Design Methodology for Multiport Antennas

by

Diana Arceo

A Dissertation Presented in Partial Fulfillment
of the Requirements for the Degree
Doctor of Philosophy

Approved November 2012 by the
Graduate Supervisory Committee:

Constantine A. Balanis, Chair
James Aberle
Karl Moeller
Joseph Palais

ARIZONA STATE UNIVERSITY

December 2012

ABSTRACT

Multiport antennas offer greater design flexibility than traditional one-port designs. An antenna array is a special case of a multiport antenna. If the antenna's inter-element spacing is electrically small, the antenna is capable of achieving superdirectivity. Superdirective antenna arrays are known to be narrow band and have low radiation resistance which leads to low radiation efficiency and high VSWR. However, by increasing the self-impedance of the antenna elements, the radiation resistance is increased but the bandwidth remains narrow.

A design methodology is developed using the ability to superimpose electric fields and multi-objective optimization to design antenna feed networks. While the emphasis in this dissertation is on antenna arrays and superdirectivity, the design methodology is general and can be applied to other multiport antennas.

The design methodology is used to design a multiport impedance-matching network and optimize both the input impedance and radiation pattern of a two-port superdirective antenna array. It is shown that the multiport impedance-matching network is capable of improving the input impedance of the antenna array while maintaining high directionality. The antenna design is critical for the methodology to improve the bandwidth and radiation characteristics of the array.

To double the bandwidth of the two-port impedance matched superdirective antenna array, a three-port Yagi–Uda antenna design is demonstrated. The addition of the extra antenna element does not increase the footprint of the antenna array. The design methodology is then used to design a symmetrical antenna array capable of steering its main beam in two directions.

DEDICATION

In loving memory of my grandmother and grandfather…

ACKNOWLEDGMENTS

I would like to thank Dr. Constantine Balanis for being my advisor and allowing me to complete my education via long distance learning. Without his support, this dissertation would never have been possible. I would also like to thank my supervisory committee: Dr. James Aberle, Dr. Joseph Palais, and Dr. Karl Moeller, for taking the time to provide comments and recommendations to this dissertation. I understand that serving in my committee was an added time commitment of an already very busy schedule.

At SPAWAR System Center Pacific, I would like to thank my work colleagues for their support. I would also like to thank the SMART and LDRD NISE program for providing funding for my labor, supplies, and travel.

Lastly, I would like to thank my amazing family: my mother Margarita and father Raul; my brothers Josue, Victor, Adrian, William; and sister Jasmine. My family's support was instrumental to the successful completion of this dissertation.

TABLE OF CONTENTS

Page

LIST OF TABLES

Table Page

LIST OF FIGURES

Figure Page

Figure Page

Figure Page

Figure Page

Figure Page

Figure Page

1. INTRODUCTION

Wireless systems continue to push the envelope in miniaturization and added capabilities. Multiport antennas may be designed to meet the demands of wireless systems, especially those on space-limited platforms. A multiport antenna offers antenna designers more degrees of design freedom than that of a traditional one-port. A multiport antenna may be classified into either a single antenna element with multiple ports or that of an antenna with multiple elements such as an antenna array and combinations of both configurations.

Figure 1 is an example of a single antenna element, a half-loop, with three ports. If ports 2 and 3 are shorted, then the half- loop antenna behaves like a traditional loop design. With the inclusion of ports 2 and 3, the antenna designer now has the freedom, for example, to load the antenna for miniaturization or to feed port 1 and port 2 out-of-phase to achieve alternative radiation patterns. With active components, the antenna can be made reconfigurable.

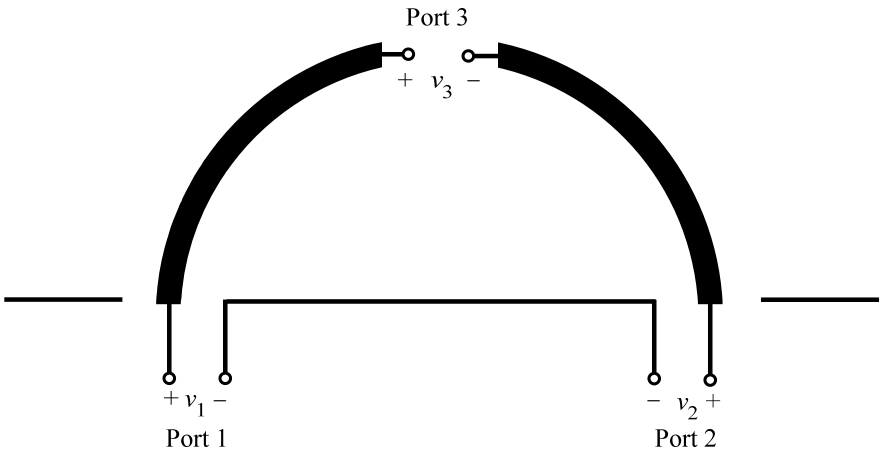

Figure 1. A three-port half-loop antenna.

A linear antenna array is another example of a multiport antenna. Linear antenna arrays provide a wireless system with the ability to improve transmission and reception with increased antenna gain. The inter-element spacing is usually chosen as 0.5λ to minimize the effects of mutual coupling. Antenna arrays of this size are impractical for space-limited platforms at low frequencies because of their large physical size. For example at the UHF frequency of 300 MHz, the wavelength is one meter and therefore the inter-element spacing would be half a meter. An antenna array that uses mutual coupling to achieve directionality is a Yagi–Uda antenna. Typical element spacing between the driven element and reflector is 0.25λ and 0.3 to 0.4λ for directors [1]. The footprint of the Yagi–Uda antenna remains large for low frequency applications. To overcome the large physical spacing of linear antenna arrays at UHF frequencies and below, antenna arrays with electrically small inter-element spacing are needed. As the inter-element spacing is reduced, the array is capable of achieving superdirectivity and is subject to a wide range of research challenges [2].

This dissertation focuses on two methods to improve the performance of superdirective arrays:

- Multiport impedance matching
- Yagi–Uda design topology

Performance improvements are sought in terms of two objectives, maximizing the absolute gain and minimizing the VSWR for a specific frequency range. To achieve these objectives, a design methodology was developed using superposition and multi-objective optimization. Sections 1.1-1.3 provide a

literature review on superdirective antenna arrays, multiport impedance matching, and Yagi–Uda antennas. Section 1.4 details the contributions made beyond existing technology and the dissertation outline.

1.1 Superdirectivity Literature Review

A multiport antenna array is capable of approaching superdirectivity as the electrical spacing between the elements is reduced. The theory behind superdirectivity states that it is possible to achieve any directivity value for a fixed aperture size [3]. A useful definition of antenna array superdirectivity is given by Hansen as "directivity higher than that obtained with the same array length and elements uniformly excited [4]."

Early work on superdirectivity includes Kraus' flat top or W8JK antenna in the late 1930s [5],[6]. Kraus began working on his flat top beam antennas after reading an article by Brown who showed that antenna gain increases as the element spacing decreases [7]. Brown also showed the limitations of these arrays due to strong mutual coupling and decrease in radiation efficiency. Although Brown and Kraus did not use the term supergain or superdirectivity, Brown and Kraus were two of the first pioneers in the field of superdirectivity.

For the linear array of N isotropic sources, shown in Figure 2, the maximum directivity, as the electrical spacing kd_s (k is the wave number and d_s is the inter-element spacing) approaches zero, was derived by Uzkov [8] as a sum of Legendre polynomials:

$$D_{\max}\left(\theta_0\right) = \sum_{n=0}^{N-1} \left(2n+1\right)\left[P_n\left(\cos\left(\theta_0\right)\right)\right]. \tag{1}$$

For an endfire radiation pattern, the maximum direction of directivity occurs at θ_0 = 0° or 180°. At these directions, $P_n(1) = 1$, and $D_{max} = N^2$. A proof of Uzkov's formulation is given in [9]. Superdirectivity is counter-intuitive; the smaller the inter-element spacing, the higher the directivity of the array. Intuitively, the larger the aperture size, the larger the antenna's directivity.

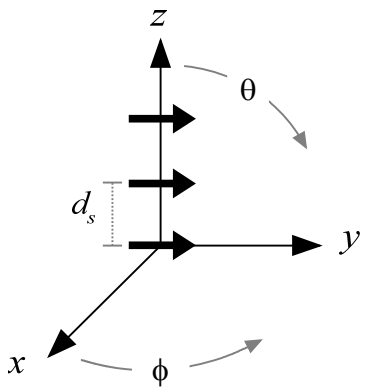

Figure 2. Coordinate system for linear array of N isotropic sources.

The ability to achieve superdirectivity in an antenna array is a challenging problem [2]. As the inter-element spacing is reduced, the mutual coupling between the radiating elements increases. The high mutual coupling decreases the radiation resistance of the antenna. The decrease of the radiation resistance is illustrated in a two-element array example. The voltage and current of each antenna element are related by

$$\begin{aligned} v_1 &= i_1 z_{11} + i_2 z_{12} \\ v_2 &= i_1 z_{21} + i_2 z_{22} \end{aligned}. \tag{2}$$

where z_{11} and z_{22} is the self-impedance of each antenna element and z_{12} and z_{21} are the mutual impedances between the elements. To achieve a directional radiation

pattern with an inter-element spacing less than 0.375λ, the antennas are driven with equal magnitude and out out-of-phase, $i_1 = i_2 \angle 180°$ [7]. Note that to achieve maximum directionality for two driven elements, Brown showed that the current magnitudes must be equal but the phase relationship varies as a function of the inter-element spacing, and the mutual and self-impedances [7]. For inter-element spacing less than 0.25λ, the optimal phase difference to produce maximum directionality varies from 150° to 170°. Therefore, 180° is used only as an example that produces a directional pattern. The input impedance of each antenna element is then

$$\begin{aligned} z_1 &= \frac{v_1}{i_1} = z_{11} - z_{12} \\ z_2 &= \frac{v_2}{i_2} = z_{22} - z_{21} \end{aligned} . \tag{3}$$

The input impedance, z_1 and z_2, of each antenna element is significantly decreased as the mutual coupling impedances z_{12} and z_{21} increases. Therefore, the input impedance of the antenna is significantly reduced leading to a low radiation resistance. The low radiation resistance leads to low radiation efficiency due to conductor losses. Superdirective antenna arrays are known to have high VSWRs and narrow bandwidths.

To mitigate the effect of mutual coupling, recent antenna designs have been proposed with antenna elements with multiple folds to increase the antenna's self-impedance [10]–[13]. These antennas have a 3 dB bandwidth ranging from 1–4%. In [13], a two-element superdirective antenna is proposed with a spacing of 0.1λ. The antenna design uses capacitors to achieve a good impedance match.

Alternatively, Lim *et al.* proposed multiple Yagi–Uda antennas with an inter-element spacing of 0.02λ [10]–[12]. However, these antennas achieve a lower gain than the maximum achievable directivity. In [12], a multi-band Yagi–Uda is proposed with an inter-element spacing of 0.02λ. This antenna achieves three resonant frequencies using three dipole directors and one driven element and achieves a 3-dB bandwidth of 6.5%, 3.5%, and 1.8%, and absolute gains of 6.14 dB, 6.13 dB, and 5.97 dB. Lim *et al.* also proposed an electronically steerable antenna array enclosed in a circle radius of 0.04λ [14]. This antenna is capable of steering its main beam in eight directions and the antenna achieved measured 3-dB bandwidths ranging from 3.3% to 5.8% and absolute gains from 8.2 dBi to 9.7 dBi.

In [15], an electrically small, superdirective antenna with parasitic elements was investigated. That paper addresses the optimal spacing between antenna elements to achieve superdirectivity and the differences in performance when using a parasitic element as a director or reflector. Although [15] primarily focused on electrically small antennas, the results are applicable to other configurations.

To overcome the challenges of superdirective antenna arrays, a multi-objective optimization design methodology is proposed. Antenna designs attempt to achieve the maximum gain possible and therefore attain narrowband performance. With multi-objective optimization, the trade-off between gain and impedance bandwidth is sought. This dissertation investigates two methods to improve the antenna gain and bandwidth. The first method uses a multiport

impedance matching feed network to simultaneously impedance-match the antenna and achieve directionality. The second method uses a three-port Yagi–Uda antenna to minimize the effects of mutual coupling.

1.2 Multiport Impedance Matching Literature Review

Impedance matching is a common method used to maximize power delivered to the load. In traditional impedance matching, a two-port impedance matching circuit maximizes the power delivered to the load from the maximum power available from the generator. R.M. Fano derived fundamental limits for impedance matching in 1950 [16]. The past decade introduced new wideband impedance matching-bound developments [17]. In particular, the Scattering Matrix Decomposition Method (SMD) is a general approach that encompasses both single and multiple ports (see Appendix A).

A preliminary study showed multiple antennas can be used to achieve wide bandwidth through multiport impedance matching [18]. Impedance matching bounds were calculated for three dipoles, resonating at 150, 300, and 600 MHz and separated by $\lambda/40$ at 150 MHz. Figure 3 shows the general setup, referred to as the multiport impedance matching network. Impedance matching bounds show the Voltage Standing Wave Ratio (VSWR) of the three dipoles is 2.7 over 100–700 MHz. If the three dipoles are directly connected and then impedance matched, the best VSWR attainable exceeds 22. Although the preliminary study shows interesting results, unaddressed factors include: an

understanding of coupling effects on the VSWR bound, resonant frequencies selection, radiation patterns, and realizable impedance-matching networks.

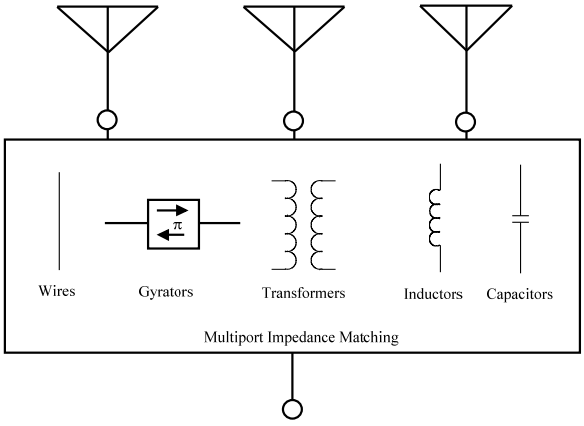

Figure 3. Multiport impedance matched antenna.

A research topic similar to that of multiport impedance matching is that of decoupling matching networks (DMN) [19]-[22]. DMN is an approach to decouple and impedance match, closely coupled antenna radiators. There are two DMN configurations. The first DMN configuration consists of inductors and capacitors in an intricate network design. To decouple three monopole antennas with 0.25λ inter-element spacing, a design has been proposed with 13 components [19]. For an inter-element spacing of 0.1λ the number of components needed grows to 16. Due to ohmic losses of the matching circuit, the matching efficiency for the 0.1λ is 35% and 65% for the 0.25λ configuration. While these efficiencies are low, without the DMN, the mismatch efficiency is 27% for the 0.25λ and 3% for the 0.1λ configuration. The second type of DMN configuration consists of designs with 90° hybrids [21] and 180° hybrids [22]. Using the 180° configuration, a superdirective antenna array was demonstrated for two

monopoles with an inter-element spacing of 0.1λ [22]. The hybrid configuration achieved a measured absolute gain of 9.87 dBi and 2.1% 3-dB bandwidth.

1.3 Yagi–Uda Literature Review

Shintaro Uda, in 1926, experimented with parasitic directors and reflectors that led to the publication of 11 articles [6]. In 1928, Hidetsugu Yagi published an article on these parasitic radiators and noted that Uda at the time had already published 9 articles. The publication grew in popularity that the antenna array was given the nomenclature of a "Yagi." A common practice now, is to refer the antenna array as a Yagi–Uda to give credit to Uda [1], [6]. Yagi–Uda antenna arrays are one of the most popular types of arrays due to its fabrication simplicity and low cost to manufacture.

The basic Yagi–Uda antenna array configuration consists of parallel dipole elements were one element is fed and the elements are parasitic elements arranged either as directors or reflectors. The directors and reflectors are energized through mutual coupling. The reflector is slightly longer than the fed dipole and the directors are slightly shorter. The Yagi–Uda antenna array demonstrated that a parasitic element cannot only reflect the electromagnetic wave but also guide it. A traditional dipole Yagi–Uda antenna array is illustrated in Figure 4 with one reflector and three directors. By adding additional directors, the gain of the antenna increases. The optimization of Yagi–Uda antenna arrays by both experimental [24] and analytical methods has been the subject of vast number of research publications [25]-[31].

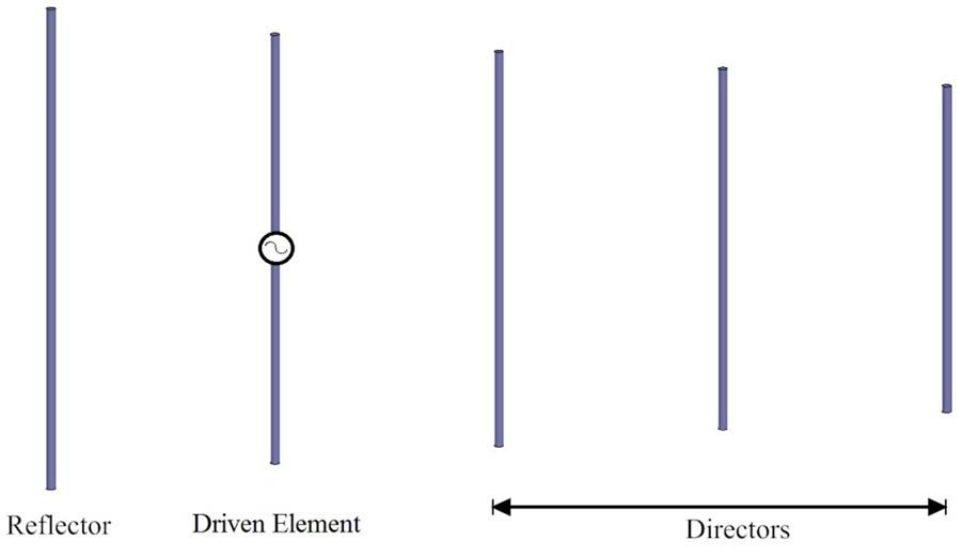

Figure 4. Traditional dipole Yagi–Uda antenna array with one reflector and three directors.

With the development of an integral equation technique to analyze Yagi–Uda antennas, the optimization of these antennas was made possible [32]. Early optimization research analyzed the optimal element spacing [25] and optimal element lengths [26] using a gradient-based approach to maximize directivity. More sophisticated optimization algorithms, such as, computational intelligence [27], genetic algorithms [28], particle swarm optimization [29], and simulated annealing [30], have been used to optimize gain, input impedance, relative side lobe level, and half-power beamwidth. Most optimized Yagi–Uda antenna designs consist of traditional linear dipole-based Yagi–Uda.

Using a multi-objecitve optimization genetic algorithm, a three-element compact Yagi–Uda antenna was proposed with an inter-element spacing of 0.0263λ and 0.0305λ, a gain of 7.4 dBi, and an input impedance of $49.87-j0.49$ ohms [31]. The publication does not mention the antenna bandwidth. Other

publications using genetic algorithms to achieve highly directional and compact Yagi–Uda includes [10]-[12].

1.4 Contributions and Dissertation Organization

This section outlines the dissertation organization and original contributions made beyond the existing technology in the subject area of directional antennas and impedance matching. All antenna designs were modeled in Expert MININEC Broadcast Professional. To include losses, the antenna models incorporate brass resistivity (3.9×10^{8} ohm-meters) in all simulations.

Chapter 2 reviews antenna metrics, formulates the multiport impedance matching problem, the superposition method used to calculate the radiation pattern of the antennas, and the design methodology that optimizes the input VSWR and radiation pattern of the antenna. The multiport impedance matching network not only determines the input VSWR of the antenna but also the radiation pattern. The design methodology contributes to existing technology by merging superposition with multi-objective optimization. By using superposition, a computational numerical modeling code can be used to calculate the admittance matrix and the electric field of each radiator. The admittance matrix and the electric fields are then used to optimize the antenna feed network. Alternative methods use analytical antenna array formulations or built-in optimization routines that are computationally intensive or expensive add-ons to the numerical code.

Chapter 3 provides the initial analysis and motivation for using multi-port impedance matching with a two-port basic monopole configuration. The chapter begins with a theoretical study to demonstrate the potential benefits of multiport impedance matching in section 3.1. Section 3.2 gives an overview of the multiport network synthesis technique and configuration used to attain a realizable circuit. Section 3.3 presents an analysis of the multiport impedance matching optimization routines using two basic monopoles with an inter-element spacing of 0.1λ. The analysis shows promise but the antenna design is limited to a gain increase of 2 dB.

Chapter 4 makes an original contribution to the design of directional antennas and impedance matching by demonstrating a multiport impedance matching network that simultaneously matched an antenna and achieved high directionality. The antenna design proposed is two monopoles with three folds in each monopole to increase the self-impedance and the inter-element spacing remains at 0.1λ. With multiport impedance matching, the bandwidth is increased 3.4 times over the original design while achieving a measured absolute gain of 8.9 dBi. The results of this study were accepted for publication [33].

Chapter 5 demonstrates how a three-port Yagi–Uda antenna is capable of achieving the superdirectivity of a two-port while not increasing the footprint. The inter-element spacing of the Yagi–Uda is ~0.05λ for a total footprint size of ~0.1λ. The antenna design achieves an unmatched 10% bandwidth with a gain of 8.8 dBi. The antenna design makes a contribution to the design of directional antennas by demonstrating that the effects of mutual coupling can be minimized

with a judicious antenna element design. The results of this design were published in [34].

Chapter 6 uses the design methodology to design a symmetrical Yagi–Uda with the capability of steering its main beam by 180°. The antenna design makes a contribution to existing technology by both demonstrating that superdirective antenna arrays with beam steering capabilities are possible with a significant improvement in bandwidth. The antenna design performance and application of the design methodology were published in [36].

Chapter 7 summarizes the dissertation and provides future research topics. Appendix A is a review of the Scattering Matrix Decomposition (SMD) method used to perform the theoretical study in section 3.1 and Appendix B is a study on how the SMD method approaches the Fano bound for a one-port.

2. MULTIPORT ANTENNA MATCHING AND GAIN

This chapter provides background information on antenna metrics related to the design of antennas, impedance matching networks, and the theory of superdirectivity. The chapter begins with a review of commonly used antenna design parameters in Section 2.1. This section also introduces the concept of impedance matching to improve the absolute gain of an antenna. Section 2.2 reviews the concept of impedance matching and formulates the necessary design equations. Section 2.3 reviews and extends a method introduced in the early 1970's of superimposing the electric fields in Norton and Thévenin equivalent circuit representations. This method, referred to as the superposition method, calculates the gain of a multiport antenna with any attached lossless load. Therefore, when an impedance matching network is attached to the multiport antenna, the resulting gain is calculated using the superposition method. Section 2.4 formulates the multi-objective problem to optimize input VSWR and the radiation pattern of an antenna. This method combines the superposition method along with multiport impedance matching.

2.1 Antenna Metrics

Antenna optimization requires engineering trade-offs between competing antenna metrics. Antenna performance metrics are reviewed in this section to set the notation for the dissertation. The gain of an antenna, G, is given by [1]

$$G(\theta,\phi) = e_{cd} D(\theta,\phi), \tag{4}$$

where e_{cd} is the radiation efficiency and D is the directivity. The directivity is "the ratio of the radiation intensity in a given direction from the antenna to the radiation intensity averaged over all directions [1]." If the direction is not given, then the directivity value is implied to be the maximum.

The radiation efficiency is the ratio of the power radiated, P_{rad}, to the power accepted by the antenna, P_{in}. The radiation efficiency is often more conveniently defined as the ratio of the power delivered to the radiation resistance, R_r, to that delivered to the conductive and dielectric losses, represented by the loss resistance R_L and R_r as given by [1]:

$$e_{cd} = \frac{R_r}{R_r + R_L}. \tag{5}$$

If $R_r >> R_L$, then the radiation efficiency of an antenna is high and the gain of the antenna approaches the directivity. When the radiation resistance is small, the radiation efficiency decreases the gain of the antenna.

The input impedance of an antenna, z_L, is another performance parameter. An antenna is impedance matched to the characteristic impedance of the transmission line to ensure sufficient power transfer from the source. Normally, the characteristic impedance, z_0, is 50 ohms. The input voltage reflection coefficient, Γ_L, is defined as [1]:

$$\Gamma_L = \frac{z_L - z_0}{z_L + z_0}. \tag{6}$$

The reflection coefficient measures how well an antenna is matched to the characteristic impedance. The reflection efficiency, e_r, or mismatch loss measures

the amount of power lost due to the impedance mismatch of the antenna. The mismatch loss is given by [1]:

$$e_r = \left(1 - \left|\Gamma_L\right|^2\right). \tag{7}$$

Figure 5 plots the relationship between mismatch loss and the reflection coefficient. The plot shows that as the impedance mismatch loss increases, more power is reflected back into the source instead of being accepted by the antenna for radiation.

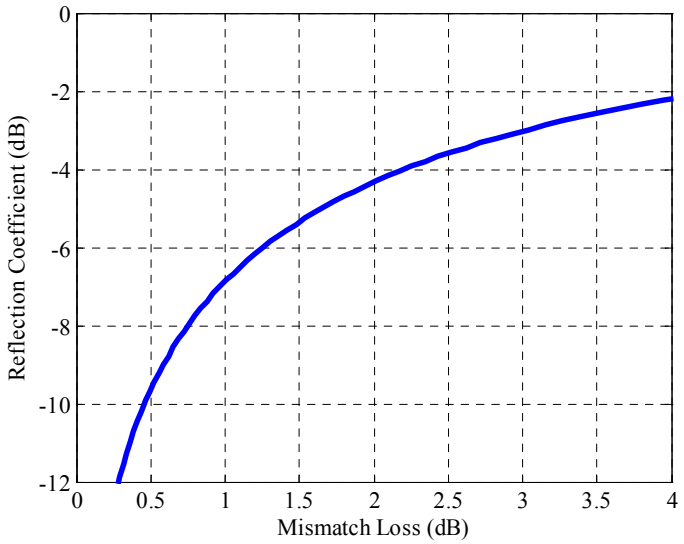

Figure 5. Relationship between the Γ and mismatch loss in dB.

The Voltage Standing Wave Ratio (VSWR) is another metric that quantifies the quality of an antenna match [1]. The VSWR is defined as:

$$\text{VSWR} = \frac{1 + \left|\Gamma_L\right|}{1 - \left|\Gamma_L\right|}. \tag{8}$$

Figure 6 plots the relationship between mismatch loss in dB and the VSWR. To minimize mismatch losses, a VSWR < 2 is often sought.

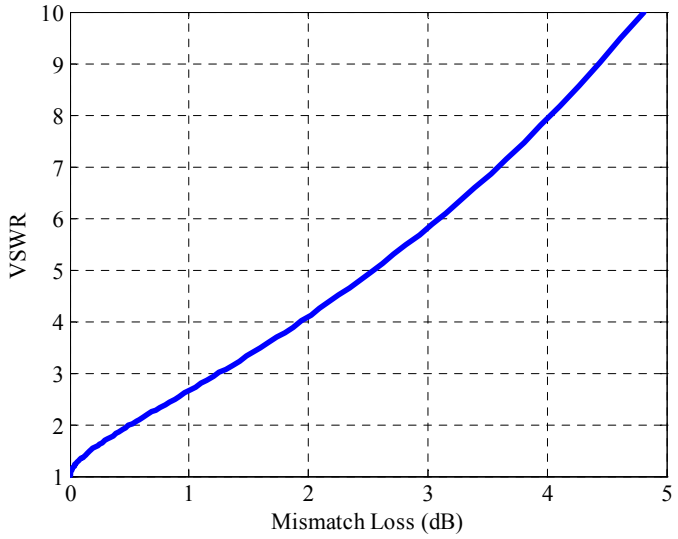

Figure 6. Relationship between VSWR and mismatch loss.

The total efficiency, e_0, of an antenna is given by [1]:

$$e_0 = e_r e_{cd}. \tag{9}$$

The realized gain or absolute gain, G_{abs}, of an antenna is defined as [1]:

$$G_{abs} = e_0 D = \left(1 - |\Gamma_L|^2\right) G \tag{10}$$

Absolute gain and gain differ by the mismatch loss. When the antenna is perfectly matched, the gain and absolute gain are the same. Impedance matching is commonly used to reduce the mismatch loss and therefore allow the absolute gain to approach the gain of the antenna.

In directional antennas, the front-to-back ratio (FBR) is used as a metric to quantify directionality. The FBR is defined as the ratio between the maximum gain, G_{Front} and the gain at 180° from the G_{Front} direction referred to as G_{Back} as shown in Figure 7.

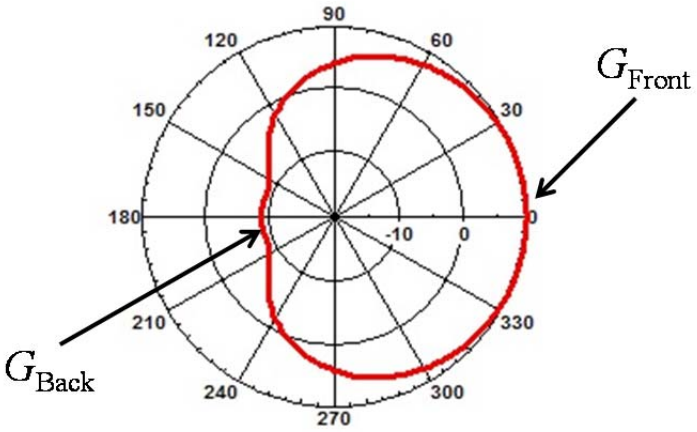

Figure 7. Directional radiation pattern.

Table 1. Commonly Used Symbols.

Symbol	Description
j	Positive square root of −1
p	Complex frequency: $p=\sigma+j\omega$
ω	Radial frequency (radians per second)
$\mathbf{U}_N$	$N \times N$ identity matrix
S	Scattering matrix (dimensionless)
Y	Admittance matrix (Siemens)
Z	Impedance matrix (ohms)
Γ	Reflection Coefficient (dimensionless)
V	Voltage vector (volts)
I	Current vector (amps)
E	Electric Field vector (volts/m)
F	Radiation Intensity (W/unit solid angle)
B	Frequency band

2.2 Multiport Impedance Matching

The input impedance of an antenna may not always be matched to the characteristic impedance of interest. The impedance mismatch causes the absolute gain to decrease. Impedance matching is a commonly used method to minimize the mismatch loss and increase the absolute gain of an antenna. This section formulates the impedance matching problem. The formulation begins with the traditional two-port configuration and then generalizes to the single input, multiple output matching configurations. The formulations are given in terms of scattering parameters (Section 2.2.1), impedance parameters (Section 2.2.2), and admittance parameters (Section 2.2.3).

2.2.1 **S** Parameters

Figure 8 shows the two-port matching schematic. The goal of the two-port matching problem is to find a lossless two-port network that maximizes the power delivered to the load. If the two-port has the scattering matrix [37]

$$\mathbf{S} = \begin{bmatrix} s_{11} & s_{12} \\ s_{21} & s_{22} \end{bmatrix}, \tag{11}$$

the reflection coefficient Γ_1 looking into port 1 is [37]

$$\Gamma_1 = s_{11} + s_{12}\Gamma_L \left(1 - s_{22}\Gamma_L\right)^{-1} s_{21}. \tag{12}$$

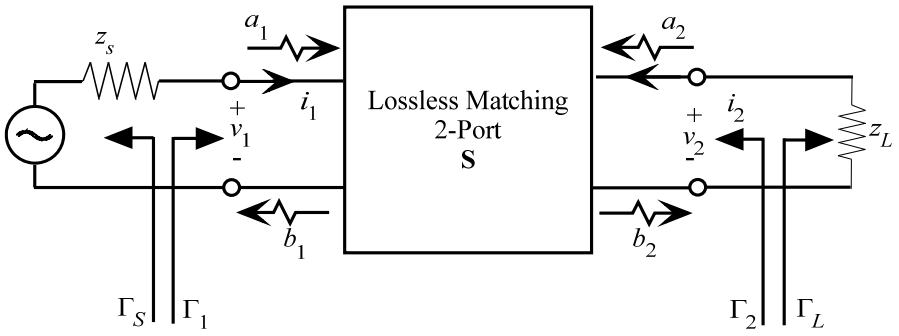

Figure 8. Cascade of a two-port and load in the scattering matrix formalism.

The amount of power delivered to the load from the generator is computed by the transducer power gain. The transducer power gain is defined as [37]

$$G_T \equiv \frac{\text{power delivered to the load}}{\text{maximum power available from the source}},$$

and calculated by [36]

$$G_T = \frac{|s_{21}|^2 \left(1-|\Gamma_s|^2\right)\left(1-|\Gamma_L|^2\right)}{|1-\Gamma_1\Gamma_S|^2 \, |1-s_{22}\Gamma_L|^2}. \tag{13}$$

where

$$\Gamma_s = \frac{z_s - z_0}{z_s + z_0}. \tag{14}$$

If the two-port is lossless, $\mathbf{S}^H\mathbf{S} = \mathbf{U}_2$, the load $\mathbf{S}_L$ is strictly passive, ${\mathbf{S}_L}^H\mathbf{S} < \mathbf{U}_2$, and the reflectance of the source is zero, $\Gamma_S = 0$, the transducer power gain simplifies to [38]

$$G_T = 1 - |\Gamma_1|^2. \tag{15}$$

The simplified transducer power gain is equivalent to the reflection efficiency given by (7).

If the two-port is lossless, then maximizing the transducer power gain is equivalent to minimizing the reflection coefficient. Minimizing the reflection coefficient is equivalent to minimizing the VSWR [37],

$$\mathrm{VSWR} = \frac{1+|\Gamma_1|}{1-|\Gamma_1|}. \tag{16}$$

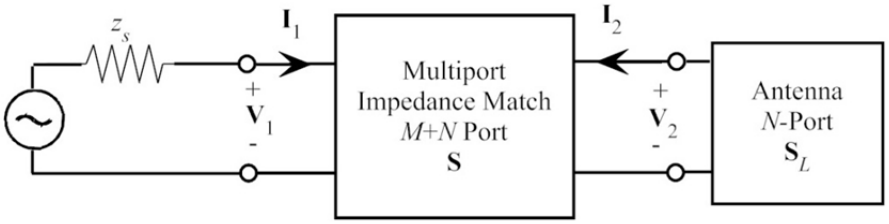

Figure 9. Cascade of an (*M*+*N*)-port and antenna load in the scattering matrix formalism.

For the multiport matching problem in Figure 9, let a *M*+*N* multiport have a scattering matrix with a block structure [18]

$$\mathbf{S} = \begin{bmatrix} \mathbf{S}_{11} & \mathbf{S}_{12} \\ \mathbf{S}_{21} & \mathbf{S}_{22} \end{bmatrix}. \tag{17}$$

Here $\mathbf{S}_{11}$ is an $M \times M$ scattering matrix corresponding to port 1, 2 …, *M*. The matrix $\mathbf{S}_{22}$ is an $N \times N$ scattering matrix corresponding to the remaining *N* ports. If these remaining *N* ports are terminated in an *N*-port load with the scattering matrix $\mathbf{S}_L$, the scattering matrix looking into ports 1, 2, …, *M* is [18]

$$\mathbf{S}_M = \mathbf{S}_{11} + \mathbf{S}_{12}\mathbf{S}_L\left(\mathbf{U}_N - \mathbf{S}_{22}\mathbf{S}_L\right)^{-1}\mathbf{S}_{21}. \tag{18}$$

For the single-input two-output case ($M = 1$, $N = 2$) shown in Figure 10, the input reflection coefficient looking into Port 1 is

$$\Gamma_1 = s_{11} + \mathbf{S}_{12}\mathbf{S}_L\left(\mathbf{U}_2 - \mathbf{S}_{22}\mathbf{S}_L\right)^{-1}\mathbf{S}_{21} \tag{19}$$

and transducer power gain is [18]

$$G_T = \frac{\left(1-\left|\Gamma_s\right|^2\right)}{\left|1-\Gamma_s\Gamma_1\right|^2}\mathbf{S}_{21}^H\left(\mathbf{U}_2 - \mathbf{S}_{22}\mathbf{S}_L\right)^{-H}\left(\mathbf{U}_2 - \mathbf{S}_L^H\mathbf{S}_L\right)\left(\mathbf{U}_2 - \mathbf{S}_{22}\mathbf{S}_L\right)^{-1}\mathbf{S}_{21}. \tag{20}$$

Just as the two-port case, multiport transducer power gain simplifies to (15), provided the multiport is lossless, $\mathbf{S}^H\mathbf{S} = \mathbf{U}_N$, the load $\mathbf{S}_L$ is strictly passive, $\mathbf{S}_L{}^H\mathbf{S} < \mathbf{U}_N$, and the reflectance of the source is zero, $\Gamma_S = 0$.

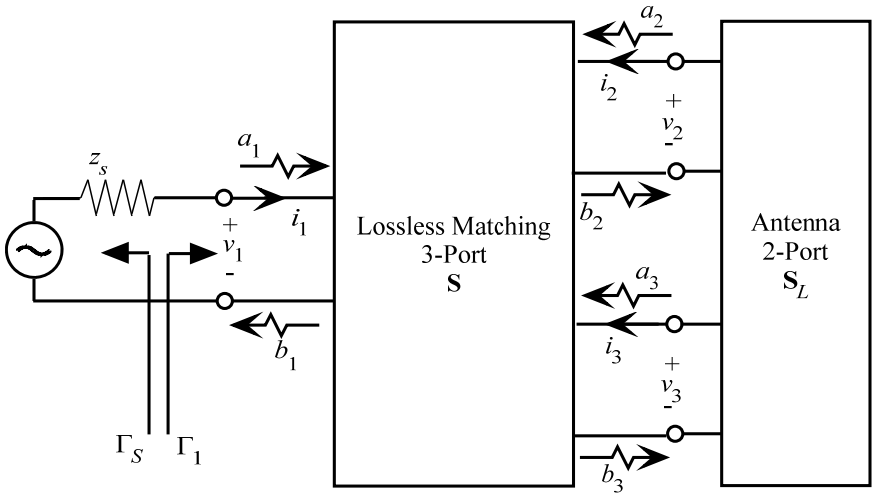

Figure 10. Three-port single-input multiport **S** parameters configuration.

2.2.2 **Z** Parameters

Figure 11 shows the two-port matching schematic in the impedance formalism. The two-port matching problem is to find a lossless two-port network that maximizes the power delivered to the antenna load, z_L. Typically for antennas, the matching problem is to match the input impedance, z_1, of the antenna to a 50-ohm transmission line.

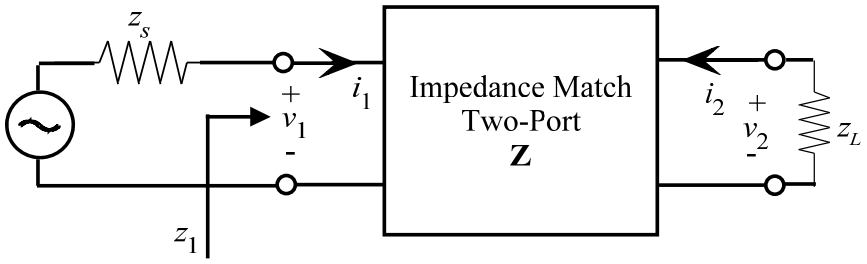

Figure 11. Cascade of a two-port and load in the impedance formalism.

The two-port has the following impedance matrix [37]

$$\begin{bmatrix} v_1 \\ v_2 \end{bmatrix} = \begin{bmatrix} z_{11} & z_{12} \\ z_{21} & z_{22} \end{bmatrix} \begin{bmatrix} i_1 \\ i_2 \end{bmatrix}. \tag{21}$$

The voltage at the antenna port, v_2, is related to the antenna's impedance by $v_2 = -z_L i_2$. Given this relationship, the input impedance is

$$z_1 = \frac{v_1}{i_1} = z_{11} - \frac{z_{12} z_{21}}{z_{22} + z_L}. \tag{22}$$

The input reflection coefficient looking into port 1 is

$$\Gamma_1 = \frac{z_1 - z_0}{z_1 + z_0}, \tag{23}$$

and the input VSWR is given by (16).

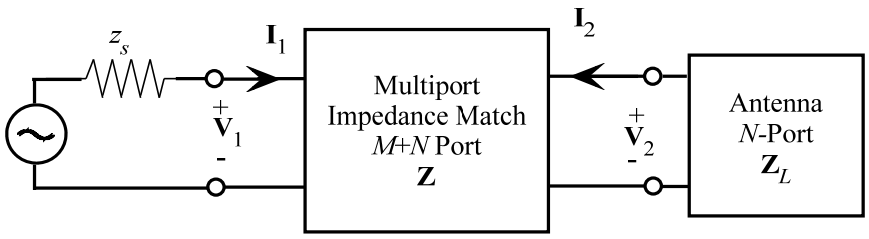

Figure 12. Cascade of an (*M*+*N*)-port and antenna load in the impedance matrix formalism.

For the multiport impedance matching network shown in Figure 12, let a *M*+*N* multiport have an impedance matrix with a block structure

$$\mathbf{Z} = \begin{bmatrix} \mathbf{Z}_{11} & \mathbf{Z}_{12} \\ \mathbf{Z}_{21} & \mathbf{Z}_{22} \end{bmatrix}, \tag{24}$$

where $\mathbf{Z}_{11}$ is the $M \times M$ impedance matrix corresponding to ports 1, 2 …, *M*. The matrix $\mathbf{Z}_{22}$ is an $N \times N$ impedance matrix corresponding to the remaining *N* ports. If the remaining *N* ports are terminated in an *N*-port load with the impedance matrix $\mathbf{Z}_L$, the impedance matrix looking into ports 1, 2, …, *M* is

$$\mathbf{Z}_M = \mathbf{Z}_{11} - \mathbf{Z}_{12}\left(\mathbf{Z}_{22} + \mathbf{Z}_L\right)^{-1}\mathbf{Z}_{21}, \tag{25}$$

because the voltages at the *N*-port load, $\mathbf{V}_2$, is related to the impedance $\mathbf{Z}_L$, by $\mathbf{V}_2 = -\mathbf{Z}_L\,\mathbf{I}_2$.

For the single-input two-output case ($M = 1$, $N = 2$), the input impedance is

$$z_1 = z_{11} - \mathbf{Z}_{12}\left(\mathbf{Z}_{22} + \mathbf{Z}_L\right)^{-1}\mathbf{Z}_{21}, \tag{26}$$

and the input Γ_1 is given by (23) and input VSWR by (16).

2.2.3 **Y** Parameters

The admittance matrix is related to the impedance matrix by [37]

$$\mathbf{Y} = \mathbf{Z}^{-1}. \tag{27}$$

Because of this relationship, only the single input, multiple output configuration is stated in this section. Figure 13 is a network description of the antenna configuration for a multiport antenna with a multiport impedance matching network. The admittance matrix of the multiport impedance matching network is denoted as $\mathbf{Y}$, and the admittance matrix of the antenna is denoted as $\mathbf{Y}_L$. The relationship between the admittance matrix, voltage, and currents at each input port is given by the block matrix (28) where:

- y_{11} is a scalar
- $\mathbf{Y}_{12}$ is a $1\times(N-1)$ vector
- $\mathbf{Y}_{21}$ is a $(N-1)\times1$ vector
- $\mathbf{Y}_{22}$ is an $(N-1)\times(N-1)$ matrix
- $\mathbf{I}_2$ is an $(N-1)\times1$ vector

The voltage at each of the antenna ports is constrained by $\mathbf{I}_2=-\mathbf{Y}_L\mathbf{V}_2$. Given this constraint, the voltage at each antenna element is given by (29). The input admittance, y_1, is given by (30).

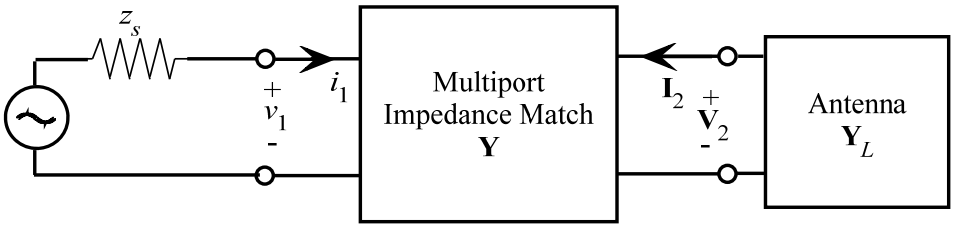

Figure 13. Cascade of an (*M*+*N*)-port and antenna load in the admittance matrix formalism.

$$\begin{bmatrix} i_1 \\ \mathbf{I}_2 \end{bmatrix} = \begin{bmatrix} y_{11} & \mathbf{Y}_{12} \\ \mathbf{Y}_{21} & \mathbf{Y}_{22} \end{bmatrix} \begin{bmatrix} v_1 \\ \mathbf{V}_2 \end{bmatrix}, \tag{28}$$

$$\mathbf{V}_2 = -\left(\mathbf{Y}_{22} + \mathbf{Y}_L\right)^{-1} v_1, \tag{29}$$

$$y_1 = \frac{i_1}{v_1} = y_{11} - \mathbf{Y}_{12}\left(\mathbf{Y}_{22} + \mathbf{Y}_L\right)^{-1}\mathbf{Y}_{21}. \tag{30}$$

The reflection coefficient is given by

$$\Gamma_1 = \frac{y_0 - y_1}{y_0 + y_1}, \tag{31}$$

where y_0 is the characteristic admittance, $y_0 = 1/z_0$, and the input VSWR is given by (16).

2.3 Multiport Antenna Gain: Superposition Method

This section outlines a procedure to calculate the radiation pattern of a loaded multiport antenna. In 1973, Harrington and Mautz formulated the problem of a loaded *N*-port scatterer in terms of two *N*-port networks connected together [39]. In 1978, Harrington formulated the problem of calculating the radiation characteristics of an *N*-port reactively loaded circular antenna array in a similar approach to that of the scatterer [40]. This method has previously been used to

design reactively steered adaptive array using mircrostrip patch antenna elements [50]. The electric field used was an analytical form based on the transmission line model and the impedance data was attained through measurements.

The *N*-port antenna array is characterized by the impedance matrix $\mathbf{Z}_A$, or admittance matrix $\mathbf{Y}_A$. The load feed network is passive, and it is characterized by the impedance matrix $\mathbf{Z}_L$ or admittance matrix $\mathbf{Y}_L$. When formulating the problem in terms of the impedance matrix, the voltage and current relationship is given by the Thévenin equivalent network shown in Figure 14. The load feed network and the antenna array are related to the Thevenin equivalent voltage and current as

$$\mathbf{V}^{OC} = \left(\mathbf{Z}_A + \mathbf{Z}_L\right)\mathbf{I}. \tag{32}$$

$\mathbf{V}^{OC}$ and $\mathbf{I}$ are the port voltage and current vectors.

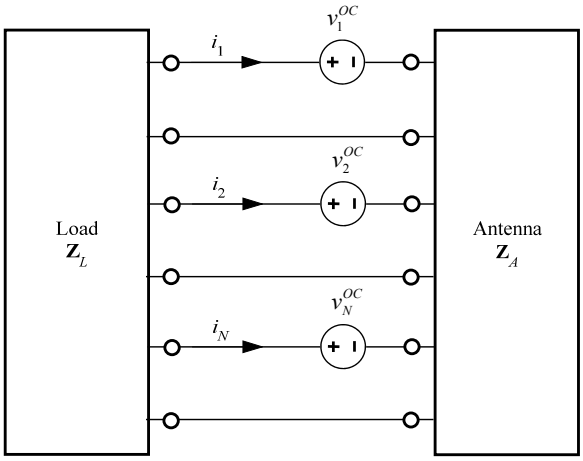

Figure 14. Thévenin equivalent of an antenna connected to a load network.

The electric field radiated by each antenna element, when excited by a unit current and all other ports are open-circuited, is denoted as E_n^{OC}. The electric field

radiated by the antenna array is the superposition of the electric field, E_n^{OC}, of each antenna element multiplied by the current, i_n, induced in each port as follows

$$E = \sum_{n=1}^{N} i_n E_n^{OC}. \tag{33}$$

Rewriting (33) in vector form and substituting (32), the electric field of the antenna array is given by

$$\begin{aligned} \mathbf{E} &= \mathbf{E}^{OC}\mathbf{I} \\ &= \mathbf{E}^{OC}\left(\mathbf{Z}_A + \mathbf{Z}_L\right)^{-1}\mathbf{V}^{OC}. \end{aligned} \tag{34}$$

The dual short-circuit equivalent representation of the loaded antenna array is represented by its Norton equivalent network shown in Figure 15. The admittance matrices $\mathbf{Y}_A$ and $\mathbf{Y}_L$ are related to the Norton equivalent voltage at each port, $\mathbf{V}$, and the current source, $\mathbf{I}^{SC}$, by

$$\mathbf{I}^{SC} = \left(\mathbf{Y}_A + \mathbf{Y}_L\right)\mathbf{V}. \tag{35}$$

The electric field radiated by each antenna element when excited by a unit voltage, and all other ports are short-circuited, is denoted as E_n^{SC}. The electric field radiated by the antenna array is the superposition of the electric field, E_n^{SC}, of each antenna element multiplied by the voltage, v_n, induced in each port as follows

$$E = \sum_{n=1}^{N} E_n^{SC} v_n. \tag{36}$$

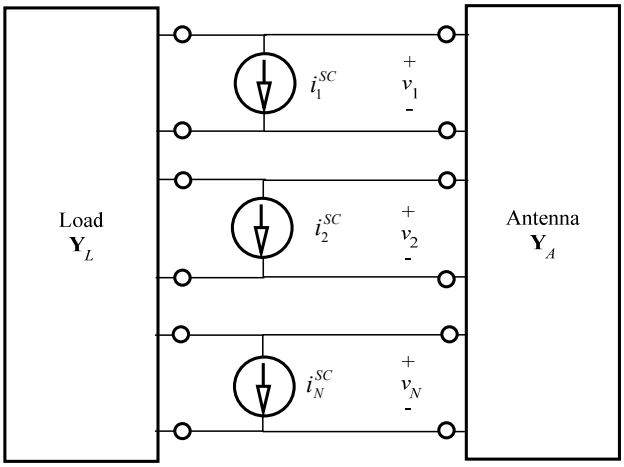

Figure 15. Norton equivalent of an antenna connected to a load network.

Rewriting (36) in vector form and substituting (35), the electric field of the antenna array is given by

$$\begin{aligned}\mathbf{E} &= \mathbf{E}^{SC}\mathbf{V} \\ &= \mathbf{E}^{SC}\left(\mathbf{Y}_A + \mathbf{Y}_L\right)^{-1}\mathbf{I}^{SC}.\end{aligned} \tag{37}$$

The gain of an antenna was defined in Section 2.1 in terms of radiation efficiency and directivity. The directivity of an antenna is given by [1]

$$D(\theta,\phi) = \frac{4\pi F(\theta,\phi)}{P_{rad}}, \tag{38}$$

where F is the radiation intensity and P_{rad} is the total radiated power of the antenna. The radiation intensity is the power radiated per unit solid angle. The radiation intensity is related to the far-zone electric field by

$$F(\theta,\phi) = \frac{r^2}{2\eta}\left|E(r,\theta,\phi)\right|^2, \tag{39}$$

where r is the radius of the observation sphere encompassing the antenna, η is the intrinsic impedance, and E is the far-zone electric field. The total radiated power is related to the input power, P_{in}, by

$$P_{rad} = e_{cd} P_{in}. \tag{40}$$

The input power into the antenna is given by

$$P_{in} = \frac{1}{2}\mathrm{Re}\left(vi^*\right), \tag{41}$$

where v is the applied source voltage and i^* is the conjugate of the resulting feed excitation current. Substituting (41) into (40) and then substituting (40) and (39) into (38), the gain of an antenna given by (4) can be rewritten as

$$G\left(\theta,\phi\right) = \frac{4\pi r^2}{\eta}\frac{\left|\mathbf{E}\left(r,\theta,\phi\right)\right|^2}{\mathrm{Re}\left(\mathbf{V}\mathbf{I}^*\right)}. \tag{42}$$

The gain of the loaded multiport antenna is calculated from the superimposed electric fields using either the impedance (open) or the admittance (short) configuration. Computationally, the admittance formalism produces more accurate results, and it is the formalism used in MININEC to calculate the admittance matrix of a multiport system. Substituting (36) into (42), the gain of an N-port antenna is given by

$$G\left(\theta,\phi\right) = \frac{4\pi r^2\left|\sum_{n=1}^{N} v_n E_n^{SC}\left(r,\theta,\phi\right)\right|^2}{\eta\sum_{n=1}^{N}\mathrm{Re}\left(v_n i_n^*\right)}. \tag{43}$$

The general procedure for calculating the gain of a multiport antenna using MININEC is as follows:

1. Calculate the admittance matrix of the multiport antenna.
2. Calculate the electric field of each antenna element by exciting the antenna element with one volt and shorting all other elements. The electric field is calculated at the far-zone, $r > 2D^2/\lambda$, where D is the maximum size of the multiport antenna.
3. Calculate the admittance matrix of the antenna load.
4. Given the admittance matrix of the load and the antenna, calculate the applied voltage at each port using (29).
5. Calculate the gain of the multiport antenna with the attached load using the applied voltage at each port and the electric fields using (43).

2.4 Multi-Objective Design Methodology

Optimization is used in a wide variety of decision-making fields including business, medicine, and engineering. Research in optimization methods can be categorized into mathematical programming techniques, stochastic process techniques, and statistical methods [41]. Calculus based optimization methods can be traced to Newton, Lagrange, and Cauchy. Lagrange made contributions in constrained optimization problems while Cauchy contributed to the steepest descent method.

The requirement to optimize more than one objective function has led to the development of multi-objective optimization techniques. The first attributed reference to multi-objective optimization traces back to Edgeworth in 1881, then to Pareto in 1896 [42]. With the development of computers, a vast number of

methods to compute optimization problems have been developed including simulated annealing, genetic algorithms, neural network methods, and game theory [41].

This chapter outlines the design methodology used to design multiport antennas. Section 2.3 outlines a method to calculate the gain of antenna with an arbitrary attached network. Section 2.2 describes how to calculate the input VSWR of a cascade of a multiport matching network and a multiport antenna. By having the capability to calculate the gain and input VSWR, a multi-objective optimization problem is formulated where the antenna designer may optimize both functions for a particular performance criterion. For this dissertation, the performance criteria is to

- Minimize the input VSWR for lossless network configuration
- Maximize the gain of a multiport antenna in a particular direction

The input VSWR is measured over a frequency band B, and therefore the maximum or worst VSWR value over the frequency band is denoted by

$$\mathrm{VSWR}_{\max} = \max\{\mathrm{VSWR}(\Gamma_1; \mathrm{B})\}.$$

Similarly, over the frequency band, B, the smallest or worst gain is denoted by

$$\min\{\mathrm{gain}(\theta_0, \phi_0; B)\}.$$

The multiport impedance matching network must simultaneously minimize the worst VSWR value while maximizing the worst gain over the frequency band. In standard optimization problems, the objective functions are minimized. Therefore, to maximize the worst gain, the goal is to minimize the negative of gain (in decibles) or

$$-G_{\max} = \max\{-\text{gain}(\theta_0, \phi_0, B), \text{dBi}\}.$$

Therefore, the multi-objective optimization objective functions are

$$\text{minimize } \gamma(\mathbf{x}) = \begin{bmatrix} \gamma_1(\mathbf{x}) \\ \gamma_2(\mathbf{x}) \end{bmatrix} = \begin{bmatrix} \text{VSWR}_{\max}(\mathbf{x}) \\ -G_{\max}(\mathbf{x}) \end{bmatrix}. \tag{44}$$

where the vector $\mathbf{x} \in \mathbf{X}$ parameterize the multiport matching network. The fundamental object is the performance image $\gamma(\mathbf{X}) := \{\gamma(\mathbf{x}): \mathbf{x} \in \mathbf{X}\}$. Minimizing $\gamma(\mathbf{x})$ over $\mathbf{x} \in \mathbf{X}$ is the search for the minimal elements of the performance image. Any $\gamma(\mathbf{x}_p)$ is a minimal element of $\gamma(\mathbf{X})$ provided no $\mathbf{x} \in \mathbf{X}$ has a better performance as $\gamma(\mathbf{x}) \leq \gamma(\mathbf{x}_p)$, where the vector inequality is applied component-wise and at least one inequality is strict inequality [43]. If $\gamma(\mathbf{x}_p)$ is a minimal element of $\gamma(\mathbf{X})$, its pre-image $\mathbf{x}_p \in \mathbf{X}$ is called *Pareto optimal*. The image of the Pareto optimal is the Pareto front [44]. Figure 16 is an illustration of the performance image and the minimal elements.

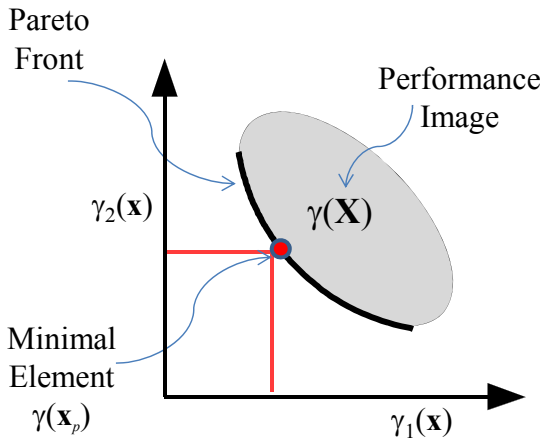

Figure 16. Minimal elements of a performance image.

The method selected to solve a multi-objective optimization problem depends on the specific antenna design. Three main methods are used:

1. Dense Sampling: This method involves filling out the performance image by parameterizing the vector **x** and calculating all possible solutions [45]. This method is impractical for most optimization problems due to the massive amount of computations required. For problems with a small set and bounded **x**, it is possible to use this method efficiently. This method is used to design the antennas in section 6. By filling out the performance image, the minimal elements are identified and the Pareto front is estimated.
2. Single-objective: This method optimizes one single objective function and then calculates the results for the second objective function. This method does not produce a Pareto front or minimal elements, but may be used to initialize a multi-objective algorithm [45]. In some cases, minimizing one objective function is sufficient to attain a suitable solution for an antenna design. This is the case for the antenna designed in section 4.
3. Goal-Attainment Method (GAM): The GAM algorithm, developed by Gembicki [46], is the algorithm used by *MATLAB* © [47]. This method calculates the minimal elements by assigning weights, w, to each objective function and specifying a design goal.

The *MATLAB* © based Optimization toolbox [47] provides the necessary tools for both the single-objective and multi-objective problems in this dissertation. The single-objective function is *fmincon* and the multi-objective function is *fgoalattain*. The *fmincon* function is a constrained nonlinear

optimization function that attempts to find the minimum of a multivariable scalar function with a starting initial estimate. The *fgoalattain* function solves the goal-attainment problem by attempting to make the objective function attain the predetermined goal with a specific set of weights, and starting initial estimate. To attain the Pareto front, the weights for each objective function are varied from zero to one such that $w_2 = (1-w_1)$, $0 < w_1 < 1$ where w_1 is the weight assigned to the first objective function and w_2 is the weight of the second objective. . The selected goals are for a VSWR = 1 and a gain of G_{max} = 10 dBi.

For a particular multiport antenna design, a multiport impedance matching network is designed to optimize the radiation pattern and input VSWR. The electric field in the far-zone is calculated for each port, along with the admittance matrix of the antenna. With these parameters the resulting input VSWR and radiation pattern is calculated using (16) and (43) for a particular multiport matching network. If after optimizing the multiport matching network, the design does not meet the design goals, then an antenna redesign is required as demonstrated in chapter 4. Figure 17 is an illustration of the design loop used to optimize the input VSWR and gain.

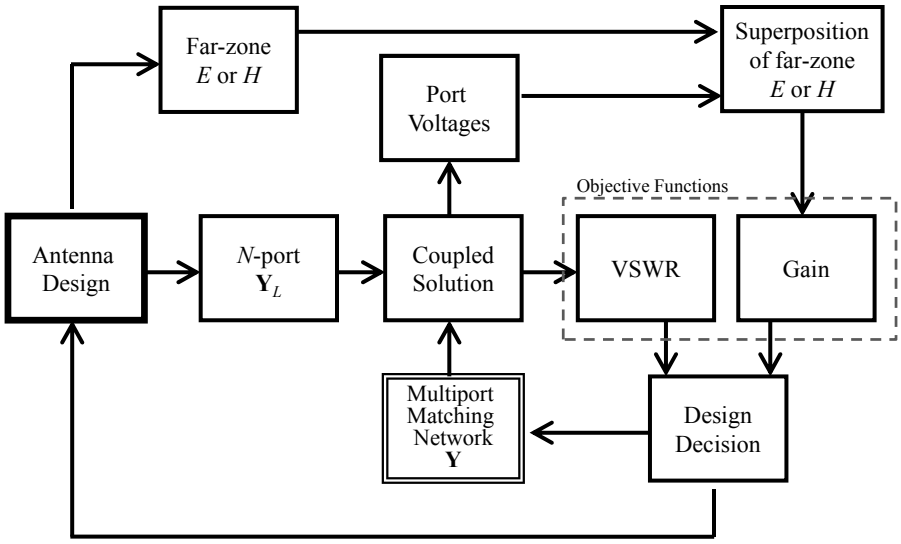

Figure 17. Multi-Object design methodology for multiport matching networks.

3. TWO-PORT IMPEDANCE MATCH BASIC ANTENNA

This chapter investigates the design of a two-port monopole antenna array. The chapter begins with a theoretical resonant frequency study of two basic monopoles to determine the relationship between the self-resonance of the monopoles to the input VSWR for a specific bandwidth. The resonant frequencies are varied by varying the height of one monopole while the other monopole remains static. The study is described in section 3.1. The best possible VSWR bound is calculated for two frequency bands and two inter-element spacing configurations. The result of this study provides motivation that a multiport impedance matching network is capable of reducing the VSWR of the antenna array. Section 3.2 is an overview of the network synthesis algorithm used to optimize the multiport network along with the changes made to the algorithm for this dissertation. Section 3.3 optimizes the input VSWR and radiation pattern for a basic two-port monopole configuration with limited success. The chapter conclusions are given in section 3.4.

3.1 Theoretical Parametric Resonant Frequency Study

A systematic set of simulations were completed in Expert MININEC to compute the best possible VSWR bound for each configuration. The admittance matrix was calculated for each simulation and the admittance matrix was later verified with measurements. The VSWR bound is used to compare the multiport impedance matching against traditional two-port impedance matching. The method used to compute the best possible VSWR bound for a specific frequency range is referred

to as the Scattering Matrix Decomposition (SMD) method. The VSWR bound is calculated as a function of number of lumped elements, *n*, and converges to the Fano Bound for a one-port, as the number of lumped elements increases. The theory behind the SMD method is described in Appendix A, and a study showing how the method converges to the Fano bound is described in Appendix B.

Monopoles were selected as the radiating antenna elements because of their simplicity in modeling, fabrication, and known attributes. The lowest operating frequency was set to 200 MHz, f_1, and corresponds to an antenna height of approximately 36.5 cm. The second antenna's resonant frequency, f_2, was varied between 200 to 400 MHz (36.5 cm to 19.3 cm) to study the effects of different resonances. The antennas were separated by a distance d_s, as shown in Figure 18. Two distances were studied: $\lambda_1/2$ and $\lambda_1/25$, where λ_1 is the wavelength at 200 MHz or 1.5 meters.

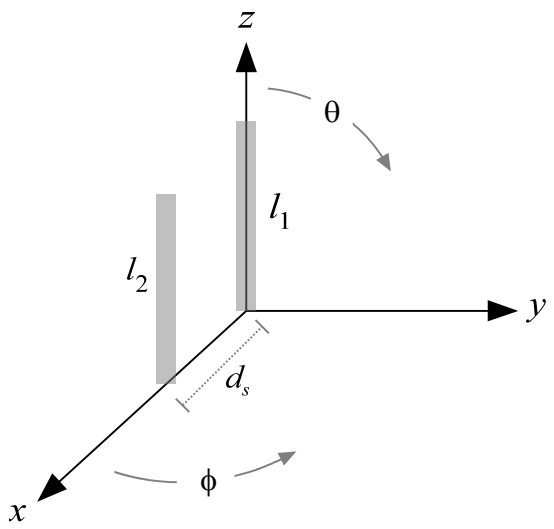

Figure 18. Two-port monopole setup for the theoretical resonant frequency study.

Figure 19. Two-port monopole fabricated to measure the *S* parameters and validate the MININEC calculations used in the theoretical study.

To verify the admittance matrix calculated from MININEC, two brass monopoles were fabricated with a diameter of 1.5 mm and placed at a distance of $\lambda_1/25$ between the antennas. The antennas were placed in an outdoor ground plane with dimensions approximating 50×50 ft^2. The ground plane has a small opening in the middle to run cables connected to an underground network analyzer. The two-port *S* parameters of the antennas were measured, while the height of one of the antennas was systematically shortened to correspond to the same frequencies calculated. A photo of the measurement-setup is shown in Figure 19.

The SMD estimates the optimal VSWR. Increasing the degree *n* decreases the VSWR until a Fano-type bound occurs. By experimentation and the results of the Fano-Bound comparison in Appendix B, $n = 10$ is sufficient to estimate the best possible bound. In practice, each component introduces losses and 10 reactive components may sustain too much loss. Nevertheless, $n = 10$ gives a

better approximation of the bound with better assurance of the calculation not being trapped in a local minima.

Two frequency bands were investigated. The first band covers 190 to 390 MHz and has 73.5% bandwidth. The second band covers 190 to 990 MHz and has 184% bandwidth. These bands were selected for the following two reasons: First, at f_1, the anti-resonance will occur at 400 MHz and the second resonance at 600 MHz. By selecting the upper frequency to be 390 MHz, the selected bandwidth only includes the first-order resonance. Second, the 190 to 990 MHz bandwidth was selected to include the anti-resonance and second resonance. By including this larger bandwidth, a better understanding of the multiport matching capabilities is revealed.

The multiport SMD bound in Figure 20 is compared to the direct connection SMD bound in Figure 21. The direct connection consists of converting the two-port monopole antenna into a single port. The SMD bound is then calculated for the single port connection. The multiport configuration is compared against the direct connection to show the differences between the impedance match of each.

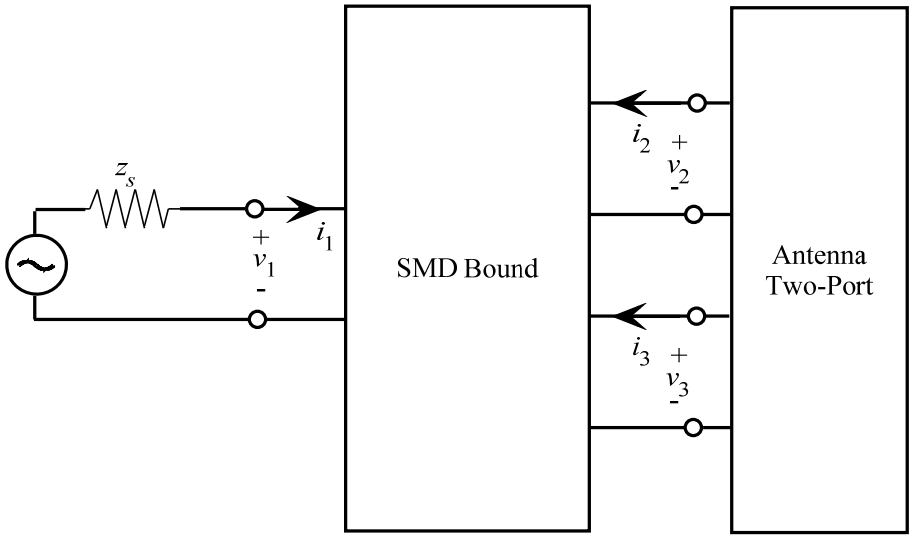

Figure 20. Cascade of the multiport SMD bound and the two-port antenna.

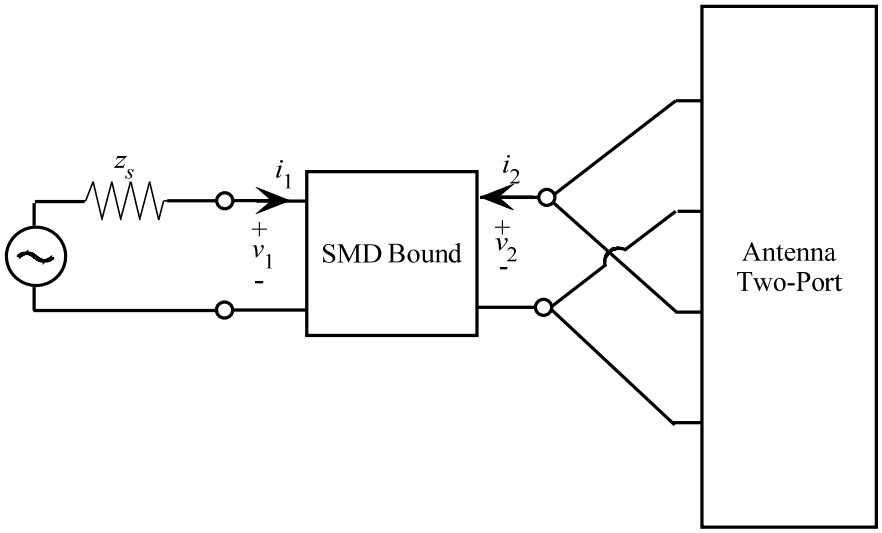

Figure 21. Cascade of the SMD bound and the two-port antenna with a direct connection.

The SMD VSWR bound results for 190 to 390 MHz bandwidth configuration are shown in Figure 22. The figure plots the length of the second monopole against the SMD VSWR bound. The SMD VSWR bound is the maximum VSWR over the entire frequency band. The plot shows the maximum

VSWR remains below 2 while the resonant frequency of the second monopole is increased by shorting the monopole lengths for the MININEC simulations. The measured data shows the maximum VSWR is below 3 and approaches 2 as the resonant frequency of the second monopole is increased. When both antenna lengths are at 36.5 cm, the VSWR results between the SMD multiport impedance match and the direct connection are similar. As the resonant frequency of the second monopole is increased, the direct connection VSWR also increases. The multiport impedance matching configuration is capable of achieving a significant lower VSWR than the direct connection when the monopole lengths are not the same. There is a close agreement between the measured and calculated results.

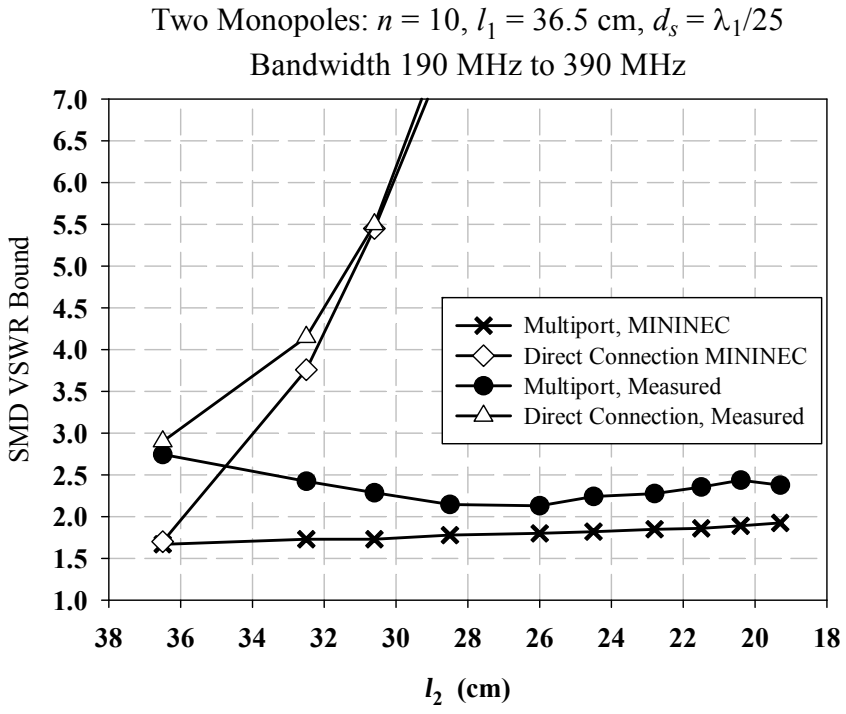

Figure 22. SMD bound and direct connection results (190–390 MHz).

The direct connection results are explained by mutual coupling. Connecting two monopoles of the same length are equivalent to a single "fat monopole" that exhibits a larger bandwidth. The concept of a "fat monopole" is basic to antenna theory [55]. It is well known that the operational bandwidth of an antenna can be enlarged by decreasing the length to diameter ratio. That is, by keeping the length constant and increasing the diameter of the antenna increases the bandwidth [55]. Without the coupling, the monopoles are equivalent to two loads in parallel. The impedance of a $\lambda/4$ monopole at resonance is $36.5 + j21.25$ (VSWR = 1.78). Therefore, the impedance of two monopoles in parallel is $18.25 + j10.625$ (VSWR = 2.88). By using multiport matching, the impedance of the monopoles are modified before being connected.

For the wider bandwidth configuration, the VSWR bounds in Figure 23 show similar trends compared to the narrow band case of Figure 22. The simulated results agree well with the measured data. The VSWR bound for the larger bandwidth is greater than the narrow bandwidth. With both monopoles at the same length, the larger bandwidth, has a VSWR bound of 2.8 from the MININEC data and 1.8 for the narrower bandwidth. These results are as expected: the larger the bandwidth the larger the VSWR bound. The VSWR bound of the larger bandwidth decreases as the resonant frequency of the second monopole decreases. Even as the monopole length decreases to 19.3 cm (~400 MHz) the antenna remains well matched. Similar to the narrow band case, the direct connection has a VSWR bound close to that of the multiport case when both

monopole lengths are the same lengths but sharply increases as the monopole's resonant frequency is increased.

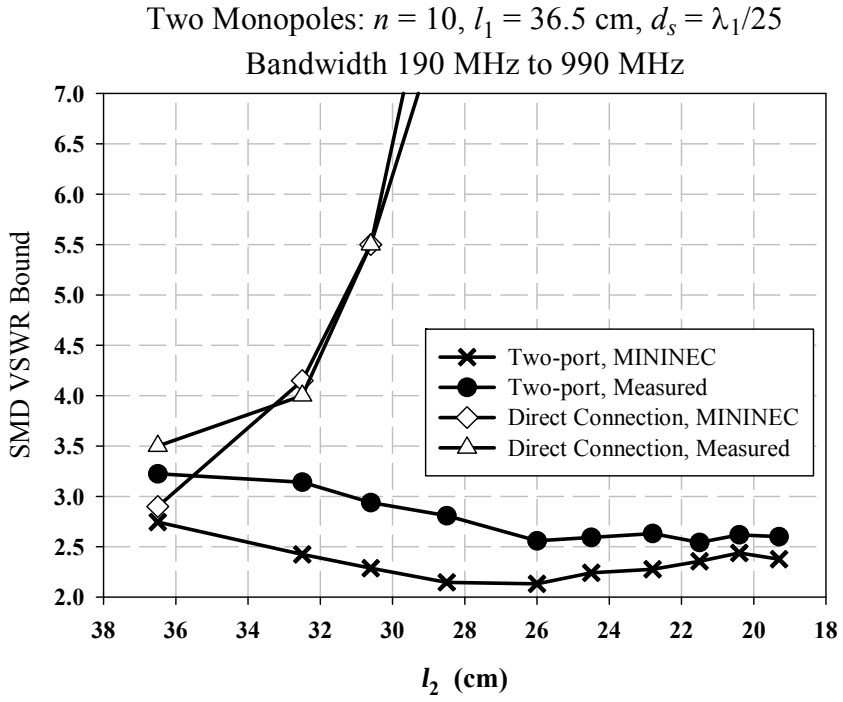

Figure 23. SMD bound and direct connection results (190–990 MHz).

The separation distance between the two monopoles was increased to d_s = λ_1/2 and the results are plotted in Figure 24 for both bandwidth configurations. The separation distance between the two monopoles was increased to decrease the mutual coupling between the monopoles. The VSWR bound results show a lower bound is possible with the multiport matching, as opposed to the large coupling case of d_s = λ_1/25. At l_2 = 36.5 cm. The VSWR bound of the narrow bound case is 1.4, as opposed to 1.6, and the VSWR bound for the larger bandwidth is 2.1 as opposed to 2.7. There are some notable differences between the d_s = λ_1/2 and d_s = λ_1/25 for the direct connection configuration. When both antenna elements are at

the same length, the direct connection and multiport matching configuration do not converge to the same VSWR bound. At $d_s = \lambda_1/2$, the direct connection converges to a larger bound than that of $d_s = \lambda_1/25$. As previously explained, without the coupling, the antennas are similar to two loads in parallel. As the resonant frequency of the second monopole decreases, the VSWR bound of direct connection also decreases, contrary to the $d_s = \lambda_1/25$ when the bound sharply increased.

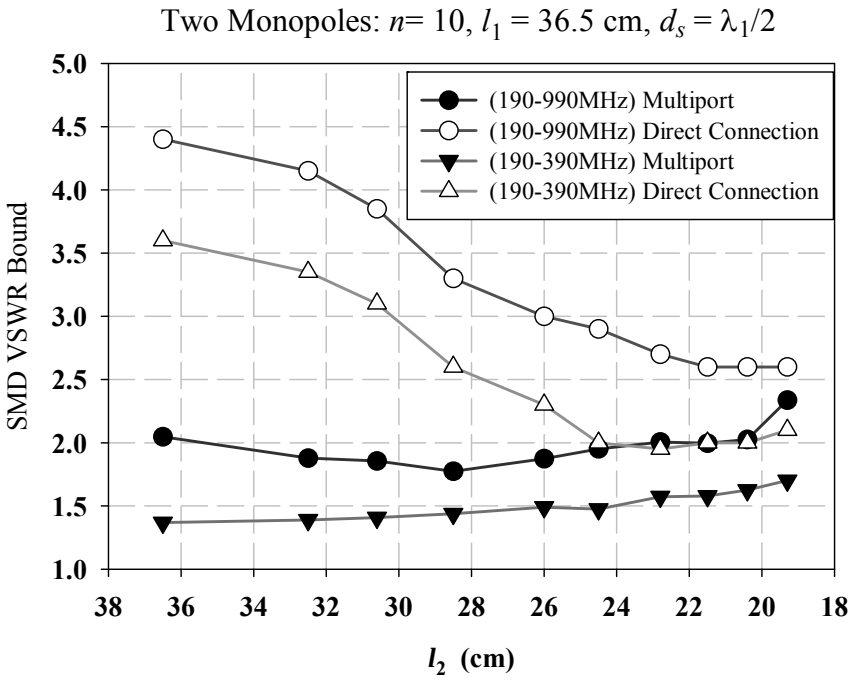

Figure 24. SMD bound and direct connection results for $d_s = \lambda_1/2$.

3.2 Network Synthesis

Section 3.1 shows how multiport impedance matching provides a good impedance match over a large bandwidth even when the antenna elements resonate at different frequencies. This section provides an overview of the network synthesis

method used to find the optimal multiport impedance matching networks and the modifications made to the algorithms to design the multiport networks.

The network synthesis algorithm uses ABCD parameters, also known as the chain or transfer matrix [37], to cascade lumped components. For the ABCD network configuration shown in Figure 25, the voltage and current relationships are given by the block matrix in (45) [37].

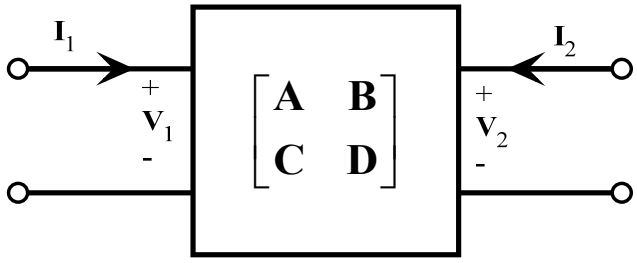

Figure 25. ABCD Matrix diagram.

$$\begin{bmatrix} \mathbf{V}_1 \\ \mathbf{I}_1 \end{bmatrix} = \begin{bmatrix} \mathbf{A} & \mathbf{B} \\ \mathbf{C} & \mathbf{D} \end{bmatrix} \begin{bmatrix} \mathbf{V}_2 \\ -\mathbf{I}_2 \end{bmatrix}. \tag{45}$$

For a two-port antenna configuration, the size of the ABCD matrix is 4 × 4, as shown in Figure 26. For one component value, there are ten possible network configurations. Each component is either an inductor or capacitor. The network configurations include:

- Series impedance in port one of the antenna load
- Series impedance in port two of the antenna load
- Shunt admittance in port one of the antenna load
- Shunt admittance in port two of the antenna load
- Shunt admittance between port one and port two of the antenna load

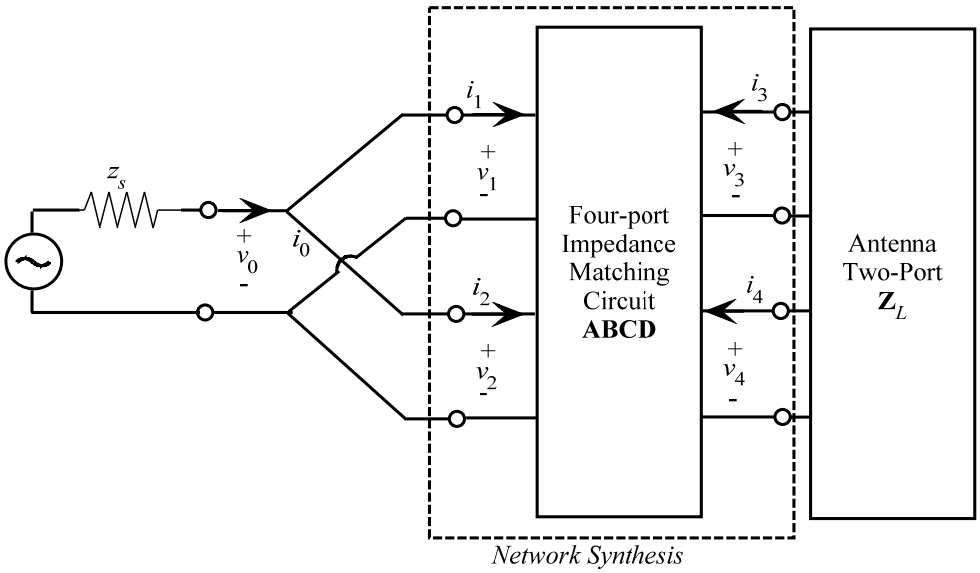

Figure 26. Cascade of the ABCD impedance matching network with the antenna load.

Figure 27 shows the ABCD parameters of the main configurations series impedance, shunt admittance in both ports, and shunt admittance between the ports. Because there are ten configurations for one component value, for n components, there are 10^n possible network configurations for the impedance matching network. The input VSWR of the network configuration is calculated by cascading the impedance matching network with the antenna load and converting the resulting two-port into a one-port as shown in Figure 26. Because $\mathbf{V}_2 = -\mathbf{Z}_L\mathbf{I}_2$, the admittance of the cascaded networks is given by

$$\mathbf{Y} = \left(\mathbf{C}\mathbf{Z}_L + \mathbf{D}\right)\left(\mathbf{A}\mathbf{Z}_L + \mathbf{B}\right)^{-1}. \tag{46}$$

Because $i_0 = i_1 + i_2$, the input current, i_0, of the resulting one-port is given by

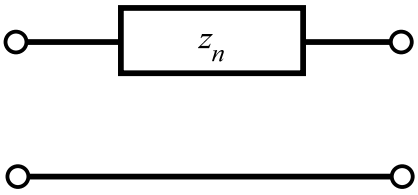

$$\begin{bmatrix} v_1 \\ v_2 \\ i_i \\ i_2 \end{bmatrix} = \begin{bmatrix} 1 & 0 & z_1 & 0 \\ 0 & 1 & 0 & z_2 \\ 0 & 0 & 1 & 0 \\ 0 & 0 & 0 & 1 \end{bmatrix} \begin{bmatrix} v_3 \\ v_4 \\ -i_3 \\ -i_4 \end{bmatrix}$$

(a) Series impedance in port one or two and the ABCD four-port matrix representation with a series impedance in both ports.

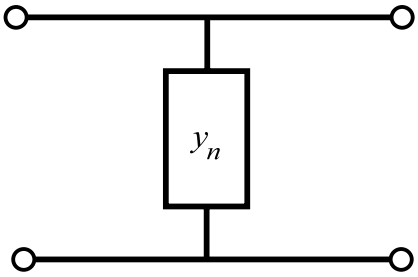

$$\begin{bmatrix} v_1 \\ v_2 \\ i_1 \\ i_2 \end{bmatrix} = \begin{bmatrix} 1 & 0 & 0 & 0 \\ 0 & 1 & 0 & 0 \\ y_1 & 0 & 1 & 0 \\ 0 & y_2 & 0 & 1 \end{bmatrix} \begin{bmatrix} v_3 \\ v_4 \\ -i_3 \\ -i_4 \end{bmatrix}$$

(b) Shunt admittance in port one or port two and the ABCD four-port matrix representation with a shunt admittance in both ports.

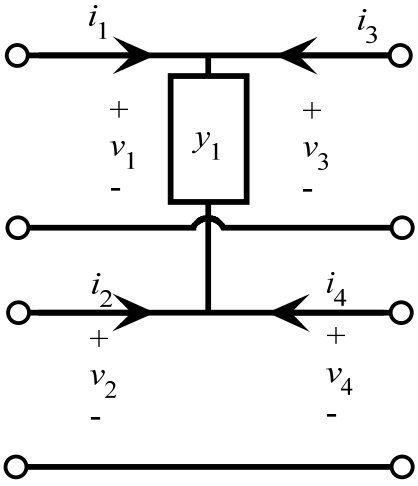

$$\begin{bmatrix} v_1 \\ v_2 \\ i_1 \\ i_2 \end{bmatrix} = \begin{bmatrix} 1 & 0 & 0 & 0 \\ 0 & 1 & 0 & 0 \\ y_1 & -y_1 & 1 & 0 \\ -y_1 & y_1 & 0 & 1 \end{bmatrix} \begin{bmatrix} v_3 \\ v_4 \\ -i_3 \\ -i_4 \end{bmatrix}$$

(c) Shunt admittance between port one and port two and the ABCD four-port representation.

Figure 27. The ABCD parameters of the three main network configurations.

$$i_0 = \begin{bmatrix} 1 & 1 \end{bmatrix} \mathbf{Y} \mathbf{V}_1. \tag{47}$$

From Figure 26, $v_0 = v_1 = v_2$ resulting in $\mathbf{V}_1^T = \begin{bmatrix} v_0 & v_0 \end{bmatrix}$. Setting $v_0 = 1$V, the input admittance is

$$y_1 = \frac{i_0}{v_0} = \begin{bmatrix} 1 & 1 \end{bmatrix} \mathbf{Y} \begin{bmatrix} 1 \\ 1 \end{bmatrix}. \tag{48}$$

For this dissertation, the network synthesis routine was modified to include transmission lines in each port. The ABCD parameters are shown in Figure 28. The transmission line length for port one is l_1 and l_2 for port two. The characteristic impedance z_0 used is 50-ohms and β is the wave number. To use the superposition method described in section 2.3, the voltages at the antenna ports are required. The voltages are calculated by

$$\mathbf{V}_2 = \left(\mathbf{A} + \mathbf{B} \left(\mathbf{Z}_L \right)^{-1} \right)^{-1} \mathbf{v}_1. \tag{49}$$

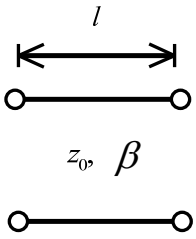

$$\begin{bmatrix} v_1 \\ v_2 \\ i_1 \\ i_2 \end{bmatrix} = \begin{bmatrix} \cos\beta l_1 & 0 & jZ_0 \sin\beta l_1 & 0 \\ 0 & \cos\beta l_2 & 0 & jZ_0 \sin\beta l_2 \\ jY_0 \sin\beta l_1 & 0 & \cos\beta l_1 & 0 \\ 0 & jY_0 \sin\beta l_2 & 0 & \cos\beta l_2 \end{bmatrix} \begin{bmatrix} v_3 \\ v_4 \\ -i_3 \\ -i_4 \end{bmatrix}$$

Figure 28. Transmission line on port 1 and port 2 and the ABCD four-port representation.

Converting the two-port into a one-port, as shown in Figure 26 may not always provide a desired solution. Alternatively, the configuration shown in Figure 29 was developed to investigate another approach for converting the two-port into a one port. In this configuration, port two is grounded resulting in

- $\mathbf{V}_1^T = \begin{bmatrix} v_0 & 0 \end{bmatrix}$
- $i_0 = i_1$
- $i_2 = 0$

Setting v_0=1V, the input admittance is

$$y_1 = \frac{i_0}{v_0} = \begin{bmatrix} 1 & 0 \end{bmatrix} \mathbf{Y} \begin{bmatrix} 1 \\ 0 \end{bmatrix}. \tag{50}$$

The configuration shown in Figure 26 is used in Chapter 3 and the configuration shown in Figure 29 is used in Chapter 4.

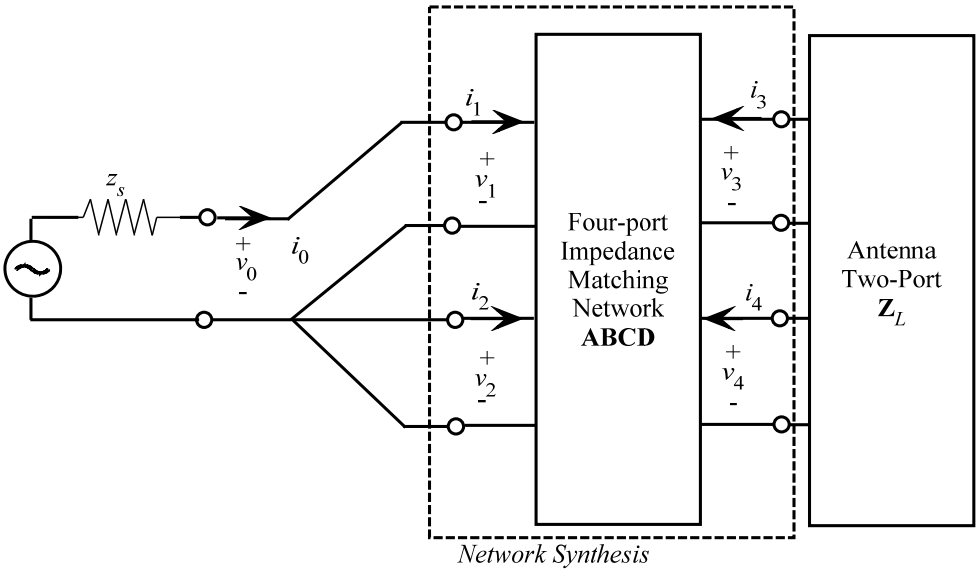

Figure 29. Cascade of the ABCD impedance matching network with the antenna load with port two shorted.

3.3 Two-Port Basic Monopole Analysis

Section 3.1 shows how multiport impedance matching can be used to maintain a reasonable VSWR when monopoles of different lengths are used. The impedance match and bandwidth of an antenna are not the only performance criteria. The radiation pattern of the antenna is also critical. The different lengths of each antenna element, the close proximity of the elements, and the phasing at each antenna port due to the impedance matching network may result in an undesirable radiation pattern. However, it may be possible to design an antenna that results in the radiation pattern desired with the correct impedance matching network.

The inter-element spacing of the antennas investigated in Section 3.1 was for λ/25 and λ/2. While λ/2 is a typical array element spacing, at λ/25 mutual coupling has a negative effect on an array performance. However, at λ/25 spacing, the antenna is capable of achieving superdirectivity. Section 2.4 describes the optimization of the input VSWR and radiation pattern.

The resonant frequencies of the monopoles studied in this section are designed for the 300 MHz frequency range. One monopole was designed with a length of 24 cm and the second monopole was designed with a length of 22 cm. An inter-element spacing of 0.05λ (5 cm) was selected.

For the analysis in this section, the dielectric constant for the transmission lines is selected as $\varepsilon_r = 1$, or air. The dielectric constant of air was selected to demonstrate the concept of using multiport impedance matching to optimize the radiation pattern, rather than to initiate a Planar Circuit Board (PCB) design. Figure 26 is the matching network configuration used for the designs in this section. From the impedance matching results, the algorithm was modified to calculate the resulting radiation pattern. The coordinate system shown in Figure 18 is the antenna configuration investigated in this section where $l_1 = 24$ cm and $l_2 = 22$ cm. The gain is optimized for $\theta = 90°$ and $\phi = 0°$. The transmission line length of 3 cm was selected for port 1 (24 cm antenna) and 1 cm for port 2 (22 cm antenna). A 1cm gap between the ports is assumed to be sufficient to accommodate the impedance matching network for these simulations. These parameters would need to be adjusted for actual implementation.

The antenna is first optimized as a single-objective optimization problem, with the objective function of VSWR. The antenna is optimize for the frequency range 280–330 MHz, a 16.4% bandwidth. The number of reactive components selected is $n = 2$. Figure 30 plots the optimized gain vs. VSWR results where each dot corresponds to a specific network topology. The gain is calculated at $\theta = 90°$ and $\phi = 0°$. From the plot, there is a matching network that attains a VSWR of 1.5 and a minimum gain of 5.9 dBi over the frequency range. This configuration is enclosed with a diamond. This matching network topology is then optimized using the GAM (see Chapter 2.4), and the component values are selected as the GAM's starting load values. From (44), the objective function is restated as

$$\text{minimize } \gamma(\mathbf{x}) = \begin{bmatrix} \gamma_1(\mathbf{x}) \\ \gamma_2(\mathbf{x}) \end{bmatrix} = \begin{bmatrix} \text{VSWR}_{\max}(\mathbf{x}) \\ -G_{\max}(\mathbf{x}) \end{bmatrix}$$
$$\text{subject to } \mathbf{x} = \begin{bmatrix} C \\ L \end{bmatrix}; \begin{array}{l} 0 \le C \le 1000 \text{ (nF)} \\ 0 \le L \le 1000 \text{ (nH)} \end{array}.$$

Because small and large values of capacitance and inductance can correspond to either an electrical short or open, the inductor and capacitor values are loosely constrained. The weight of each objective function is varied between zero and one. The squares in Figure 30 correspond to the results of the GAM for each weight configuration. These results approximate the Pareto Front discussed in Chapter 2.4. From the plot, a minimum gain of 7 dBi and VSWR = 4.75 is possible and is shown with an asterisk.

Figure 31(a) plots the radiation pattern of the multiport matching network for multiple frequencies with the original components values (VSWR = 1.6, Gain

= 5.9 dBi) while Figure 31(b) plots the maximum and minimum gain as well as the FBR of the multiport antenna. The plots show the gain varies from 5.9 dBi to 7.4 dBi and the FBR varies from 1.6–5 dB. Figure 32(a) plots the radiation of the antenna with the component values that produce a minimum gain of 7 dBi and VSWR of 4.75. The plots show there is now little variation in the gain of the antenna and the FBR improves to 4.8 dB. Figure 32(b) shows the optimized design increased the gain and FBR, in addition to minimizing fluctuations in the radiation pattern.

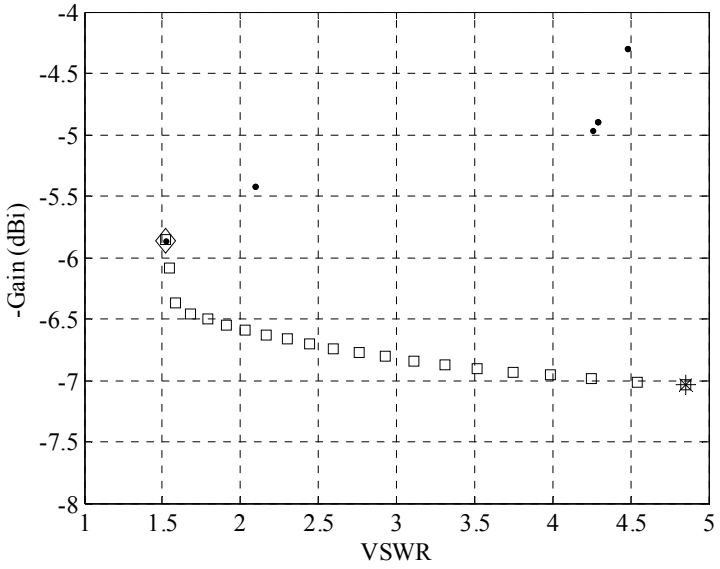

Figure 30. Optimal gain vs. VSWR for $n = 2$ (280–330 MHz).

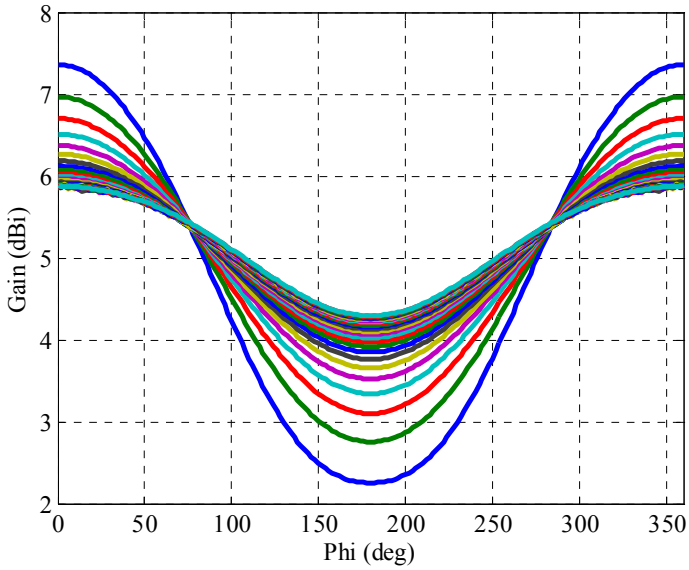

(a) Gain variations for the frequency range for 280–330 MHz.

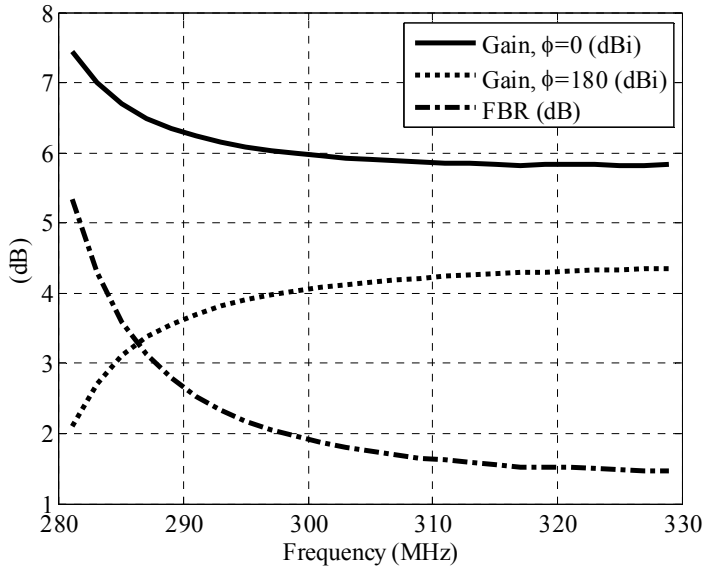

(b) Maximum, minimum, and FBR for 280–330 MHz.

Figure 31. Calculated gain patterns for the configuration enclosed in a diamond in Figure 30.

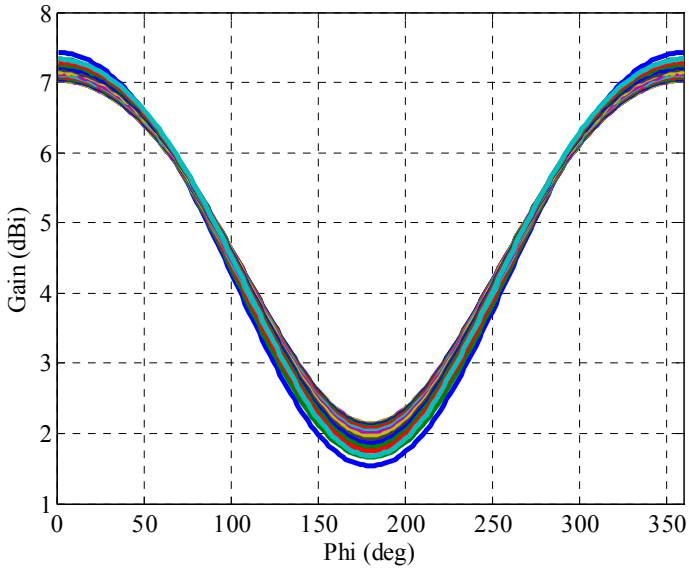

(a) Gain variations for the frequency range for 280–330 MHz.

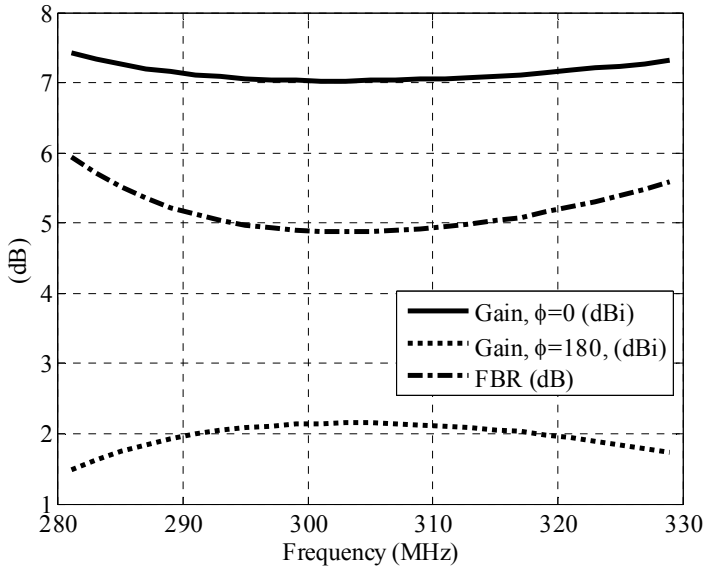

(b) Maximum, minimum, and FBR for 280–330 MHz.

Figure 32. Optimized calculated gain patterns for the configuration enclosed in an asterisk in Figure 30.

Although the gain results shown in Figure 32 are encouraging, the VSWR is large. To reduce the VSWR, traditional two-port matching after the multiport impedance matching network is investigated. The two-port matching, in

conjunction with the multiport network configuration, is shown in Figure 33. The two-port impedance matching algorithm was configured for $n = 3$, and the inductor and capacitor values were bounded as

$$0.1 \le L \le 500 \text{ (nH)}$$
$$0.1 \le C \le 500 \text{ (pF)} .$$

The results from the GAM were impedance matched with the two-port matching network. Figure 34 plots the results shown in Figure 30, along with the impedance matching results shown in circles. The impedance matching results show the optimized design with a minimum gain of 7 dBi can be matched to a final VSWR of 1.7. The final network configuration is shown in Figure 35, and the optimized VSWR results, with and without the two-port matching network, is shown in Figure 36. The input impedance was verified using ANSOFT Designer.

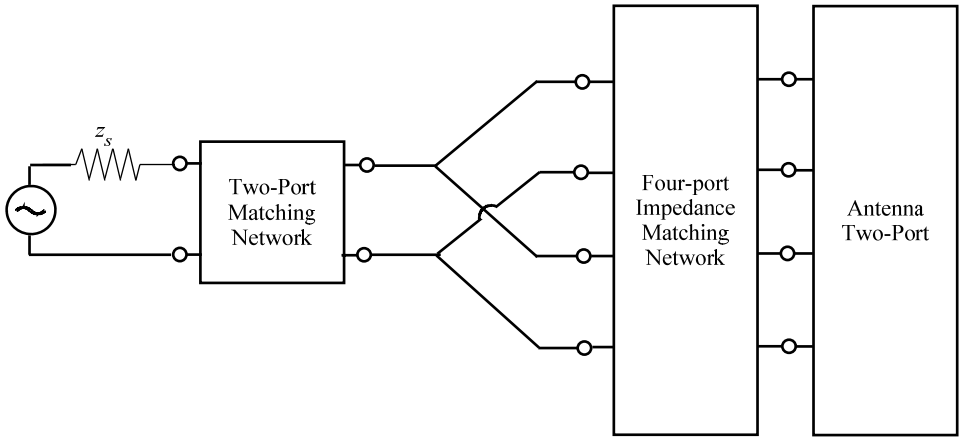

Figure 33. Cascade of two-port matching with a multiport matching network.

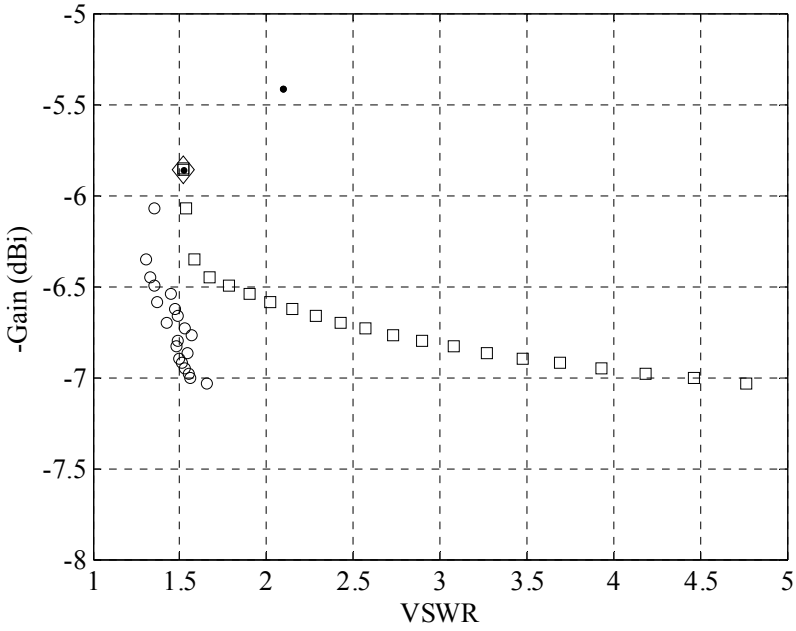

Figure 34. Impedance matched gain vs. VSWR for $n = 2$ (280–330 MHz).

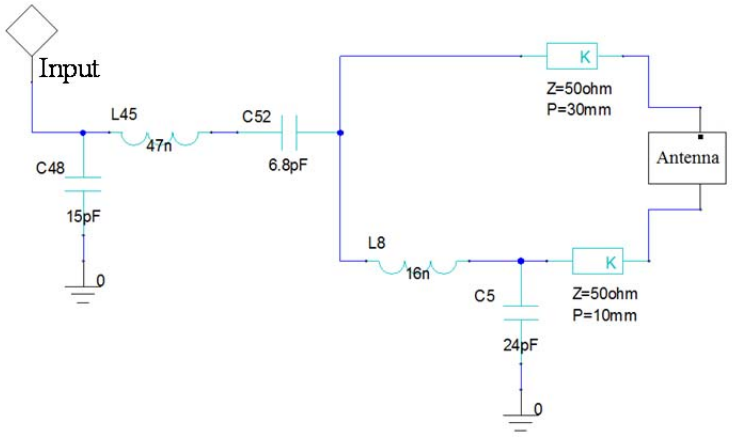

Figure 35. Ideal network design for the optimized two-port and multiport matching configuration.

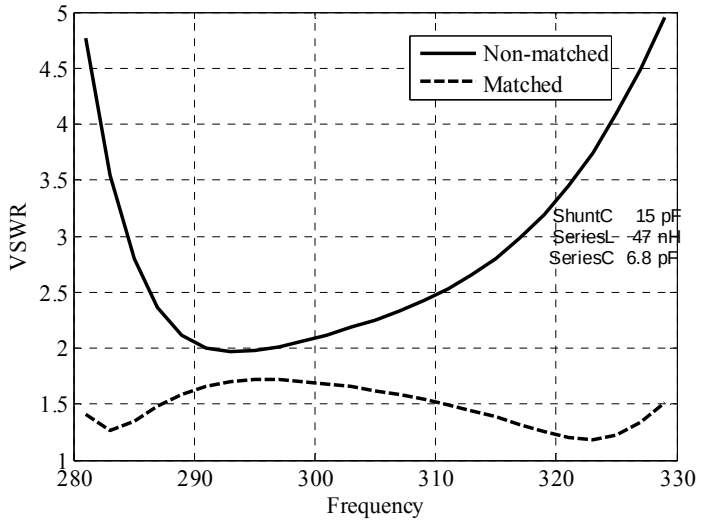

Figure 36. VSWR of the optimized impedance matched multiport antenna network of Figure 35 with and without the two-port matching network.

The multiport antenna was also optimized for $n = 5$ for the frequency range of 280–330 MHz. The number of components was increased to determine if the performance of the antenna can be improved. Figure 37 plots the resulting gain at $\theta = 90°$ and $\phi = 0°$, and VSWR for each optimized multiport impedance matching network is shown in dots. The multiport impedance matching network selected is the dot encased with a diamond because it has the smallest VSWR and largest gain combination. The impedance matching network topology and component values were then used to initialize the GAM, and the results are plotted with squares. The results from the GAM show how the algorithm only approximates the Pareto Front because some of the results are not minimal elements. The square with the asterisk is the selected network design because it maintains a VSWR less than two and a gain larger than 7 dBi. The network

topology and component values were verified in ANSOFT's Designer, and they are shown in Figure 38.

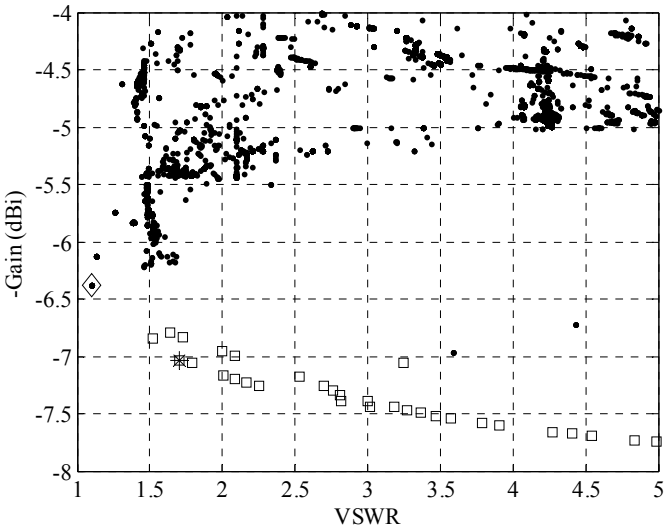

Figure 37. Optimal gain vs. VSWR for $n = 5$ (280–330 MHz).

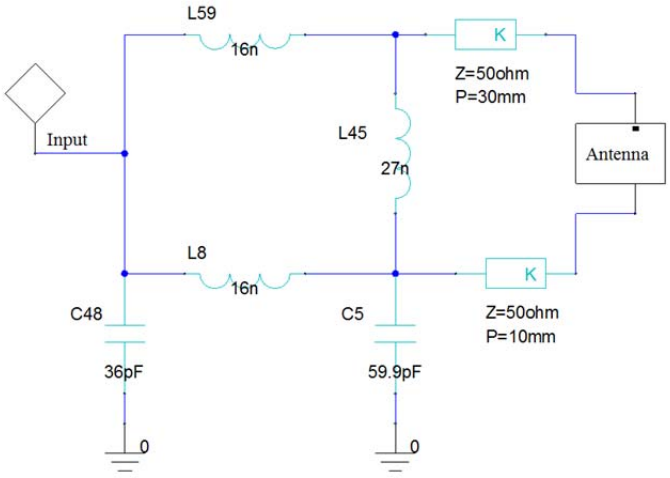

Figure 38. Optimal multiport network topology for the configuration enclosed in an asterisk in Figure 37.

For the original optimized design, enclosed in a diamond in Figure 37, has a minimum gain of 6.4 dBi with a VSWR of 1.15. The antenna maintains stable radiation patterns with an FBR of 3 dB. After optimizing for gain, the configuration enclosed in an asterisk in Figure 37, the gain is plotted in Figure 39. The antenna now has a minimum gain of 7 dBi, a VSWR of 1.75, and FBR of 5 dB. While the optimization of the multiport impedance matching network shows promise, the improvement in gain is only 2 dB. An alternative antenna design is required to attain additional gain.

An investigation into the maximum bandwidth possible for a VSWR < 2 was also investigated for $n = 5$. For 280–500 MHz, a 56.4% bandwidth, the best VSWR is 1.87. Because the VSWR is very close to 2, the impedance matching network cannot be optimized for gain without sacrificing the impedance match. Figure 40(a) shows the gain versus VSWR tradeoff. From the plot, there are several topologies that meet the VSWR < 2 criteria. The topology with the smallest VSWR was selected, and it is shown enclosed with a diamond. Figure 40(b) shows the gain at $\theta = 90°$, $\phi = 0°$, and FBR for the optimal topology. The figure shows the gain increases by 3 dB as frequency increases. Each ladder topology produces a different radiation pattern. To illustrate this, Figure 41(a) plots the gain versus VSWR plot, and the configuration enclosed with a diamond is selected. This ladder topology has a VSWR of 1.95 and produces the gain results shown in Figure 41(b). This investigation shows the antenna maintains a low VSWR by using multiport impedance matching over a large bandwidth but the radiation pattern depends on the selected network configuration.

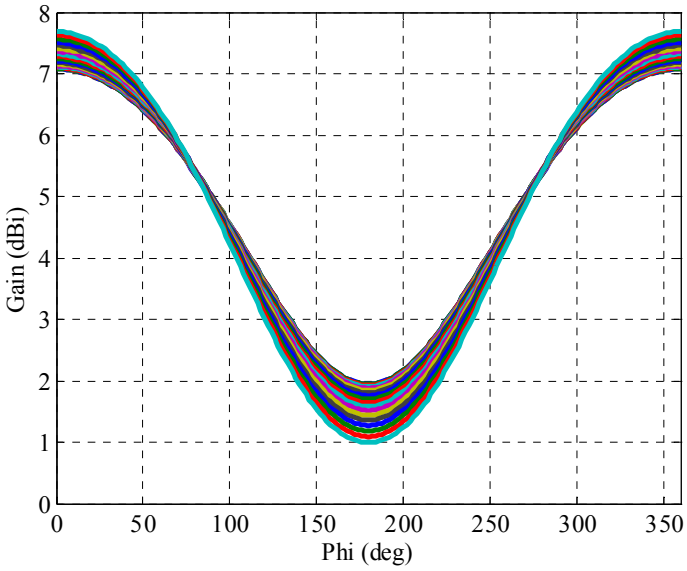

(a) Gain variations for the frequency range for 280–330 MHz.

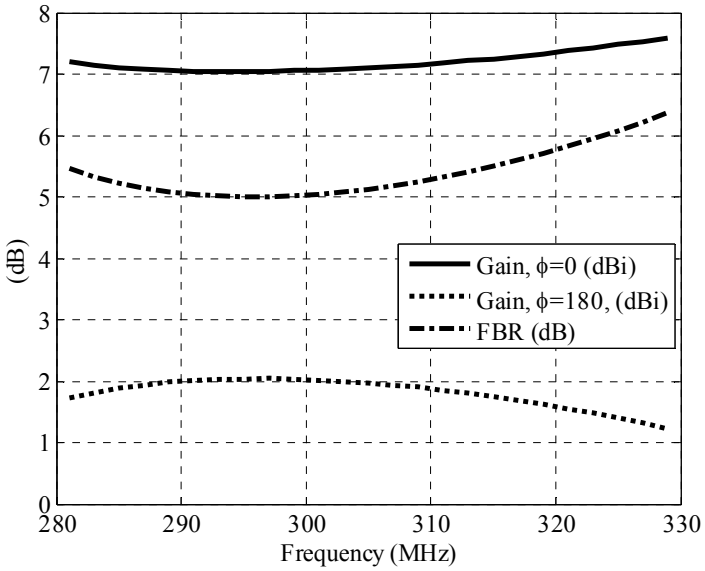

(b) Maximum, minimum, and FBR for 280–330 MHz.

Figure 39. Optimized calculated gain patterns for n = 5 (280–330 MHz).

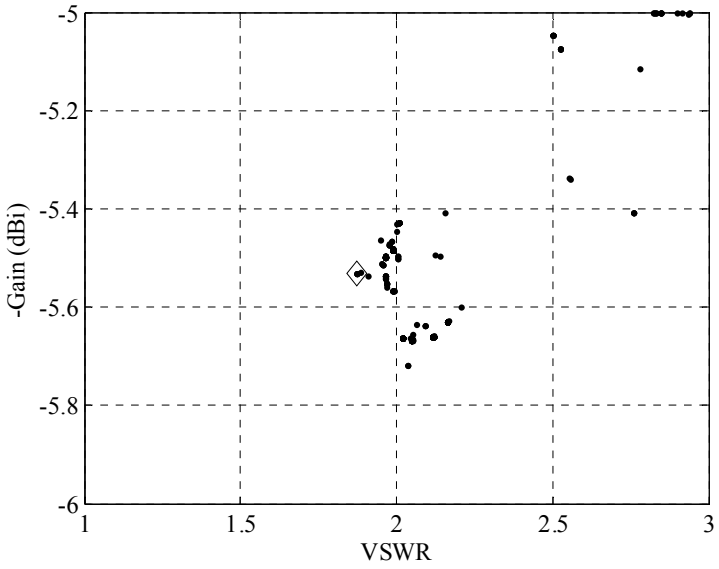

(a) Optimized multiport matched topologies

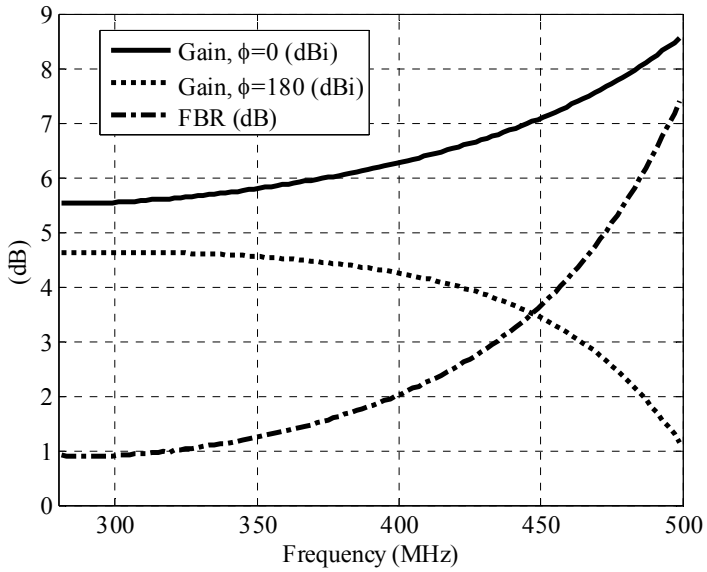

(b) The maximum, minimum, and FBR for the configuration circumscribed in a diamond in (a).

Figure 40. Calculated gain patterns for n = 5 (280–500 MHz), VSWR = 1.87.

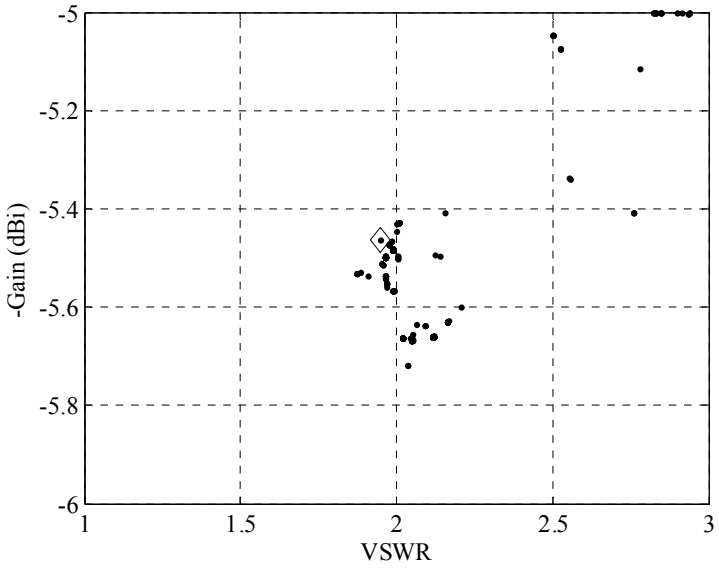

(a) Optimized multiport matched topologies

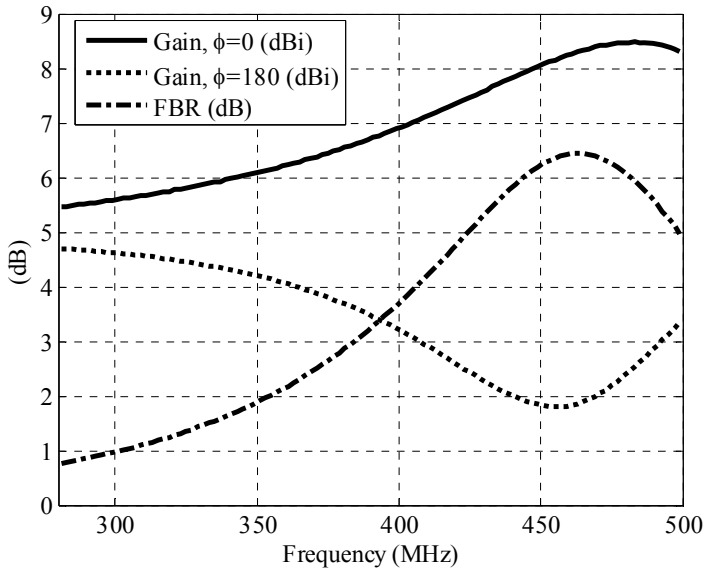

(b) The maximum, minimum, and FBR for the configuration enclosed in a diamond in (a).

Figure 41. Calculated gain patterns for n = 5 (280–500 MHz), VSWR = 1.95.

3.4 Chapter Conclusions

The theoretical study of two monopoles indicated mixed results. When there is strong coupling between two antennas and both antennas are resonating at the same frequency, the direct connection and the multiport SMD bound converge to

the same VSWR value. This result leads to the conjecture that due to the strong coupling and “fat monopole” effect, no additional benefit is gained from a multiport impedance match. When there is weak coupling between the two antennas, the multiport bound converges to a lower VSWR than the direct connection or the tightly coupled case. Multiport impedance matching allows the impedance of the antenna to be modified as such, so when the impedances add in parallel, the resulting impedance is better matched. Also, when higher order resonances are included within the bandwidth, monopoles at different resonant frequencies cause the multiport match to converge to a lower VSWR compared to the direct connection. The third order resonances, occurring at slightly different frequencies, help to decrease the VSWR. The theoretical study shows promise in the ability to attain a low VSWR over a large bandwidth using multiport impedance matching and a two-port antenna array with an electrically small inter-element spacing.

The multiport network synthesis algorithm and radiation pattern optimization were demonstrated in a two-port basic monopole configuration with limited success. The algorithms produced optimal trade-offs between VSWR and gain but the antenna array was only capable of achieving an additional 2 dB of gain. An investigation into attaining a large bandwidth with the two basic monopoles was also completed. It was shown, that while the two basic monopoles are capable of achieving a 56.4% bandwidth with a VSWR less than 2, the radiation pattern varies depending on the network topology selected. At higher frequencies, the radiation pattern becomes directional.

4. TWO-PORT THREE-FOLD MONOPOLE DESIGN

This section demonstrates how multiport impedance matching can increase the bandwidth while simultaneously maintaining a reasonable maximum gain with a proper antenna design. Rather than using basic monopoles, monopoles with three-folds are used to increase the antenna element's self-impedance. For three-folds, the antenna elements' self-impedance increases by a factor of 16 [1]. The results in this section were submitted for publicaThtion [32].

Section 4.1 is an overview of the antenna design. Section 4.2 details the optimization approach for the objective functions of VSWR and gain. A sensitivity analysis of the component value tolerances was performed of the optimized network topology to determine the sensitivity of the components to VSWR and Gain. Section 4.3 details the PCB design, fabrication, impedance, and gain measurements. The chapter conclusions are given in section 4.4.

4.1 Antenna Configuration

In [13], a two-element superdirective antenna was designed with 0.1 λ inter-element spacing. The antenna uses tuning capacitors to cancel the antenna element reactance and impedance match the antenna array. With this technique, the antenna array achieved a 1.7% bandwidth and VSWR of 2:1. This section investigates the concept of using a multiport impedance matching network to attain a broader bandwidth while simultaneously maintaining a high absolute gain.

The antenna design used to demonstrate the multiport impedance matching network originates from the antenna design in [13]. The antenna dimensions are:

- 0.236 λ in height
- 0.0094 λ spacing between folds
- 0.1 λ inter-element spacing

For the design in this section, the antenna was scaled to operate at 300 MHz, a one-meter wavelength. The height of one antenna was kept at 23.6 cm and the second was modified to a height of 22 cm. The height of the second antenna element was reduced to provide a better impedance match and higher gain with the multiport impedance-matching network. Brass tubing with a diameter of 3.2 mm was used to fabricate the antenna. Figure 42 shows the fabricated antenna array and depicts the coordinate system. The 23.6 cm antenna is on the –x-axis and the 22 cm antenna is on the +x-axis; the antenna element spacing remained at 0.1 λ. The element spacing is measured as the distance between each fed element.

4.2 Optimization and Sensitivity

This section describes the multiport impedance matching network design. Figure 13 shows a network description of the antenna configuration for an *N*-port antenna with an (*N*+1)-multiport impedance matching network. In the network description, **Y** represents the admittance of the multiport impedance matching network while $\mathbf{Y}_L$ denotes the antenna admittance matrix. The voltage at each

antenna element is given by (29) and the input admittance, y_1, is represented by (30).

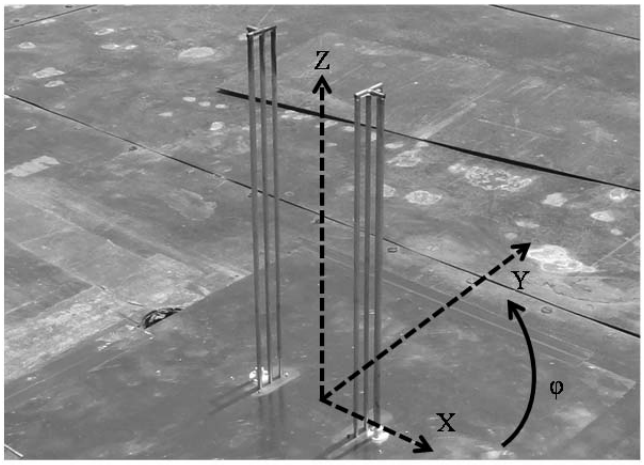

Figure 42. Antenna photograph of two-port three-fold antenna and coordinate system description.

The multiport matching network must simultaneously minimize the VSWR and maximize the gain of the antenna. This problem is formulated as a multi-objective optimization problem with two objective functions, $\gamma(\mathbf{x})$: VSWR and gain. Chapter 2.4 reviews the optimization methods used in this dissertation. In optimization problems, the objective function is traditionally minimized. Therefore, to maximize the antenna array gain, the goal is to minimize the negative of gain (in decibels). For the frequency band B, the objective functions are restated from Chapter 2.4

$$\text{minimize } \gamma(\mathbf{x}) = \begin{bmatrix} \gamma_1(\mathbf{x}) \\ \gamma_2(\mathbf{x}) \end{bmatrix} = \begin{bmatrix} \text{VSWR}_{\max}(\mathbf{x}) \\ -G_{\max}(\mathbf{x}) \end{bmatrix}.$$

For a 2-port ladder topology, there are 10^n possible ladder topologies; where n is the number of lumped elements in the topology. Section 3.2 reviews

the network synthesis approach. Therefore, to simplify the optimization problem, rather than optimizing both objective functions, the first objective function, $\gamma_1(\mathbf{x})$, is first optimized for a specific number of lumped elements. Figure 29 shows the network configuration used in the optimization routine.

After optimizing each ladder topology to minimize the input VSWR into the antenna, the resulting gain for each topology is calculated. The antenna gain is calculated by applying the superposition method described in 2.3 and using the calculated electric field of each antenna element. This computation requires the voltages at each port, computed from (29) and constraining v_1 to 1V.

The multiport impedance matching network was selected to include four lossless lumped elements and two 50-ohm, 47.5 mm in length transmission lines to connect both ports together. Both simulation and fabrication used Rogers RT/Duroid 5880 board with a thickness of 31 mils. The antenna input impedance was optimized for the frequency range B = 301−319 MHz; a 5.8% bandwidth. Given the coordinate system shown in Figure 42, the antenna gain is calculated at $\theta = 90°$ and $\phi = 0°$. The results of optimizing the first objective function and the corresponding antenna gain are plotted in Figure 43. The scaling in the plot is constrained to those matching networks that produce a gain greater than 5 dBi with a VSWR less than 5. Every black dot corresponds to a specific ladder topology. The black dot circumscribed in a diamond is the ladder topology selected for design and fabrication. There are two other topologies that produce a gain greater than 9 dBi and a VSWR less than two but the topology selected was

the least sensitive to the component values and the component values where easier to realize.

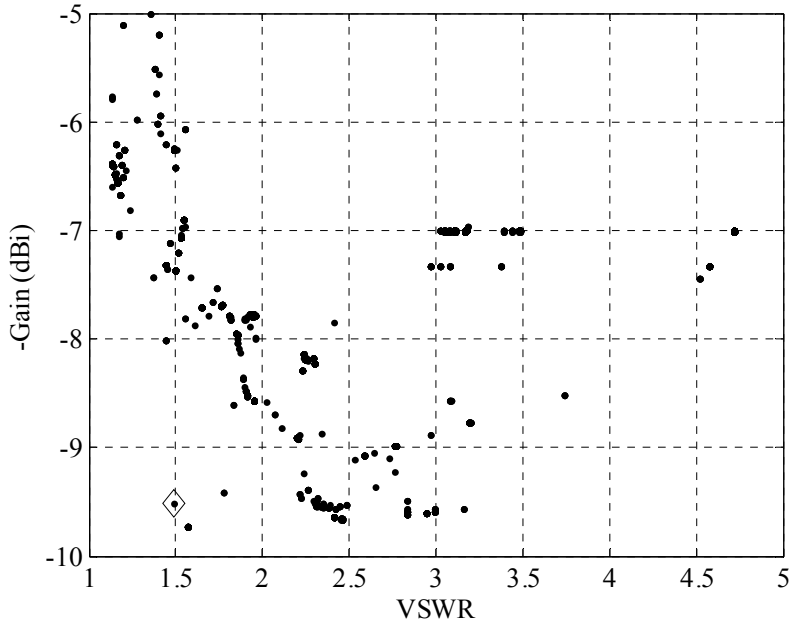

Figure 43. Minimum gain between 301–319MHz for all multiport impedance matching networks with three components for the two-port three-fold antenna.

The selected optimized network topology consists of L_1 = 4.56 nH, L_2 = 102.2 nH, C_1 = 17.8 pF, and C_2 = 56.9 pF. The optimized lumped elements are rounded to the closest available capacitor and inductor from available kits except for L_1, resulting in the revised values of: L_1 = 4.56 nH, L_2 = 100 nH, C_1 = 18 pF, and C_2 = 56 pF. Figure 44 is a network schematic of the optimized network topology in ANSOFT's Designer. The inductor L_1 was left as is because the nearest inductor values available from the kits would degrade the input VSWR of the antenna. This network topology includes only ideal components. The impedance of the ideal network is plotted in Figure 45.

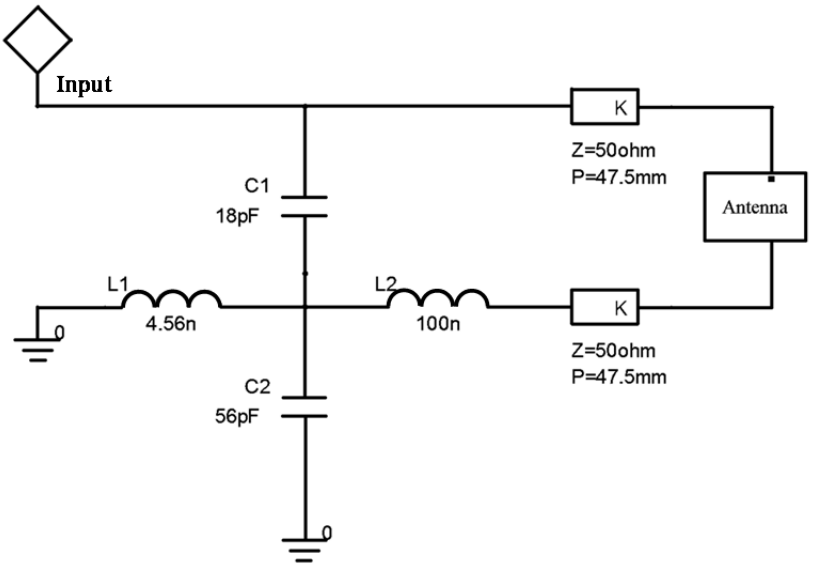

Figure 44. Ideal network topology for the selected multiport ladder shown in Figure 43.

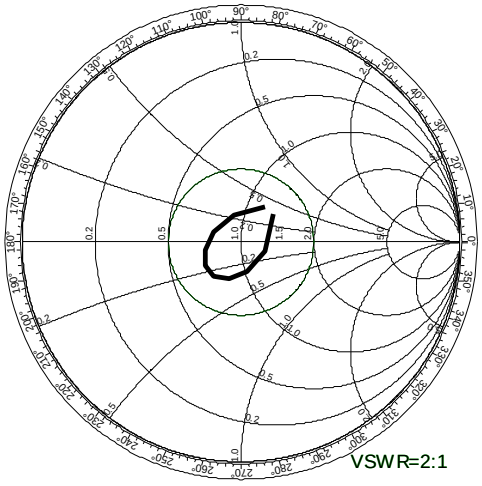

Figure 45. Impedance of the two-port three-fold antenna with ideal multiport network for the frequency band *B*

To study the network sensitivity to the tolerance of the components, the cumulative distribution function (CDF) was calculated for the ideal network topology and component values with 2%, 5%, and 10% tolerance. The study was

constrained to the frequency band *B* (301−319 MHz). The CDF plot for VSWR sensitivity is shown in Figure 46 and for gain sensitivity in Figure 47. The results show the network's ability to maintain a low VSWR is sensitive to the tolerance of the component values but the gain is not. The tolerance of the component values can readily shift the array's impedance outside the VSWR 2:1 circle. For a 50% probability of attaining a VSWR less than two, the 2% and 5% tolerance values are able to maintain the low VSWR. For a tighter probability of 90%, the 2% tolerance components are the only ones capable of achieving the low VSWR of less than 2. The gain on the other hand, only varies by a fraction of a dB for each configuration.

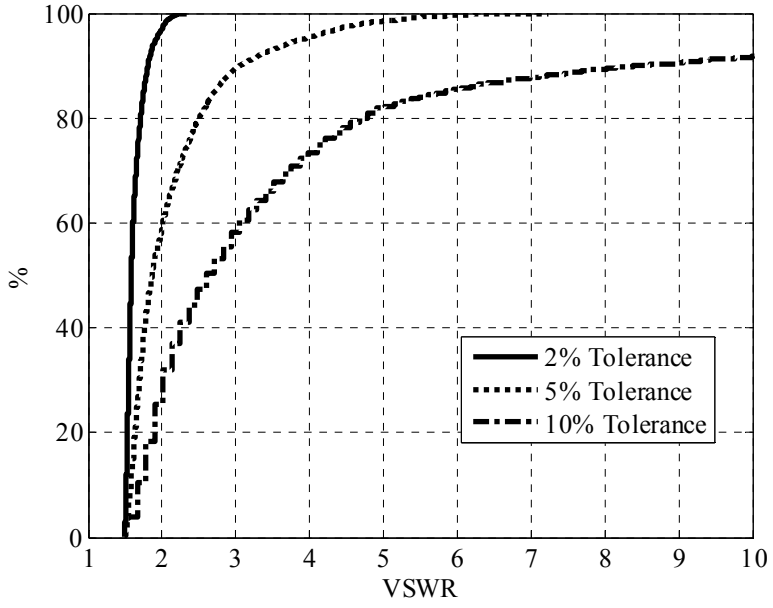

Figure 46. VSWR CDF of the ideal multiport network with 2%, 5%, and 10% tolerance component values for the two-port three-fold monopole array.

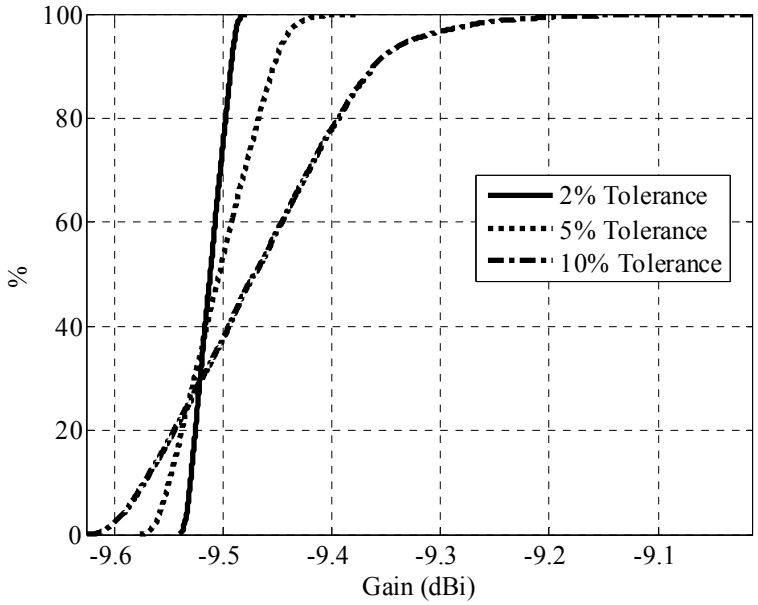

Figure 47. Gain CDF of the ideal multiport network with 2%, 5%, and 10% tolerance component values.

To determine which component is the most sensitive, the CDF was calculated by varying each individual component while fixing all other components. The results for the 10% tolerance configuration are shown in Figure 48. The figure shows that L_1 and C_2 are the most sensitive components while C_1 is the least sensitive.

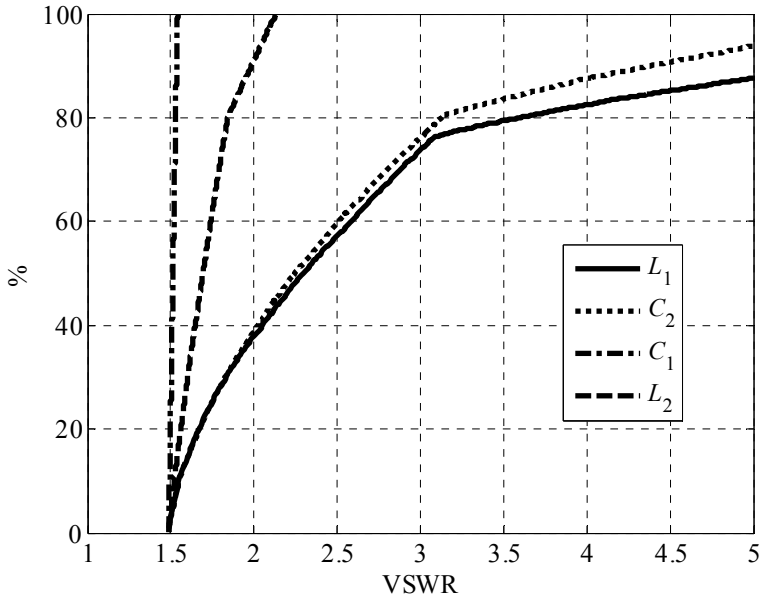

Figure 48. VSWR CDF of the ideal multiport network for each individual component with a 10% tolerance.

4.3 PCB Design and Measurements

Next, an Electromagnetic (EM) examination determined parasitic and transmission line effects. This study used Planer EM in ANSOFT Designer. The *S* parameters of L_2 from the manufacturer were imported into the simulation. The *S* parameters of the capacitors were not readily available, and therefore the EM simulation used ideal capacitors. The simulation first investigated the required, L_1, inductor value to maintain a small input VSWR of the antenna while taking into consideration the component footprints and parasitic effects. To maintain a small VSWR over the frequency band, the network required a value of 3.5 nH for L_1, a reduction in inductance value of 23% from the original value. The significant reduction in inductance value demonstrates the importance of simulating the component footprints and transmission lines. Rather than using a lumped

component to achieve the small inductance value, a shunt transmission line is used. Figure 49 shows the final design schematic, where L_1 is designed as a shunt transmission line 18.25mm long. The fabricated network is shown in Figure 50.

From the EM simulation, losses introduced by the network can be incorporated into the superposition method to determine the resulting gain from the board layout. The antenna gain is calculated using the input power of the network, $P_{in} = \frac{1}{2}\,\mathrm{Re}(v_1^2 y_1)$, as given below rather than using the input power at each individual port as described in section 2.3,

$$G(\theta,\phi) = \frac{4\pi r^2}{\eta} \frac{\left| \sum_{n=1}^{N} v_n E_n^{sc}(r,\theta,\phi) \right|^2}{\mathrm{Re}\left(v_1^2 y_1\right)}, \tag{51}$$

where η is the intrinsic impedance of the medium.

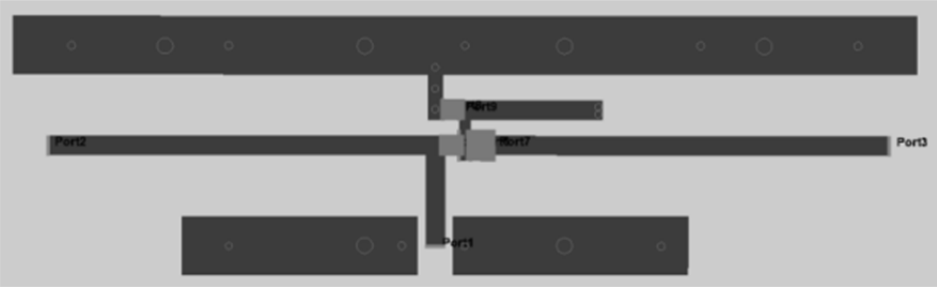

Figure 49. EM Model of the multiport network topology shown in Figure 44.

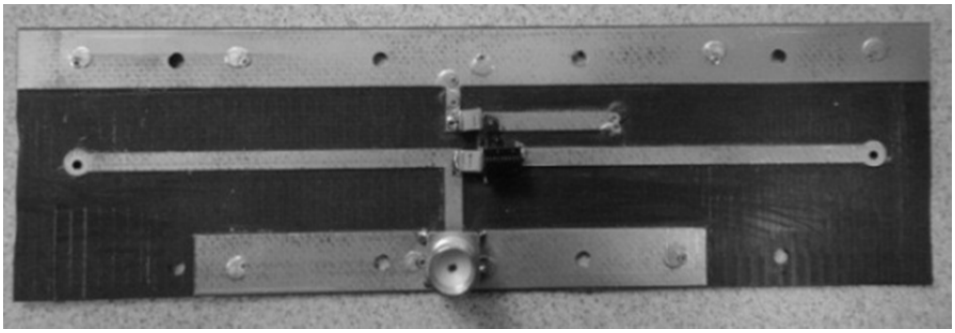

Figure 50. Fabricated PCB of the multiport network topology shown in Figure 44.

The PCB in Figure 49 was fabricated and a photograph of the assembled PCB is illustrated in Figure 50. The capacitors used have a 5% tolerance and the inductor has a 2% tolerance value. The circuit board was soldered to the feed point of each antenna element shown in Figure 51. Brass screws attached the circuit board ground to the antenna ground plane for both ground continuity and structural support. The circuit board fabrication used a milling machine that does not have as tight tolerances as other fabrication methods. The measured input impedance was not well matched to the antenna and C_2 was interchanged from 56 pF to 47 pF for better matching. These differences are primarily due to the fabrication tolerances of the circuit board, maintaining ideal capacitors in the simulation, fabrication tolerances of the antennas, component tolerance and additional parasitic effect the EM simulation does not take into consideration such as solder.

Figure 51. Fabricated multiport network integrated with the two-port three-fold antenna.

Figure 52 shows the antenna VSWR for the ideal network, the EM simulation, and the measured data. The plot shows the differences between the ideal configuration and that actually measured. The rounding of the lumped elements to available components had a minimal impact on the ideal network's VSWR. With the inclusion of the footprints for the components, the EM simulation shows a contraction in bandwidth. The contraction is due to the parasitic effects that the ladder optimization algorithm does not take into account. The footprints add additional capacitance and inductance. The VSWR 2:1 bandwidth is 6.14%, as opposed to the ideal network of 6.9%. The plot also shows that designing a shunt transmission line, in lieu of the inductor, has a minimal impact to the VSWR performance of the antenna. The measured VSWR has a slightly wider bandwidth. The increase in bandwidth is primarily due to the

difference between the EM simulation and the fabricated PCB board that required C_2 to be interchanged from 56 pF to 47 pF. The antenna maintains a VSWR less than 2 from 296−321 MHz; an 8.1% bandwidth.

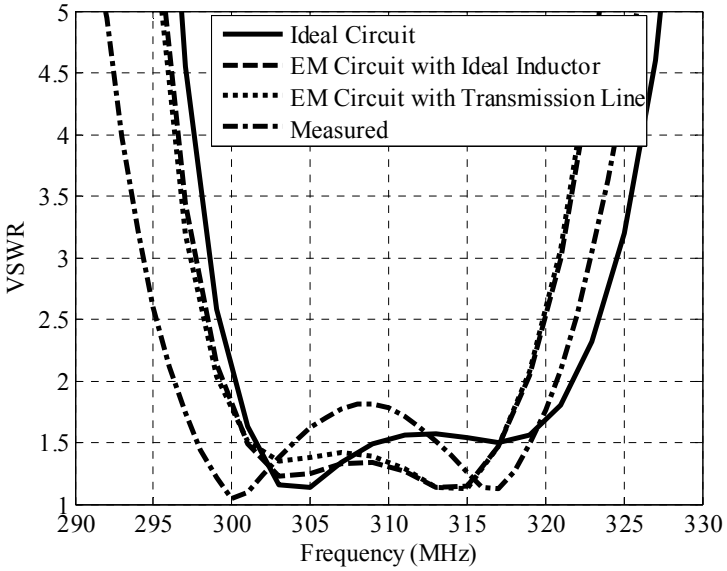

Figure 52. VSWR of the two-port three-fold antenna array with the ideal multiport network, the EM network design, and with the fabricated measured network as shown in Figure 51.

The absolute gain of the antenna was measured in an outdoor antenna pattern range. Figure 53 exhibits the antenna's absolute gain of the ideal network, EM simulation, and measured data. There are some notable differences between the predicted absolute gain with the ideal network, the EM simulations, and the measurements. The inclusion of the footprints for the components created sufficient parasitic effects that the absolute gain bandwidth of the antenna was reduced. Interchanging the ideal inductor with the shunt transmission line showed minimal differences between both simulations. For an absolute gain greater than 9 dBi, the ideal network has a 7.87% gain bandwidth and the EM network has a

5.97% gain bandwidth. The measured absolute gain is approximately 0.5 dB less than the absolute gain predicted by the EM simulation. The reduction in absolute gain is most likely due to the need to interchange the C_2 for impedance matching and the inability to incorporate realistic capacitor models into the simulation to incorporate the additional losses. For a measured absolute gain greater than 8.9 dBi, the antenna has a 5.8% gain bandwidth. The achieved gain bandwidth is less than the impedance bandwidth.

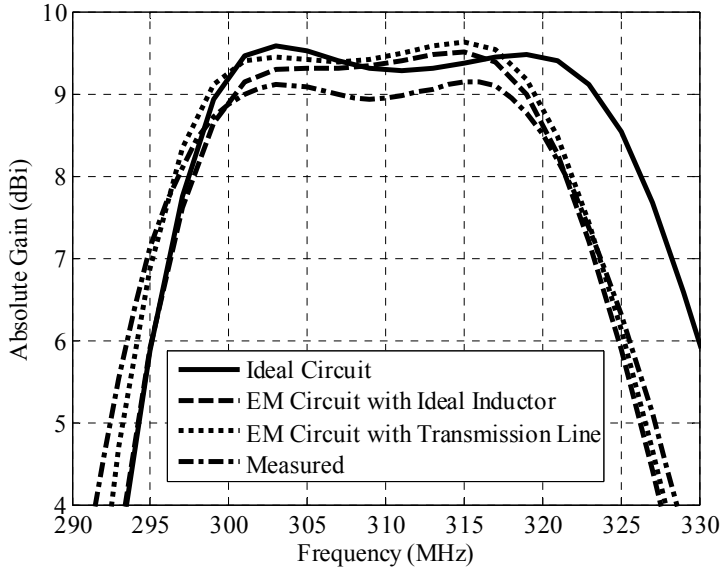

Figure 53. Absolute gain of the two-port three-fold antenna array design with the ideal network multiport matching network, the EM network design, and with the fabricated measured network.

4.4 Chapter Conclusions

Chapter 3 showed a two-port basic monopole configuration that was only capable of achieving an additional 2 dB of gain. To improve the gain performance, a two-port antenna array with three-folds in each antenna element was used in conjunction with multiport impedance matching. The impedance

matching network simultaneously matched the input impedance and provided the appropriate phase difference for maximum gain. The antenna achieved an absolute gain of 8.9 dBi for a 5.8% bandwidth. The bandwidth is 3.4 times greater than the original design from [13] at a reduction of 1.26 dB less gain than the directivity of the original design. To realize the multiport feed network, careful consideration is required in the design of the component layout and interconnections.

5. THREE-PORT YAGI–UDA ANTENNA

This chapter investigates an alternative method to achieve superdirectivity by adding an additional element and arranging the antenna elements in a Yagi–Uda configuration. Section 1.3 provides a review of the Yagi–Uda antenna design along with recent work using multi-objective optimization. The three-port Yagi–Uda antenna achieves similar directivity than that of a two-port but without increasing the overall footprint of the antenna array. The inter-element spacing is ~0.05λ. The Yagi–Uda antenna approached superdirectivity for an unprecedented measured 12% VSWR 2:1 bandwidth. The results of this chapter were published in [34].

Section 5.1 is an overview of the antenna design configurations investigated, the design approach, and the VSWR and the absolute gain predictions for each configuration. Section 5.2 investigates the impedance and phase of each element to provide insight into the improved performance of the Yagi–Uda antenna. Section 5.3 contains the measure VSWR and absolute gain for two of the configurations studies. The chapter conclusions are found in section 5.4.

5.1 Antenna Configuration

Chapter 4 shows how a two-element antenna array is capable of achieving an absolute gain of 8.9 dBi for 5.8% bandwidth. The inter-element spacing is 0.1λ. This section shows that by adding an additional element and maintaining the overall antenna footprint length, the bandwidth of the antenna is increased. The

antenna is designed in a Yagi–Uda configuration offering a multi-objective trade-off between VSWR, bandwidth, and gain.

The Yagi–Uda antenna consists of a driven element, a director, and a reflector. The inter-element spacing determines the mutual impedance between the elements. Figure 54 is a network description of the antenna configuration for a driven antenna with N parasitic shorted elements. The impedance relationship between the driven element and parasitic elements is denoted by the matrix $\mathbf{Z}$. The relationship between the impedance matrix, the voltage, and the currents at each input port is given by the block matrix

$$\begin{bmatrix} v_1 \\ \mathbf{V}_2 = 0 \end{bmatrix} = \begin{bmatrix} z_{11} & \mathbf{Z}_{12} \\ \mathbf{Z}_{21} & \mathbf{Z}_{22} \end{bmatrix} \begin{bmatrix} i_1 \\ \mathbf{I}_2 \end{bmatrix}, \tag{52}$$

where

- z_{11} is a 1×1 scalar
- $\mathbf{Z}_{12}$ is an 1×N vector
- $\mathbf{Z}_{21}$ is an N×1 vector
- $\mathbf{Z}_{22}$ is an N×N matrix
- $\mathbf{I}_2$ is an N×1 vector.

The voltage at each of the parasitic shorted elements is zero and port 1 is the driven element. The input impedance, z_1, is given by

$$z_1 = z_{11} - \mathbf{Z}_{12} \left(\mathbf{Z}_{22} \right)^{-1} \mathbf{Z}_{21}, \tag{53}$$

where z_{11} is the self-impedance of the driven element, $\mathbf{Z}_{22}$ is the self-impedance of the parasitic elements, and $\mathbf{Z}_{12}$ is the mutual impedance between the elements. The input current at each port of the parasitic antennas is given by

$$\mathbf{I}_2 = -\left[\left(\mathbf{Z}_{22}\right)^{-1}\mathbf{Z}_{21}\right] i_1. \tag{54}$$

Note the input current is defined as going into the antenna but the current actually flows in the opposite direction.

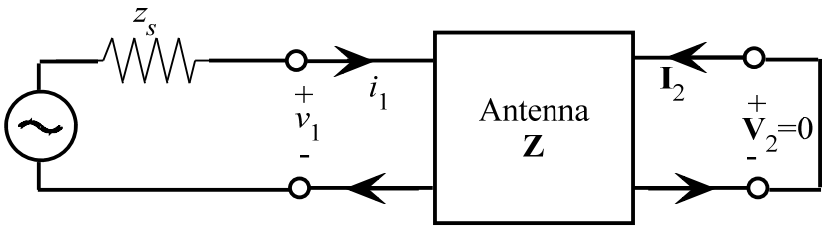

Figure 54. Antenna network configuration for the three-port Yagi–Uda.

For the case when the antenna has only one parasitic element, director or reflector, the antenna can be modeled as a two-port device and the input impedance is

$$z_1 = z_{11} - \frac{z_{12}z_{21}}{z_{22}}. \tag{55}$$

The relationship between the input current in port 1 and the current in the parasitic element, port 2, is

$$i_2 = -\frac{z_{21}}{z_{22}} i_1. \tag{56}$$

The difficulty to attain a well-matched antenna is revealed in (55). The self-impedance of the driven element is subtracted by the ratio of the mutual impedance between the elements and the self-impedance of the parasitic element.

As the inter-element spacing between the radiators decreases, the mutual impedance approaches the self-impedance of the radiators and the input impedance of the energized element approaches zero.

The proposed Yagi–Uda antenna in this section is a three-port device with the input impedance

$$z_1 = z_{11} - \frac{1}{z_{22}z_{33} - z_{23}^2}\left(z_{12}^2 z_{33} - 2z_{12}z_{13}z_{23} + z_{13}^2 z_{22}\right). \tag{57}$$

The current at port 1 and those at ports 2 and 3 are related by

$$i_2 = \frac{1}{z_{22}z_{33} - z_{23}^2}\left(z_{12}z_{33} - z_{13}z_{23}\right)i_1, \tag{58}$$

$$i_3 = \frac{1}{z_{22}z_{33} - z_{23}^2}\left(z_{13}z_{22} - z_{12}z_{23}\right)i_1. \tag{59}$$

Unlike the input impedance of the two-port antenna configuration in (55), the mutual-impedance contribution consists of three terms. Two of the terms subtract from self-impedance of the driven element while one of the terms adds to the self-impedance. By optimizing the spacing between the antenna elements and the self-impedance of each radiator, the effects of the mutual coupling on the self-impedance of the driven element can be controlled. This concept is similar to that proposed in [35] to decouple two closely spaced driven dipoles by placing a parasitic dipole with a reactive load in-between the two dipoles.

The compact Yagi–Uda antenna design consists of a driven element, a director, and a reflector. The inter-element spacing was selected as 5 cm or 0.053λ at 315 MHz. The driven-element is a folded monopole. A quarter-wave monopole on an infinite ground plane has an impedance of 36.5+*j*21.25ohms. With initial

impedance less than 50 ohms, any further reduction in impedance will greatly reduce any possibility of attaining a low VSWR over a significant frequency range. Therefore, the monopole has one fold to increase the self-impedance by a factor of 4 [1]. The folded monopole is 21 cm in length and 5 cm wide. The director and reflector were designed as a bowtie monopole to increase the bandwidth and attain the self-impedance needed to optimize the driving-point impedance and gain. The bowties are 6 cm wide and each length investigated for the reflector and director is tabulated in Table 2. The coordinate systems used is illustrated in Figure 55. A photograph of the fabricated antenna is shown in Figure 56. The driven element is centered on the *x*-*y* plane, the director element is along the +*x*-axis while the reflector is along the –*x*-axis.

Table 2. Reflector and Director Height Configurations Investigated.

	Reflector	**Director**
A	19 cm	16.5 cm
B	19.5 cm	16.5 cm
C	20 cm	16.5 cm
D	19.5 cm	17 cm

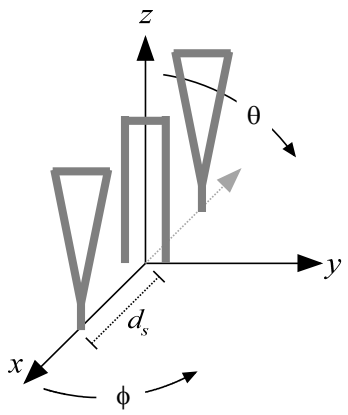

Figure 55. Yagi–Uda coordinate systems.

Figure 56. Fabricated compact Yagi–Uda antenna.

Table 2 lists the dimensions of four different antenna configurations. These configurations demonstrate the trade-off between gain and bandwidth. The maximum gain as a function of frequency is plotted in Figure 57 for each configuration. Each antenna configuration displays two peaks. One peak is near the director's resonant frequency and the other peak is near the reflector's

resonant frequency. The gain at each peak is approximately 10.3 dBi. The maximum theoretical directivity of two monopoles is 10.5 dBi [9]. Figure 57 shows how the frequency range between the peaks can be varied by modifying the resonance of each parasitic element. As the frequency range between the peaks increases, the dip in between the peaks also increases. For example, the difference in gain between the peak and dip in configuration A is approximately 0.5 dB and 1 dB for configuration C.

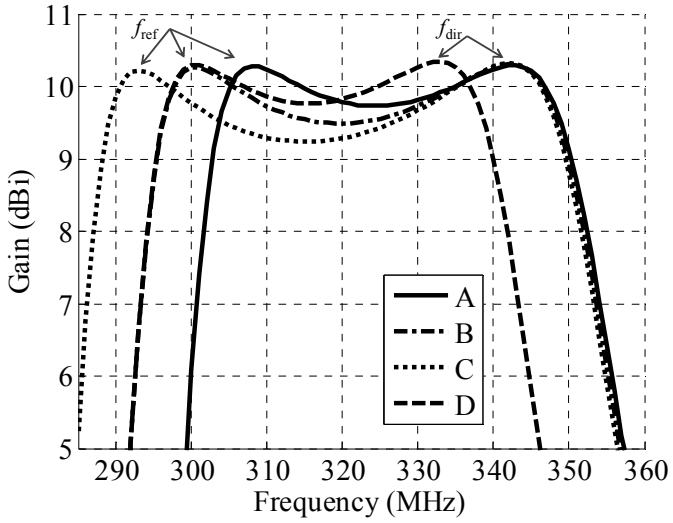

Figure 57. Maximum gain of the compact Yagi–Uda antenna.

The VSWR for all four configurations is shown in Figure 58. For a 2:1 VSWR bandwidth, configuration A has 7%, B has 8.6%, C has 10.2%, and D has 4.2%. Configuration C has the largest bandwidth while configuration D has the smallest. While configuration C achieves the maximum 2:1 VSWR bandwidth, configuration C has approximately 0.5 dB lower gain than that of configuration A.

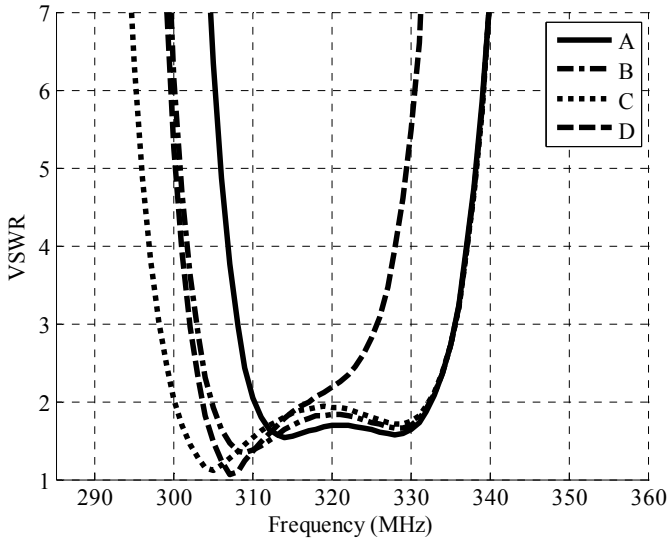

Figure 58. VSWR of the compact Yagi–Uda antenna.

The absolute gain for each configuration is shown in Figure 59. With the inclusion of the mismatch loss, there is a 0.7 dB difference in the maximum absolute gain between configurations A and C. Configuration C has a maximum absolute gain of 9.5 dBi and minimum absolute gain of 8.8 dBi between the peaks. Configuration A on the other hand has a maximum absolute gain of 9.9 dBi and a minimum absolute gain of 9.5 dBi between the peaks.

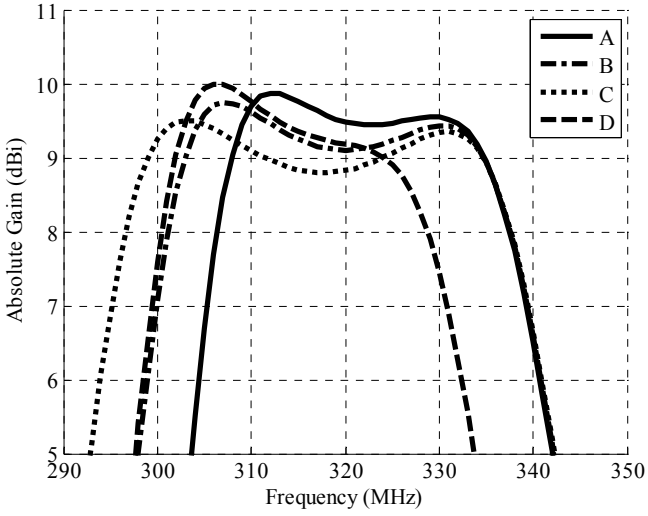

Figure 59. Absolute gain of the compact Yagi–Uda antenna.

5.2 Impedance and Phase Investigation

To investigate the antenna behavior in terms of impedance bandwidth and gain, (57) is decomposed to determine the behavior of each term and the phase difference between the driven element and the director and reflector from (58) and (59).

The impedance behavior is first investigated. The driving point impedance in (57) is calculated from the self-impedance of the driven element subtracted by the mutual impedance effects of the parasitic elements. The mutual impedance effects contain three terms. For configuration C, the resistance and reactance of the driving point impedance, self-impedance, and mutual impedance effects are plotted in Figure 60(a) and (b), respectively. The resistance plot shows the mutual resistance effects approach the self-impedance of the driven element at frequencies below 290 MHz and greater than 340 MHz, leading to very small

input resistance values. Between 290 MHz and 340 MHz, the contribution of the mutual resistance effects to the input resistance is decreased; the input resistance is therefore increased. The reactance plot shows the dual resonance effects produced by the parasitic elements.

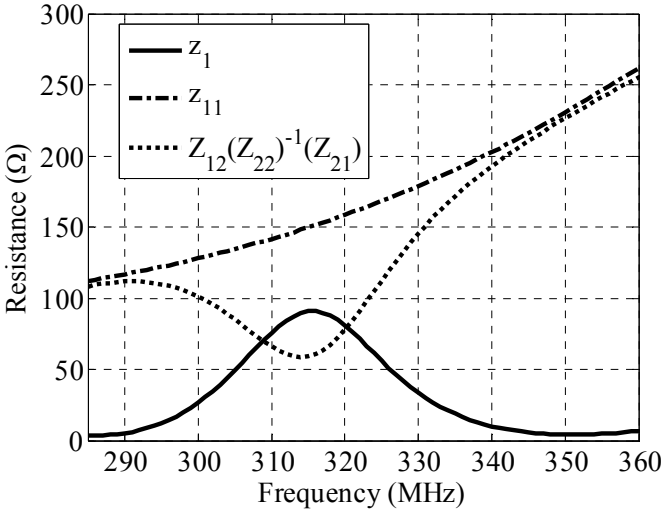

(a) Resistance

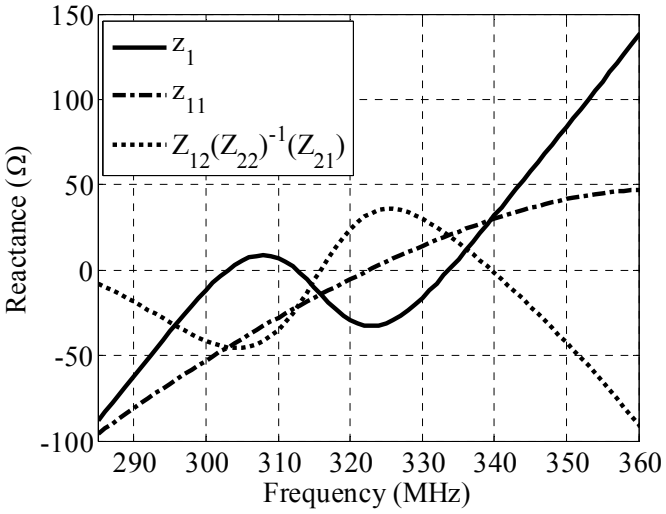

(b) Reactance

Figure 60. Resistance (a) and reactance (b) of impedance of configuration C.

The induced current magnitude and phase on the parasitic elements was calculated using (58) and (59) for configurations A and C by feeding the driven element with 1 Amps and 0°. Figure 61(a) plots the induced current magnitude. In configuration A, the current peak induced in the director and reflector is similar in magnitude with the director being slight greater than the reflector. The two peaks are 10 MHz apart. From Figure 57, the gain peaks at approximately 307 MHz and 334 MHz. At 307 MHz, the current magnitude of the director is very small and at 344 MHz, the current magnitude of the reflector is very small. In conjecture, because the magnitude is very small, the peak gain is due primarily to the reflector at 307 MHz and the director at 344 MHz as shown in Figure 57. For configuration C, the director and reflector current magnitude peaks are 15 MHz apart and the peak of the director is greater than the reflector. From Figure 57, the peak gain for configuration C occurs at 292 MHz and 344 MHz. Similarly to configuration A, the peak gain is due primarily to the reflector at 292 MHz and to the director at 344 MHz.

The phase at the parasitic elements is plotted for configurations A and C in Figure 61(b). This plot shows interesting results. The only difference between configuration A and C is the height of the reflector. The phase of the reflectors for both configurations shows similar trends with the minimum phase occurring at 330 MHz. While the directors are the same height for both configurations, the phase varies between them. The directors maximum phase for configuration A occurs at 305 MHz and 295 MHz for configuration C. Therefore, the reflector's height varies the phase induced in the director.

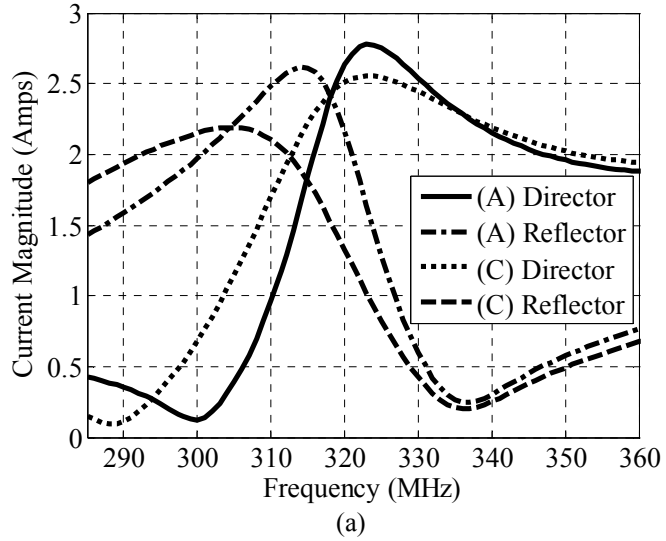

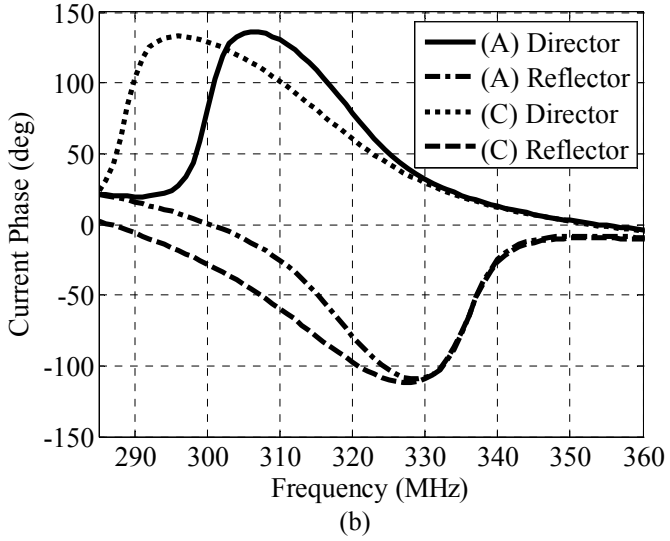

Figure 61. Induced current magnitude (a) and phase (b) on the parasitic elements.

The magnitude and phase difference between the parasitic elements is plotted in Figure 62(a) and (b) respectively. The reflector's current magnitude and phase is subtracted from the director's corresponding magnitude or phase. The current magnitude differs by approximately 2 Amps for both configurations A and C. The phase difference between the director and reflector peaks at 160°. Configuration C has a broader frequency range where the 160° phase difference is

maintained. The phase difference between the director and reflector is close to the phase difference required by two driven monopoles as derived by Brown in [7] and also demonstrated in [9]. The phase difference for two identical monopoles for 0.1λ is approximately 165°.

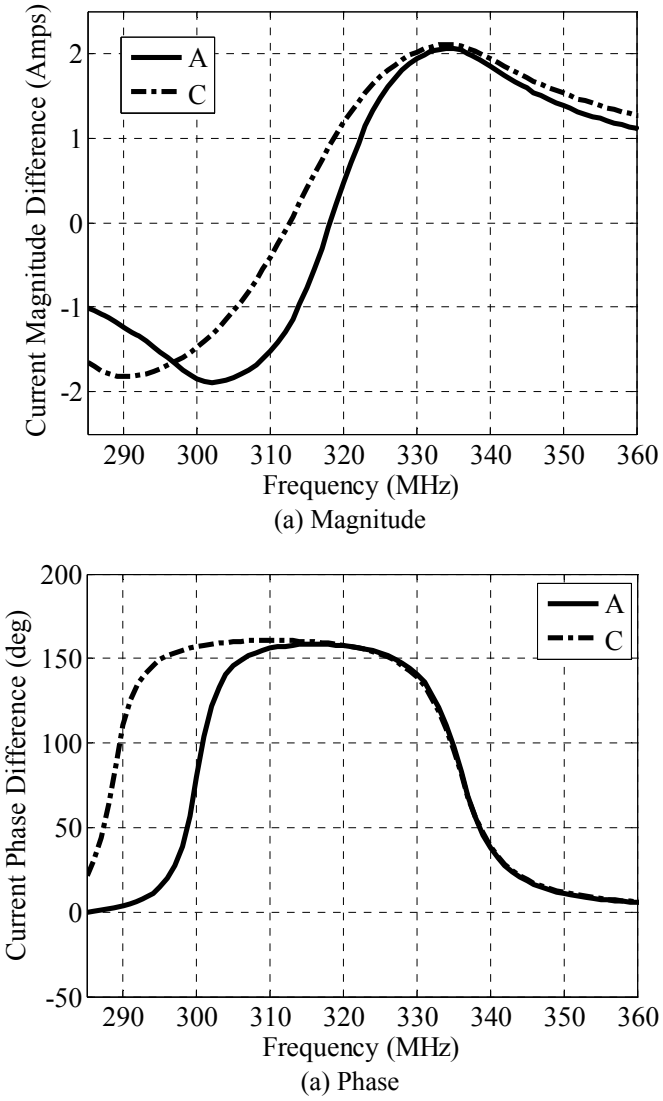

Figure 62. Current magnitude (a) and phase (b) difference between the parasitic elements.

5.3 Measured Results

Configurations A, B, and C were prototyped and measured. The antennas were fabricated using brass tubing. The input impedance of each configuration was measured on a ground plane several wavelengths large with the parasitic elements shorted. The resulting VSWR is plotted in Figure 63(a), (b), and (c) for each configuration. The 2:1 VSWR fractional bandwidth for configuration A is 9.67%, for configuration B is 11.15%, and for configuration C is 12.44%. The measured fractional bandwidth is larger than predicted by over 2.2%. The differences between measurements and calculations are due to fabrication tolerances.

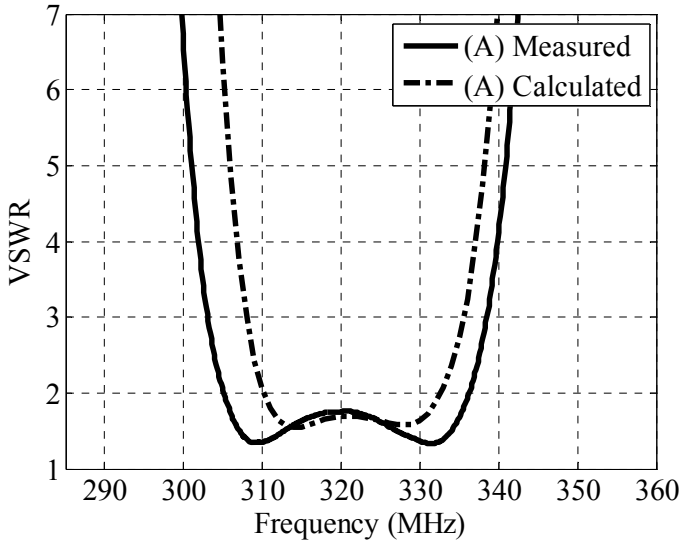

(a) VSWR of configuration A

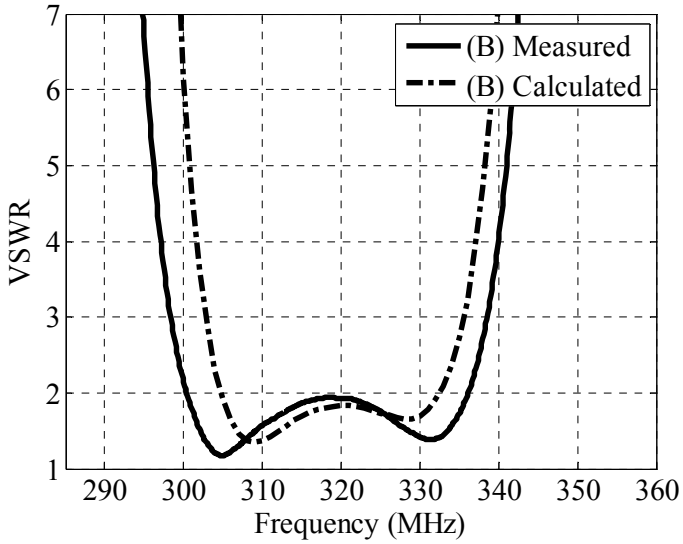

(b) VSWR of configuration B

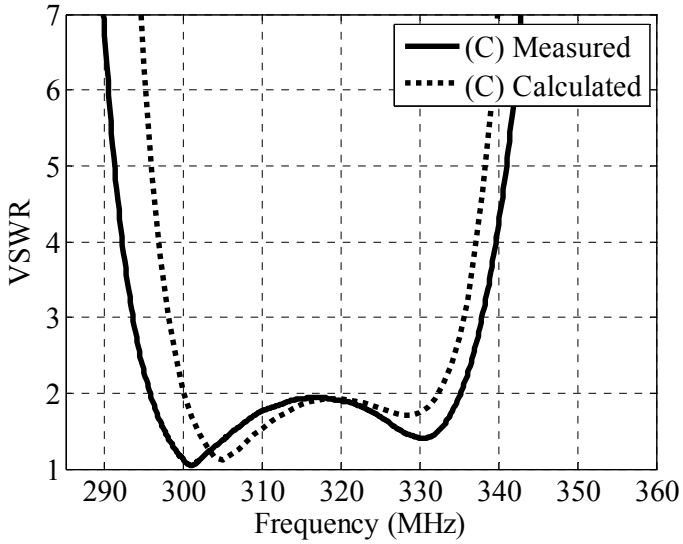

(c) VSWR of configuration C

Figure 63. Measured and calculated VSWR comparison for configuration A (a), B (b), and C (c).

The absolute gain of all three configurations was measured in an outdoor pattern range. The measurements were performed at 5° elevation. The maximum absolute gain is plotted in Figure 64 and compared against the predicted values of

Figure 59. Excellent agreement is shown between predictions and measurements. Although, the measured bandwidth of all three configurations is larger than predicted, the absolute gain bandwidth did not increase by the same amount. For an absolute gain greater than 9.4 dBi, configuration A has a 7% gain bandwidth; for a gain greater than 9 dBi, configuration B has a 9% gain bandwidth; and for a gain greater than 8.9 dBi, configuration C has 11.7% gain bandwidth. This section shows that an antenna array, with electrically small inter-element spacing can achieve directional radiation patterns and be well-matched.

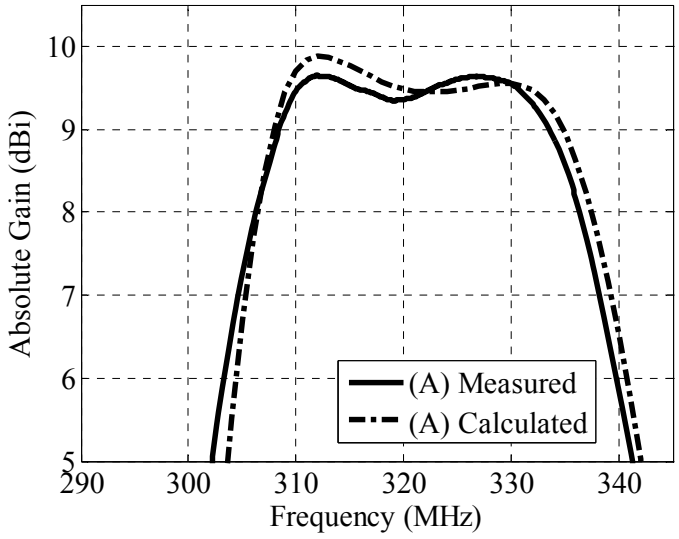

(a) Absolute gain of configuration A

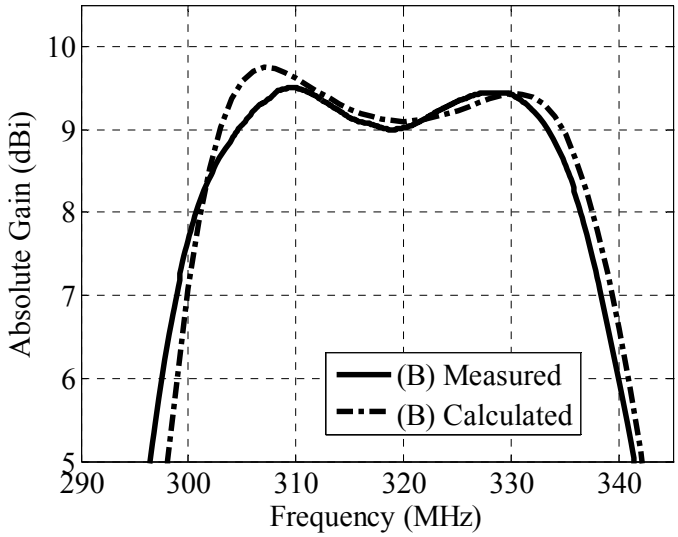

(b) Absolute gain of configuration B

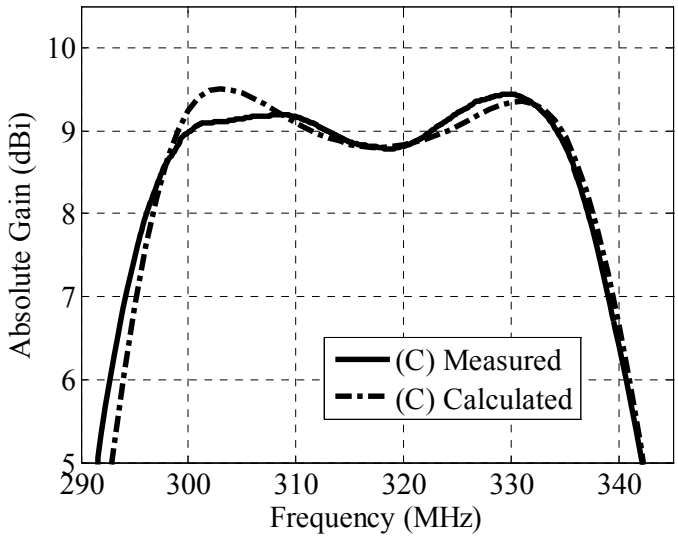

(c) Absolute gain of configuration C

Figure 64. Measured absolute gain for configuration A (a), B (b), and C (c).

5.4 Chapter Conclusion

Superdirective arrays are known to be narrowband. This chapter showed a Yagi–Uda antenna that achieved a significant improvement in bandwidth by using

both a director and reflector at an inter-element spacing of 0.053λ. By using both a director and reflector, a gain peak is noted for each element. It is also shown that by using three radiators instead of two, the effects of the mutual coupling between the elements is minimized. Multiple antenna configurations were investigated to illustrate the trade-off between bandwidth and gain. By reducing the gain by 0.7 dB, the 2:1 VSWR bandwidth of the antenna increases from 9.67% to 12.44%.

6. REACTIVELY LOADED YAGI−UDA ANTENNA

This chapter demonstrates how the design methodology developed in section 2.4 may be used to design reactively loaded antenna arrays. The methodology is demonstrated in a three-port Yagi–Uda antenna. The results of this study were published in [36]. The basic design methodology demonstrated in the chapter can be used for circular parasitic arrays by enforcing symmetry. For example, in a five-element circular array, two elements can be used as directors and two elements can be used as reflectors. This method may be applied to electronically steerable parasitic antenna radiators (ESPAR) such as to the design in [48].

6.1 Design Methodology

This section designs a symmetrical reactively loaded Yagi–Uda antenna. Because the antenna is symmetrical, the reactive loads can be used to steer the maximum gain of the antenna in two directions. Figure 65 is a network description of the antenna configuration for a driven antenna with N parasitic reactively loaded elements. The admittance of the antenna is denoted as $\mathbf{Y}$, and the admittance matrix of the parasitic load is a diagonal matrix denoted as $\mathbf{Y}_{\mathrm{L}}$. The relationship between the admittance matrix and the voltage and currents at each input port is given by the block matrix (28). The input admittance is given by (30) and the voltages at the resulting voltages from the parasitic load are given by (29).

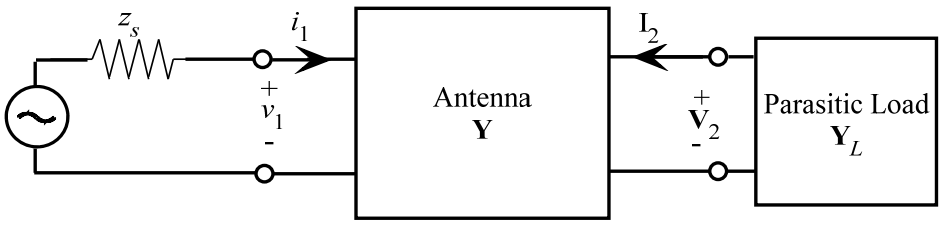

Figure 65. Parasitic loaded multiport antenna.

The reactively loaded three-element antenna designed consists of a folded monopole for the driven element and bowtie parasitic elements. The antenna configuration is similar to that in Chapter 5. The driven element is 21 cm in height, 5 cm wide, and is self-resonant at 315 MHz. The inter-element spacing between the driven element and the bowties is 5 cm, and the bowtie antennas are both 20 cm in height and 6 cm wide. The bowtie antennas are self-resonant at 298 MHz. The coordinate system of the antenna is shown in Figure 55 and the antenna's maximum gain is optimized for $\theta = 90°$ and $\phi = 0°$. By symmetry the optimized reactive loads can be interchanged to maximize the gain at $\phi = 180°$. The coordinate system shown in Figure 55 is maintained for the antenna configuration investigated in this section.

To compute the optimal load matrix, the problem is formulated as a multi-objective optimization problem with two objective functions, $\gamma(\mathbf{x})$: VSWR and gain as described in section 2.4. The objective functions and constraints are

$$\begin{aligned} &\text{minimize } \gamma(\mathbf{x}) = \begin{bmatrix} \gamma_1(\mathbf{x}) \\ \gamma_2(\mathbf{x}) \end{bmatrix} = \begin{bmatrix} \text{VSWR}_{\max}(\mathbf{x}) \\ -G_{\max}(\mathbf{x}) \end{bmatrix} \\ &\text{subject to } \mathbf{x} = \begin{bmatrix} C_1 \\ C_2 \end{bmatrix}; \ \begin{matrix} 0.1 \le C_1 \le 100 \ (\text{pF}) \\ 0.1 \le C_2 \le 100 \ (\text{pF}) \end{matrix}. \end{aligned} \tag{60}$$

The performance image is calculated by parameterizing the vector **x**, with a specific number of points rather than using the GAM. Because the capacitors are constrained to reasonable impedance values, a small number of points are used for each vector. For example, 50 points allows for a 2pF variation between each parameterized value. With such as small vector space, computing the performance image is computationally efficient. Also, the number of points and constraints can be readily modified.

6.2 Yagi–Uda Antenna Design

The electric field of each antenna element and the admittance matrix was calculated in Expert MININEC. In monopoles, the capacitance is known to reduce the electrical length while inductance increases the electrical length of the antenna. For this particular problem, the parasitic elements are loaded with capacitance. Capacitors were used to facilitate the fabrication process and minimize losses. The capacitors are connected to a 55 mm transmission line to account for the connector and circuit board. To account for the transmission line, the input impedance was calculated by [36]:

$$z_{in} = z_0 \frac{z_L + jz_0 \tan \beta l}{z_0 + jz_L \tan \beta l}, \tag{61}$$

where β is the wave number, l is the transmission line length, z_L is the reactive load impedance $(j\omega C)^{-1}$, and z_0 is the transmission line impedance (50 ohms).

Figure 66 plots the performance image of the capacitive loaded Yagi–Uda antenna for the frequency range 300–310 MHz. Each dot corresponds to a sample

of the parameterized **x** (C_1 and C_2 combination). The squares correspond to the minimal elements of the set of dots, $\mathbf{x}_p \in \mathbf{X}$. The squares approximate the Pareto front. For this bandwidth configuration, a maximum gain of 9.7 dBi is possible for a VSWR less than 2. The performance image of the Yagi–Uda antenna is plotted in Figure 67 with the gain objective function gain changed to absolute gain. For the absolute gain objective function and the same set, $\mathbf{x} \in \mathbf{X}$, the number of Pareto points decreases. Due to the impedance mismatch, the maximum absolute gain possible is 9.2 dBi with a VSWR of 2.2. Figure 66 gives insight into the maximum possible gain achievable by the antenna design while Figure 67 gives insight into the maximum absolute gain possible due to the impedance mismatch.

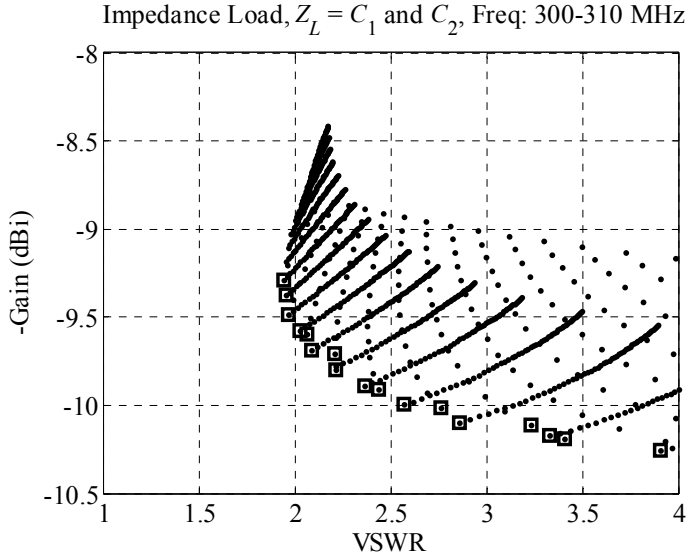

Figure 66. Gain performance image of capacitive loaded Yagi–Uda.

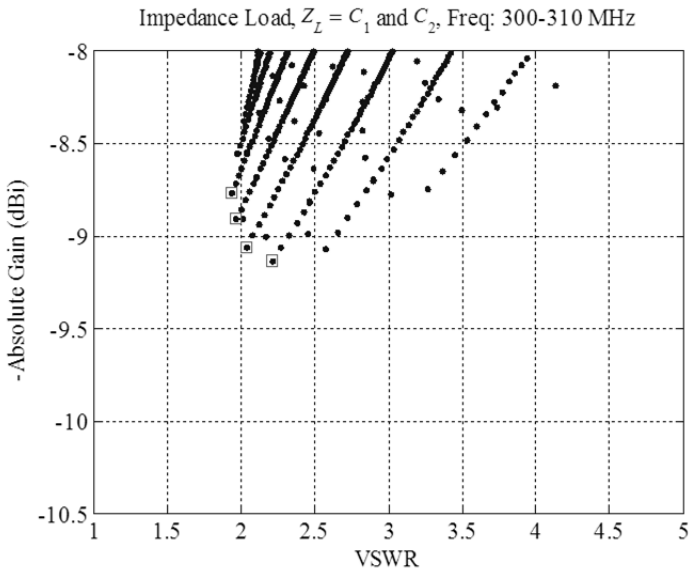

Figure 67. Absolute gain performance image of capacitive loaded Yagi–Uda.

Next, an investigation into the antenna performance, as the bandwidth is increased, is explored. The estimated Pareto front is calculated for bandwidths of 3.3% (300–310MHz), 6.5% (300–320MHz), 9.5% (300–330MHz), and 12.5% (300–340MHz). Figure 68 plots the estimated Pareto front from the performance image for each bandwidth configuration, with the performance image more heavily sampled over the results shown in Figure 66. As expected, the gain decreases with increased bandwidth.

Figure 69 plots the Pareto front where the objective function is modified from gain to absolute gain. The absolute gain at 3.3% is 9.2 dBi for a VSWR of 2. There are Pareto optimal points for the 6.5%, 9.5%, and 12.5% bandwidth that produce about the same trade-off between VSWR and gain or absolute gain were the absolute gain is 8.6 dBi and VSWR is 2.5.

Because the impedance mismatch negates the gain of the antenna an investigation into impedance matching to improve the VSWR and absolute gain was also performed. To investigate the improvement in the antenna performance with impedance matching, every Pareto optimal point with gain greater than 7 dBi and VSWR less than 5 was impedance matched with three components. The inductor and capacitor values are bounded by

$$0.1 \le L \le 500 \text{ (nH)}$$
$$0.1 \le C \le 500 \text{ (pF)}$$

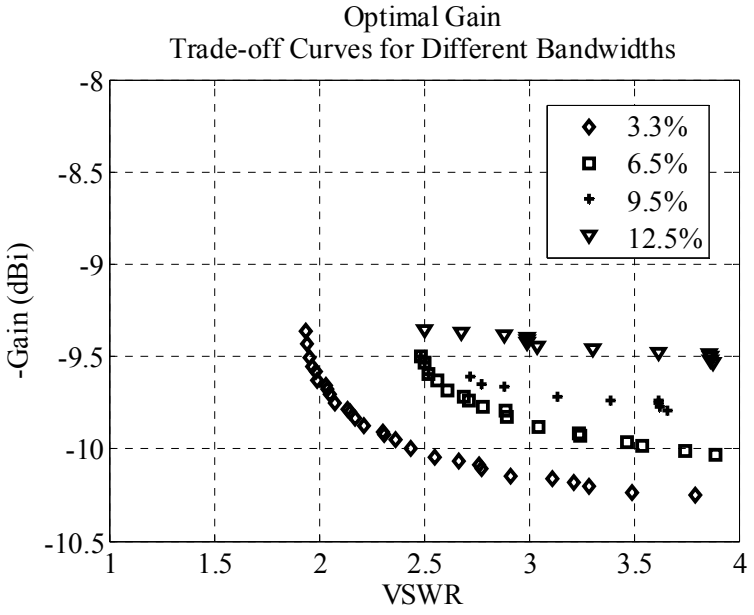

Figure 68. Maximum gain minimal elements for various bandwidths.

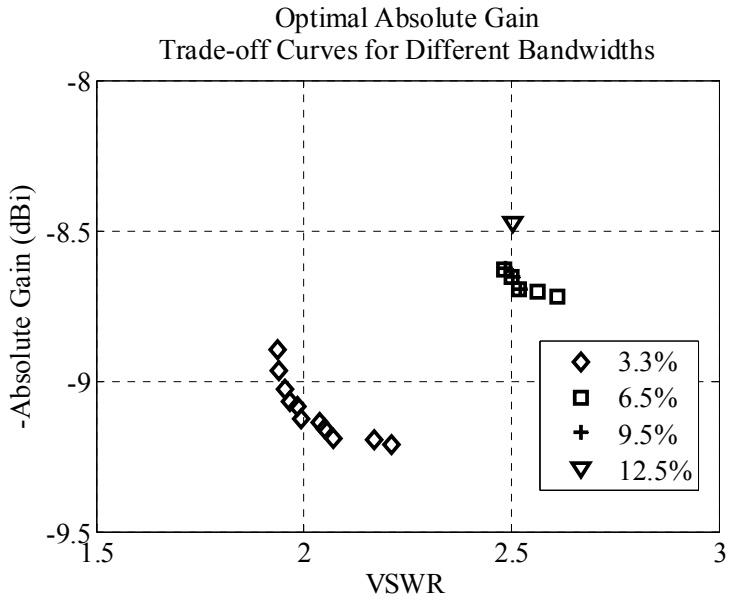

Figure 69. Maximum absolute gain minimal elements for various bandwidths.

The impedance matching results are plotted in Figure 70. In comparing the results shown in Figure 69 and the results in Figure 70, the absolute gain with impedance matching improves from 9.2 to 10 dBi. Two pairs of reactive loads were selected for the measurements. The first is for the 3.3% configuration, version 1, and the second is for the 9.5% configuration, version 2. These two configurations were selected to verify the trade-off between gain and bandwidth. For version 1, the capacitor values required were 21 pF and 8.2 pF. The reflection coefficient for version 1 with and without impedance matching is plotted in Figure 71, and the gain improvement is shown in Figure 72. A three-component matching network is used to match the antenna. The antenna design shows a gain of 10 dBi and VSWR less than 2. Version 2 consists of a capacitor of 27 pF and 3.9 pF. The reflection coefficient, with and without impedance matching, is shown in Figure 73, and the gain improvement is displayed in Figure 74. By impedance

matching, the antenna has a gain of 9 dBi and VSWR of 2. The antenna configuration and performance results are tabulated in Table 3.

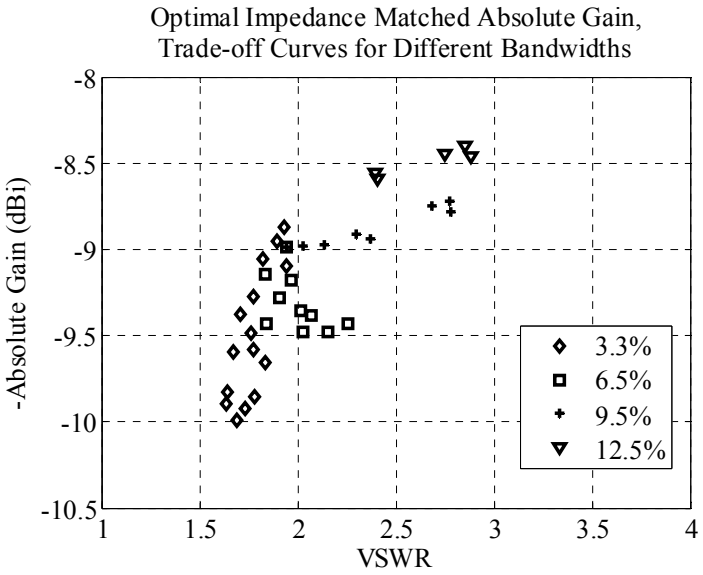

Figure 70. Impedance matched Pareto front for various bandwidths (absolute gain).

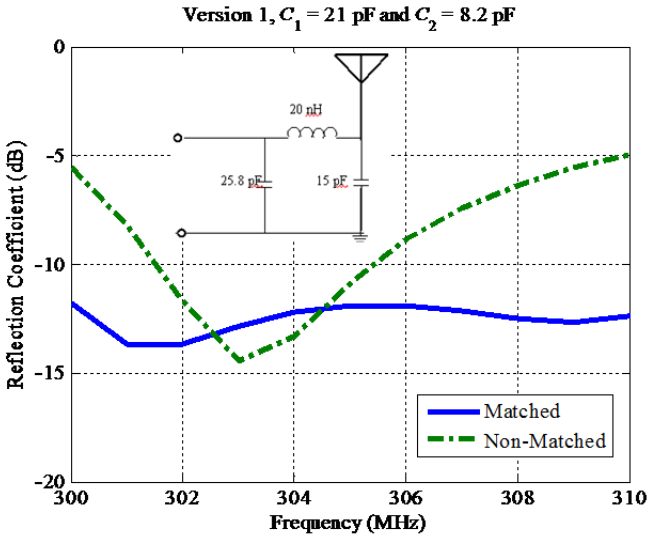

Figure 71. Reflection coefficient of impedance matched reactively loaded (300–310 MHz).

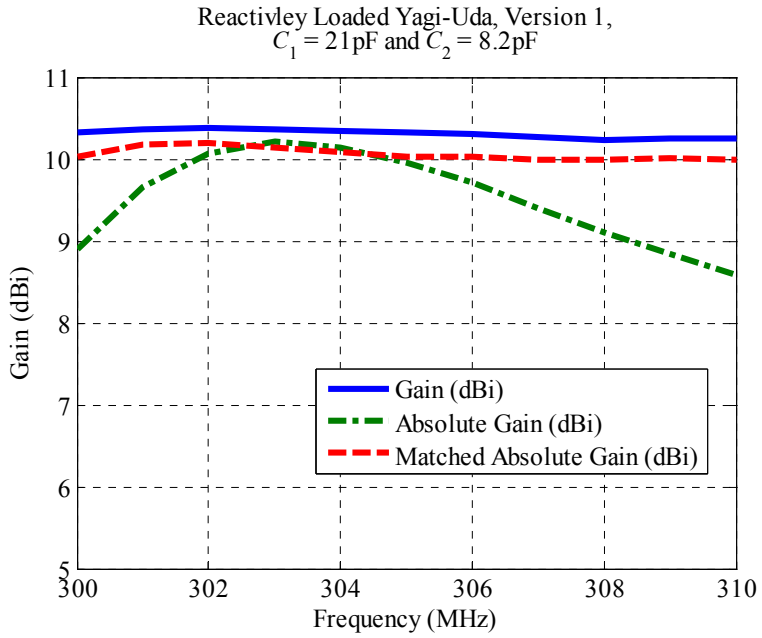

Figure 72. Gain of impedance matched reactively loaded (300–310MHz).

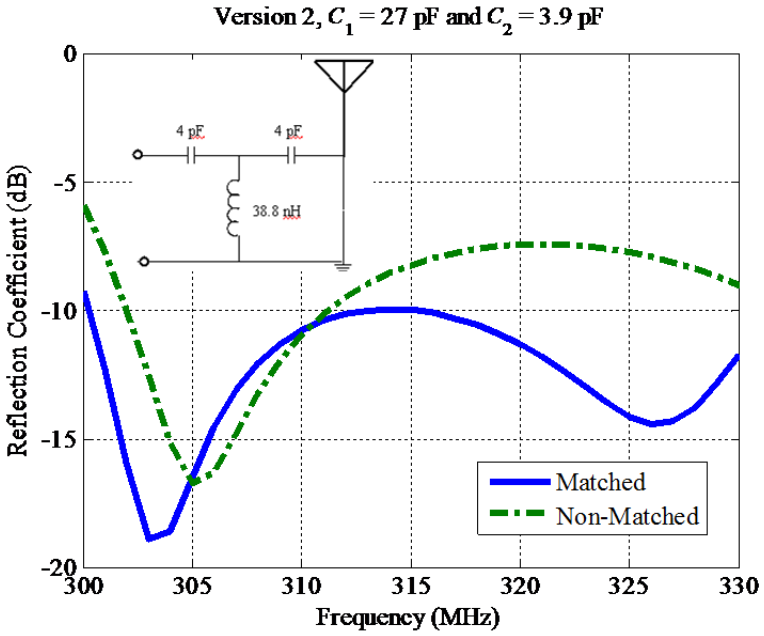

Figure 73. Reflection coefficient of impedance matched reactively loaded (300–330MHz).

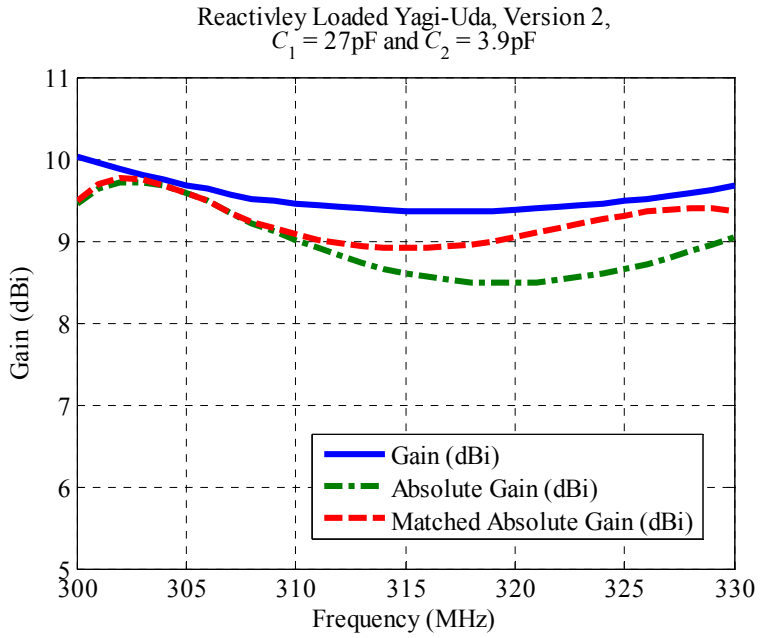

Figure 74. Gain of impedance matched reactively loaded (300–330MHz).

Table 3. Impedance Matching Configurations Investigated and Results.

	Version 1	**Version 2**
Optimized Bandwidth	3.3% (300–310 MHz)	9.5% (300–330 MHz)
Reactive Load	21 pF and 8.2 pF	27 pF and 3.9 pF
Original VSWR	≈ 3.6	≈ 3
Original Absolute Gain	8.6 dBi	8.5 dBi
Matched VSWR	< 2	≈ 2
Matched Absolute Gain	10 dBi	8.9 dBi

6.3 Measured Results

The reactively loaded Yagi–Uda antenna was fabricated and measured. Figure 75 is a photograph of the fabricated Yagi–Uda. Impedance matching networks were designed and built based on the measured impedance. To connect the impedance matching network to the antenna, the additional transmission line from the connector to the network was included in the design. ANSOFT Designer was used to design the impedance matching networks and layout of the PCB. A photo of the impedance matching networks and topology is shown in Figure 76. The impedance matching networks consists of a two-component ladder. Version 1 was matched with a series inductor of 27 nH and shunt capacitor of 6.8 pF while version 2 was matched with a shunt capacitor of 2.2 pF and series inductor of 16 nH. The measured VSWR of the antenna, with and without a matching network, is shown in Figure 77. By impedance matching, the VSWR 2:1 impedance match for version 1 is 4.2% and 9.5% for Version 2.

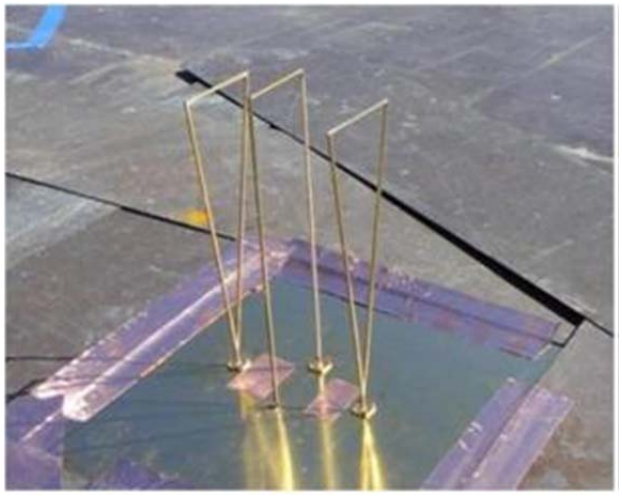

Figure 75. Reactively loaded Yagi–Uda antenna.

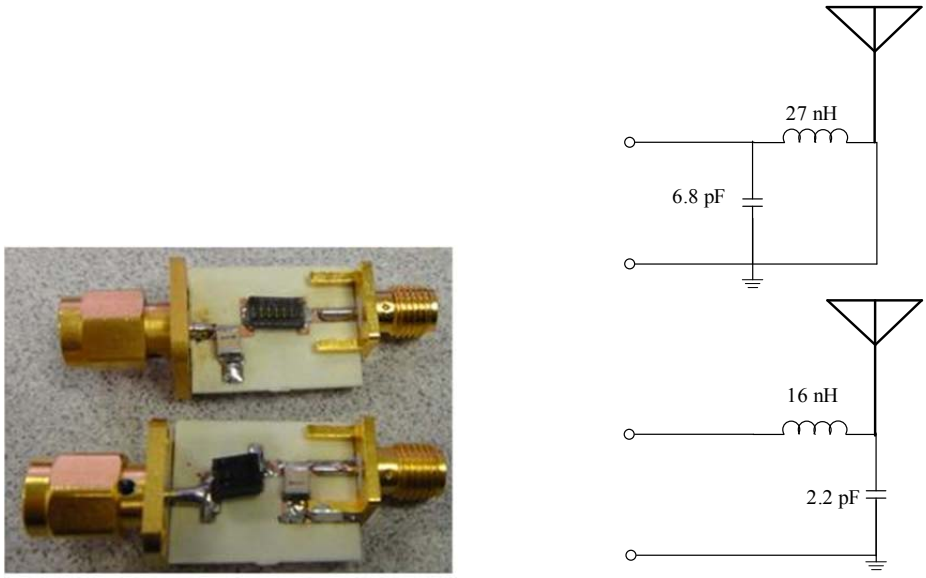

Figure 76. Impedance matching networks for reactively loaded Yagi–Uda.

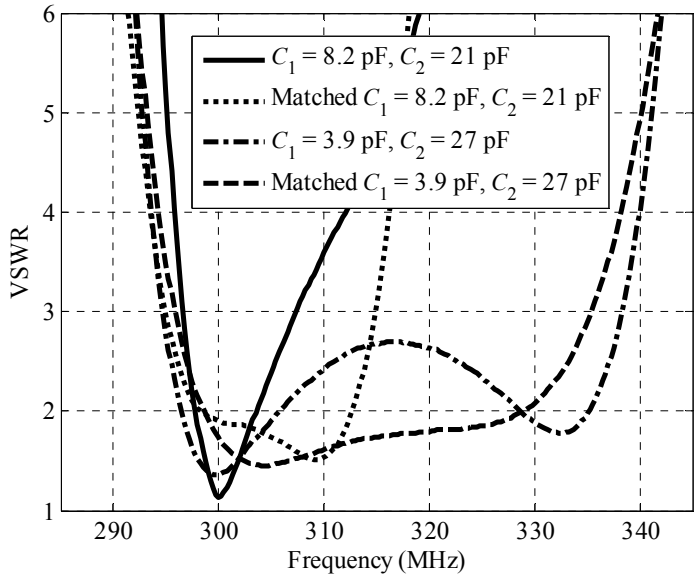

Figure 77. Measured VSWR for the reactively loaded Yagi–Uda.

Figure 78 displays the measured absolute gain of each configuration with and without impedance matching. The measured gain shows Version 1 attained slightly higher gain than the Version 2 configuration. The gain for Version 1 is

greater than 9 dBi and for Version 2 the gain is greater than 8.8 dBi. While the antenna design presented in chapter 5 gives similar performance without requiring impedance matching networks and reactive loads this antenna design is capable of scanning its main beam by 180° with the inclusion of switches. The beam scanning is possible because the antenna is symmetrical.

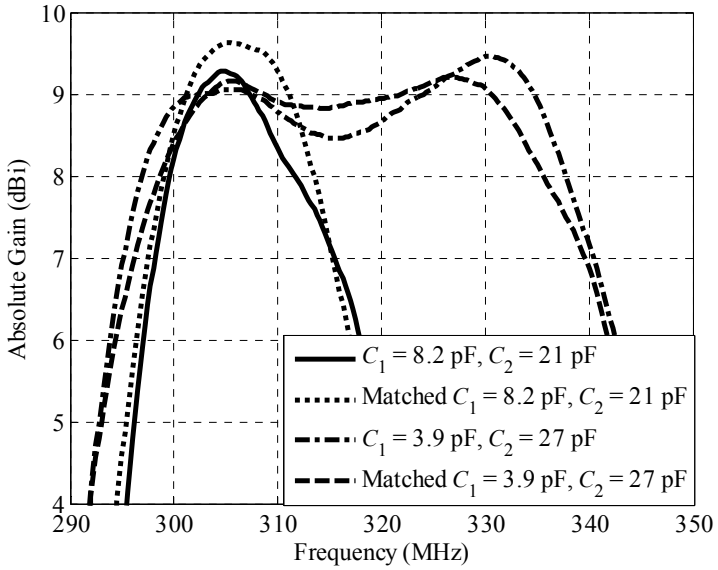

Figure 78. Measured gain of reactively loaded Yagi–Uda.

To demonstrate how the antenna is capable of scanning its main beam, the reactive loads of version 2 were manually interchanged between each parasitic element. A different impedance matching network was used during these measurements because the antenna was reassembled and care was taken to maintain equal spacing between the antenna element. The impedance matching networks consists of a two-component ladder, a shunt capacitor of 0.4 pF and a series inductor of 13.5 nH. The measured VSWR of the antenna, with and without the matching network, is shown in Figure 79. Each configuration is referred to as

Beam 1 and *Beam 2*. With the impedance matching network, the VSWR 2:1 was reduced from approximately 2.5 to 2. Each beam configuration is similar to each other due to the symmetry of the antenna design. The main differences are due to the fabrication and assembly of the antenna.

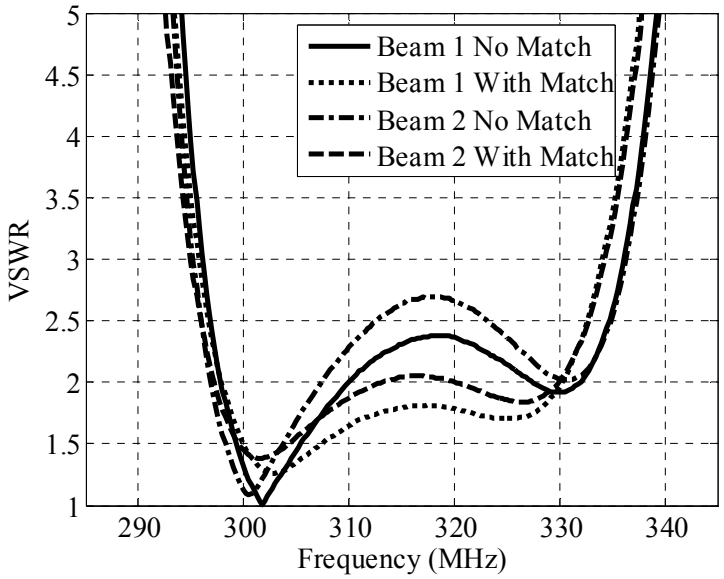

Figure 79. VSWR of reactively loaded Yagi–Uda for version 2 showing the symmetry between Beam 1 and Beam 2.

The absolute gain of the antenna was measured for both beams. Figure 29 plots the measured absolute gain of each beam configuration with and without impedance matching. As expected, impedance matching improves the absolute gain performance. The predicted absolute gain of 9 dBi was very similar to the measured gain. Also, each beam produces similar gain performance. With the inclusion of switches, the antenna could switch its direction of maximum gain by 180° by switching to the appropriate reactive load. The effects of the switch losses would need to be investigated.

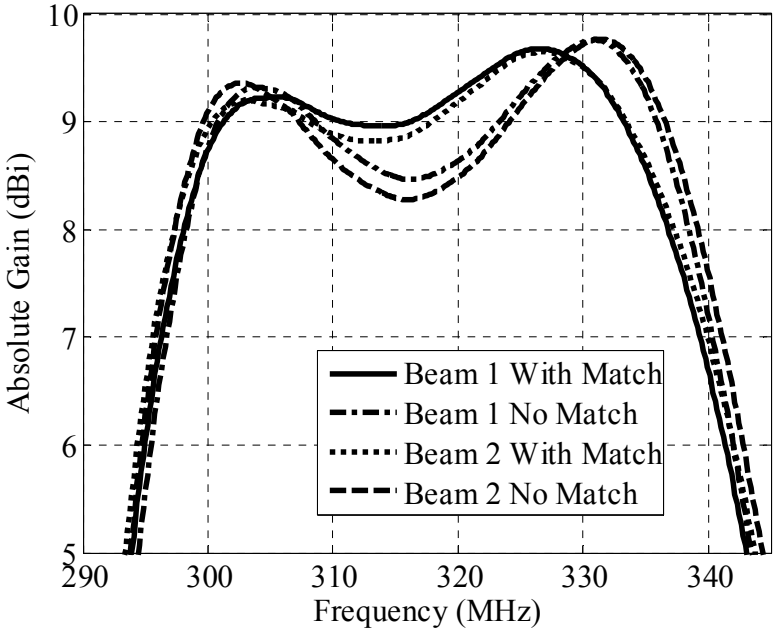

Figure 80. Absolute gain measurements of reactively loaded Yagi–Uda for version 2 showing the symmetry between Beam 1 and Beam 2.

6.4 Chapter Conclusions

The design methodology presented in section 2.3 was used to design a reactively loaded Yagi–Uda antenna with the capability of scanning its main beam in two directions. The design methodology can be used for other antenna configurations that require impedance loading optimization. The antenna designed using the methodology achieved a high absolute gain of 8.8 dBi and a 9.5% bandwidth for a VSWR less than 2 with an inter-element spacing of 0.053λ.

7. SUMMARY AND RECOMMENDATIONS

7.1 Summary

This dissertation addresses the topics of impedance matching and radiation pattern optimization as applied to superdirective antenna arrays. The primary optimization goal was to minimize the input VSWR of the antenna array while maximizing the gain for a frequency range. This illustrated the trade-offs between input VSWR, bandwidth, and gain for three antenna designs. It was shown that by trading-off a small amount of gain, the bandwidth of the antenna array was significantly increased while maintaining a low VSWR.

To optimize the input VSWR and radiation pattern of the antenna array, multi-objective optimization was used along with superposition. The superposition method allowed for the gain of an antenna array to be calculated for any load configuration by exporting the admittance matrix of the array and the short-circuit electric fields. The design methodology was detailed in Chapter 2.4.

In Chapter 3, a new type of an antenna array feed network was introduced using multiport impedance matching for a two-port antenna with an inter-element spacing of 0.1λ. It was shown that to achieve high gain and low VSWR, the antenna design is critical. Chapter 4 demonstrated that with a proper antenna design, the multiport impedance matching network and antenna configuration are capable of increasing the bandwidth and achieved a high directionality. The antenna showed an increase in bandwidth from 1.7% to 5.8% and a measured absolute gain of 8.9 dBi. Each antenna element required to be folded three times

to increase the self-impedance of the antenna. However, it was also shown that while the impedance matching network is realizable, it was also sensitive to the component footprints and tolerances.

In Chapter 5, a three-port Yagi–Uda antenna was designed with an inter-element of ~0.05λ. This antenna design made a significant contribution to the design of superdirective antennas by showing that by using three antenna elements rather than two, the effects of mutual coupling are minimized and only the driven antenna element required to be folded one time to increase the self-impedance. Four antenna configuration were investigated to show the trade-offs between gain and bandwidth. It was shown that by decreasing the gain by 0.7 dB, the gain bandwidth of the antenna increased from 7% to 11.7% and the VSWR bandwidth increased from 9.67% to 12.44%. Chapter 6 implements the design methodology in a reactively loaded Yagi–Uda with an inter-element spacing of ~0.05λ/ that achieved a 9.5% bandwidth. Although the non-loaded design has better bandwidth and gain performance, the reactively loaded Yagi–Uda antenna is capable of beam scanning. By including switches and inter-changing the reactive loads, the antenna can scan the maximum direction of radiation by 180°.

7.2 Recommendations for Future Work

Recommendations for future work include modifying the network synthesis algorithm with sophisticated component models to reduce the network sensitivity and allow for the inclusion of loss in the optimization. This

modification can be accomplished by including small signal models of inductors and capacitors.

It is also recommended to design a multiport impedance matching feed configuration for the three-port Yagi–Uda antenna. Because the three-port Yagi–Uda antenna has more design degrees of freedom than a two-port, especially with mutual coupling, the multiport impedance matching network feed configuration might be capable of further increasing the bandwidth of the antenna design. The network synthesis algorithm would need to be extended to include three ports.

The three-port Yagi-Uda was designed with a folded driven element and bow-tie parasitic elements. Further investigation is needed to determine if other radiators with larger inherent bandwidth can extend the bandwidth of the Yagi-Uda. Also, a study on how the inter-element spacing can be further reduced is needed to determine if the footprint of the antenna arrays can be further reduced.

The reactively loaded Yagi-Uda antenna was shown to be capable of beam scanning. A method to switch the reactive loads needs to be investigated to minimize losses. The array configuration can also be extended to circular arrays.

Lastly, the work in this dissertation focused on superdirective antenna arrays, the design methodology is general and can be applied to other antenna configurations, such as the half-loop in Figure 1, to optimize input VSWR, bandwidth, and radiation pattern.

REFERENCES

[1] C. A. Balanis, *Antenna Theory Analysis and Design*, 3rd Edition, Wiley-Interscience, Hoboken, New Jersey, 2005.

[2] R. P. Haviland, "Supergain antennas: possibilities and problems," *IEEE Antennas and Propagation Magazine*., vol. 37, pp. 13–26, Aug. 1995.

[3] A. Bloch, R. G. Medhurst, and S.D. Pool, "A new approach to the design of super-directive aerial arrays," in *Proc. Inst. Elec. Eng*., Sep. 1953, pp 303–314.

[4] R. C. Hansen, *Electrically Small, Superdirective, and Superconducting Antennas*, New Jersey: Willey, 2006.

[5] J. D. Kraus, "Antenna arrays with closely spaced elements," *Proceedings of the IRE* , vol.28, no.2, pp. 76–84, Feb. 1940.

[6] J. D. Kraus and R. J. Marhefka, *Antennas for All Applications*, 3rd ed. New York: McGraw-Hill, 2002.

[7] G. H. Brown, "Directional antennas," *Proceedings of the IRE,* Vol. 25, pp. 78–145, 1937.

[8] A. I. Uzkov, "An approach to the problem of optimum directive antennae design," *Comptes Rendus de l'Academie des Sciences de l'*URSS, vol. 53, pp. 35–38, 1946.

[9] E. E. Altshuler, T. H. O'Donnell, A. D. Yaghjian, and S. R. Best, "A monopole superdirective array," *IEEE Transactions on Antennas and Propagation*, vol. 53, no. 8, Aug. 2005, pp. 2653–2661.

[10] S. Lim and H. Ling, "Design of a planar, closely spaced yagi antenna," *IEEE APS Symposium*, Honolulu, HI, June 2007, pp. 5997–6000.

[11] S. Lim and H. Ling, "Design of a closely spaced, folded yagi Antenna," *IEEE Trans. Antennas and Wireless Propagation Letters*, vol. 5, 2006, pp. 302–305.

[12] J. Yu and S. Lim, "A multi-band, closely spaced yagi antenna with helical-shaped directors," *IEEE APS Symposium*, Charleston, SC, June 2009.

[13] S. R. Best, E. E. Altshuler, A. D. Yaghjian, J. M. McGinthy, and T. H. O'Donnell, "An impedance-matched 2-element superdirective array,"

IEEE Trans. Antennas and Wireless Propagation Letters, vol. 7. 2008, pp. 302–305.

[14] S. Lim, "Design of a multidirectional, high-gain compact yagi antenna," *Antennas and Wireless Propagation Letters*, *IEEE*, vol. 8, pp. 418–420, 2009.

[15] T. H. O'Donnell, and A. D. Yaghjian, "Electrically small superdirective arrays using parasitic elements," *IEEE APS Symposium*, Albuquerque, NM, July 2006.

[16] R. M. Fano, "Theoretical limitations of broadband matching of Arbitrary Impedances," *J Franklin Institute*, vol. 249, pp. 139–154, 1959.

[17] J. C. Allen, *H^{∞} Engineering and Amplifier Optimization*, Boston: Birkhauser, 2004.

[18] J. C. Allen, J. Rockway, and D. Arceo, "Wideband multiport matching phase I: single-feed multiport antennas," SSC San Diego, TR 1972, September 2008.

[19] J. Weber, C. Volmer, K. Blau, R. Stephan, M. A. Hein, "Miniaturized antenna arrays with an element separation down to λ/10," *IEEE Antennas and Propagation Society International Symp.*, 2007, pp. 5897-5900.

[20] J. Weber, C. Volmer, K. Blau, R. Stephan, and M. A. Hein, "Miniaturized antenna arrays using decoupling networks with realistic elements," *IEEE Transaction on Microwave Theory and Techniques*, vol. 54, no. 6, 2006.

[21] J. C. Coetzee, and Y. Yu, "Port decoupling for small arrays by means of an eigenmode feed network," *IEEE Transactions on Antennas and Propagation*, vol. 56, no. 6, 2008.

[22] T. Lee and Y. E. Wang, "Mode-based beamforming with closely spaced antennas," *IEEE/MTT-S International Microwave Symp.,* 2007, pp. 1723–1726.

[23] H. Yagi, "Beam transmission of ultra short waves," *Proceedinsg of the IRE*, vol. 16, pp. 715–741, June 1928.

[24] H. W. Ehrenspeck and H. Poehler, "A new method for obtaining maximum gain from Yagi antennas," *IRE Trans. Antennas and Propagation*, vol. AP-7, pp. 379−386, Oct. 1959.

[25] D. K. Cheng and C. A. Chen, “Optimum element spacing for Yagi–Uda arrays,” *IEEE Trans. Antennas Propagat*., vol. AP-21, pp. 615–623, Sept. 1973.

[26] C. A. Chen and D. K. Cheng, “Optimum element lenghts for Yagi–Uda arrays,” *IEEE Trans. Antennas Propagat*., vol. AP-23, pp. 8−15, Jan. 1975.

[27] N. V. Venkatarayalu and T. Ray, “Single and multi-objective design of Yagi–Uda antennas using computational intelligence,” *The 2003 Congress on Evolutionary Computation*, vol. 2, pp. 1237−1242, Dec. 2003

[28] Y. Kuwahara, “Multipobjective Optimization Design of Yagi–Uda Antenna,” *IEEE Trans. Antennas and Propagation*, vol. 53, no. 6 June 2008.

[29] M. Khodier and M. Al-Aqil, "Design and optimisation of Yagi–Uda antenna arrays," *Microwaves, Antennas & Propagation, IET* , vol.4, no.4, pp.426-436, April 2010.

[30] U. Singh, M. Rattan, and N. Singh, “Optimization of gain and impedance of Yagi–Uda antenna using simulated annealing,” *Inter. Conf. Applied Electromagnetics and Communications*, pp. 1–4, Sept. 2007.

[31] B. Yuan and X. Want, “Multi-objective optimization of double-folded Yagi antenna using genetic algorithms,” *Inter. Conf. Computational Intelligence and Software Engineering*, pp. 1–4, Dec. 2010.

[32] G. A. Thiele, “Analysis of Yagi–Uda-Type Antennas,” *IEEE Trans. Antennas and Propagation*, vol. AP-17, pp. 24−31, Jan. 1969.

[33] D. Arceo and C. A. Balanis, “A multiport impedance matching feed network for directional antennas,” *IEEE Antennas and Wireless Propagation Letters*, submitted for publication.

[34] D. Arceo and C. A. Balanis, “A compact Yagi–Uda antenna with enhanced bandwidth,” *IEEE Antennas and Wireless Propagation Letters*, Vol. 10, pp. 442–445, 2011.

[35] B. K. Lau, and J. B. Andersen, “Simple and efficient decoupling of compact arrays with parasitic scatterers,” *IEEE Transaction on Antennas and Propagation*, vol. 60, no. 2, Feb. 2012.

[36] D. Arceo and C. A. Balanis, “Design methodology for a reactively loaded Yagi–Uda antenna,” *IEEE Antennas and Wireless Propagation Letters*, vol. 11, pp. 795–798, 2012.

[37] G. Gonzalez, *Microwave Transistor Amplifiers*, Second Edition, Prentice Hall, Upper Saddle River, NJ, 1997.

[38] J. C. Allen and D. Arceo, “A Pareto approach to lossy matching,” SSC San Diego, TR 1942, September 2006.

[39] J. R. Mautz and R. F. Harrington, “Modal analysis of loaded *N*-port scatterers,” *IEEE Trans. Antennas Propagat.,* vol. AP-21, no. 2, pp. 188–199, Mar. 1973.

[40] R. F. Harrington, “Reactively controlled directive Arrays,” *IEEE Trans. on Antennas and Propagation,* vol. AP-26, no. 3, pp. 390–395 May 1978.

[41] S. Rao, *Engineering Optimization Theory and Practice*, 4th ed. New Jersey: John Wiley & Sons, 2009.

[42] G. Eichfelder, *Adaptive Scalarization Methods in Multiobjective Optimization* (Vector Optimization series), Berlin, Germany: Springer-Verlag, 2008.

[43] S. Boyd, and L. Vandenberghe, *Convex Optimization*, Cambridge, U.K., Cambridge University Press, 2009.

[44] I. Y. Kim and O. L. de Weck, “Adaptive weighted-sum method for bi-objective optimization: Pareto front generation,” *Struct. Multidiscip. Optim.*, vol. 29, no. 2, pp. 149–158, 2005.

[45] C. Fonseca and P. J. Fleming, “An Overview of Evolutionary Algorithms in Multiobjective Optimization,” *Evolutionary Computation*, vol. 3, issue 1, pp. 1–16, 1995.

[46] F. W. Gembicki, “Performance and sensitivity optimization: a vector index approach,” Ph.D. Dissertation, Dept. Systems Eng., Case Western Reserve Univ., Cleveland, OH, 1974.

[47] MATLAB version R2011b, Natick, Massachusetts: The MathWorks Inc., 2011.

[48] K. Iigusa, K. Sato, M. Fujise, "A slim electronically steerable parasitic Array Radiator Antenna," *ITS Telecommunications Proceedings, 2006 6th International Conference on* , pp.386–389, June 2006.

[49] K. Iigus, and T. Ohira, “A simple and accurate mathematical model of electronically steerable parasitic array radiator antennas,” *Consumer Communications and Networking Conference, 2004, First IEEE*, pp. 312–315, Jan. 2004.

[50] R. J. Dinger, “Reactively steered adaptive array using microstrip patch elements at 4 GHz,” *IEEE Transactions on Antennas and Propagation,* Vol. AP-32, No. 8, pp. 848–856, Aug. 1984.

[51] A. Lopez, “Review of narrowband impedance-matching limitations,” *IEEE Antennas and Propagation Magazine*, Vol. 46, No 4, Aug. 2004, pp. 88–90.

[52] A. G. Sokolov, and L. I. Babak, “Examples of numerical solution of the Fano gain-bandwidth limitation problem for different load types,” *in Proc. 3-rd Internat. Symp. SIBCONVERS’99*, 18–20 May 1999, pp. 236–238.

[53] J. C. Allen, and D. Schwartz, “Wide-band impedance matching: H^{∞} performance bounds,” *IEEE Transactions on Circuits and Systems—II: Express Briefs*, Vol. 51, No. 51, July 2004.

[54] R. M. Wohlers, *Lumped and Distributed Passive Networks*, Academic Press Inc, New York, New York, 1969.

[55] Y. Oono, “Minimum-gyrator synthesis of *N*-ports”, *IEEE Transactions on Circuit Theory*, Vol. CT-19(4), pp. 313–316, 1972.

APPENDIX A

A. SCATTERING MATRIX DECOMPOSITION METDHOD

The theoretical impedance matching bounds were derived by Fano in 1950 [16]. Since then, Lopez [48] used Wheeler's formulations to derive a closed-form solution based on the Q-bandwidth relationship and reflection coefficient. Similarly, Hansen [4] independently derived closed-form formulas based on his Bandwidth Improvement Factor (BWIF) that converges to the Fano bound. Both of these methods are only applicable to narrowband devices. The Fano bound is calculated by representing the load impedance as a rational function or an equivalent circuit [52]. For wideband applications, Allen and Schwartz [53] developed the H^{∞} wide-band gain optimization (WGO) method and the $U^{+}(2,d)$ computation. The $U^{+}(2,d)$ is further analyzed in [17]. This section provides an examination of the $U^{+}(2,d)$ within an engineering context and is referred to as the SMD method.

The SMD method is a mathematical calculation of all possible networks as a function of lumped elements. More precisely, the SMD method is a parameterization of the scattering matrix corresponding to all lumped, passive N-ports. The SMD method can be used to bound the best possible impedance match as a function of the number of components. In practice, the number of components is limited to 4-5 to avoid losses. Two theorems by R.M. Wohlers [54] are the foundation of the SMD method.

The first theorem (Theorem 3.2, [54]) states that given a rational, linear, continuous, time-invariant, causal, passive scattering matrix $\mathbf{S}(p)$, where p denotes the complex frequency, there exist an N-port network consisting of passive, time-invariant, lumped elements. In other words, $\mathbf{S}(p)$ contains wires,

transformers, capacitors, inductors, resistors, and gyrators. A gyrator is a canonical, nonreciprocal, two-port device having a 180° phase shift . Wohlers introduces three corollaries from the first theorem. Given $\mathbf{S}(p)$ is a rational, linear, continuous, time-invariant, causal, passive matrix, then

1. Let the normal rank of $\mathbf{S}(p)$ be $r[\mathbf{S}(p)] = \text{rank}(\mathbf{U}_N - \mathbf{S}(-p)^T \mathbf{S}(p))$. Then the number of resistor in $\mathbf{S}(p)$ is greater than or equal to $r[\mathbf{S}(p)]$. Moreover, of all the N-ports that have $\mathbf{S}(p)$, there exists at least one N-port having exactly $r[\mathbf{S}(p)]$ resistors.
2. Let the K distinct poles of $\mathbf{S}(p)$ be denoted as p_k. Let $\deg(\mathbf{S}(p); p_k)$ denote the largest order to which $p = p_k$ appears in any minor of $\mathbf{S}(p)$. Define Smith-McMillan degree of $\mathbf{S}(p)$ as $d = \deg_{SM}[\mathbf{s}(p)] = \sum_{k=1}^{K} \deg(\mathbf{s}(p); p_k)$. Then the number of inductors plus the number of capacitors must be equal to or greater than the Smith-McMillan degree n. Moreover, of all the N-ports that have $\mathbf{S}(p)$, there exists at least one N-port having exactly $\deg_{SM}(\mathbf{S}(p))$.
3. The number of gyrators is given by the skew-symmetric rank of $\mathbf{S}(p)$: $g[\mathbf{S}(p)] := \frac{1}{2}\text{rank}(\mathbf{S}(p) - \mathbf{S}(p)^T)$. Moreover, of all the N-ports that have $\mathbf{S}(p)$, there exists at least one N-port having exactly $g[\mathbf{S}(p)]$ gyrators [55].

Wohlers' second theorem (Theorem 3.3, [54]) states that every rational, linear, continuous, time-invariant, causal, passive scattering matrix $\mathbf{S}(p)$ of normal rank r and degree n has the following representation as a linear fractional transformation:

$$\mathbf{S}(p) = \mathbf{S}_{a,11} + \mathbf{S}_{a,12}\,\mathbf{S}_X(p)\,(\,\mathbf{U}_{n+Nr} - \mathbf{S}_{a,22}\,\mathbf{S}_X(p)\,)^{-1}\,\mathbf{S}_{a,21}, \tag{62}$$

where $\mathbf{U}_{d+Nr}$ is the identity matrix, d is the number of reactive elements, N_r is the number of resistors, $\mathbf{S}_a$ is the augmented scattering matrix, and $\mathbf{S}_X$ is the reactive load as illustrated in Figure 81. Figure 81 shows the passive, lumped N-port is a cascade of a non-reactive multiport $\mathbf{S}_a$ terminated in a reactive load $\mathbf{S}_X$. The augmented scattering matrix $\mathbf{S}_a$ has the block form [48]:

$$\mathbf{S}_a = \begin{bmatrix} \mathbf{S}_{a,11} & \mathbf{S}_{a,12} \\ \mathbf{S}_{a,21} & \mathbf{S}_{a,22} \end{bmatrix}, \tag{63}$$

where $\mathbf{S}_{a,11}$ is $N \times N$, $\mathbf{S}_{a,12}$ is $N \times (n + N_r)$, $\mathbf{S}_{a,21}$ is $(n + N_r) \times N$, $\mathbf{S}_{a,22}$ is $(n + N_r) \times (d + N_r)$ matrix, and the matrix is a non-reactive multiport, unitary matrix of real constants.

The augmented scattering matrix $\mathbf{S}_a$ is a constant, orthogonal matrix because all the reactive elements are removed. The augmented scattering matrix contains only wires, transformers, and gyrators. If the N-port is reciprocal, $\mathbf{S}_a$ is symmetric: $\mathbf{S}_a{}^T = \mathbf{S}_a$ and contains no gyrators [54].

The augmented load matrix $\mathbf{S}_X(p)$ has the block form:

$$\mathbf{S}_X(p) = \frac{p-1}{p+1}\begin{bmatrix} \mathbf{U}_{N_L} & 0 & 0 \\ 0 & -\mathbf{U}_{N_C} & 0 \\ 0 & 0 & 0_{N_r} \end{bmatrix}, \tag{64}$$

where N_L is the number inductors, N_C is the number of capacitors, N_r is the number of resistors, and $N_L+N_C=n$. If the N-port is lossless, $N_r=0$.

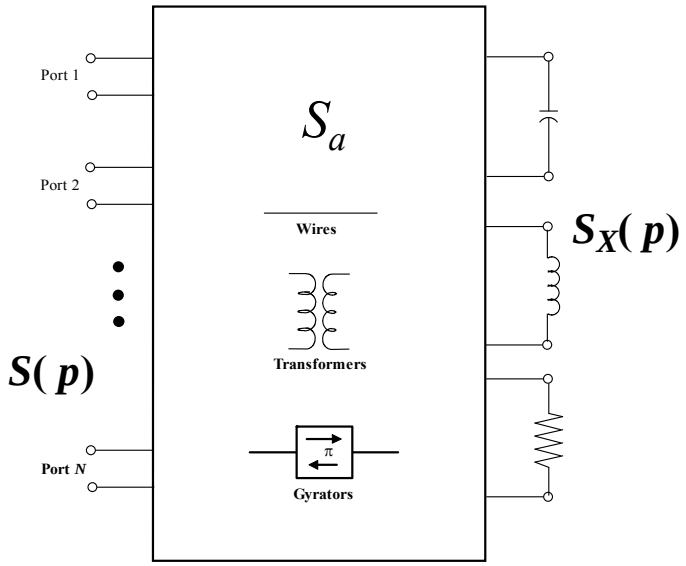

Figure 81. SMD representation of a passive, lumped, cascaded *N*-port.

The inductors and capacitors represented in (64) are normalized to unit-values. The normalization simplifies the elements because the reactive load is only a function of *p*. The reactive load is normalized because the augmented matrix includes ideal transformers. An ideal transformer terminated in a unit-value element can represent any inductor or capacitor value.

Denote the group of $M \times M$ orthogonal matrices as:

$$\mathbf{O}\,[\,M\,] = \{\, \mathbf{S}_a \in \mathrm{R}^{M\times M} : \mathbf{S}_a{}^T\, \mathbf{S}_a = \mathbf{U}_M \,\}.$$

Because $\mathbf{S}_a$ is orthogonal, sweeping over the orthogonal group $\mathbf{O}\,[N+n]$ generates all lumped, lossless, *N*-ports of degree *n*. Therefore, optimizing over all the lumped, lossless *N*-ports of degree *n* can be implemented by optimizing over the orthogonal group $\mathbf{O}\,[N+n]$. This is how the SMD method calculates all possible circuit networks as a function of lumped elements.

The *N*-port matching problem offers an example of an application of the SMD method to calculate the smallest possible VSWR over a frequency band. Using the notation of Figure 81 and Figure 10, assume the matching *N*-port is lossless with degree *n*. The scattering matrix $\mathbf{S}(p)$ of this *N*-port has the representation:

$$\mathbf{S}(p) = \mathbf{S}_{a,11} + \mathbf{S}_{a,12}\,\mathbf{S}_X(p)\,(\,\mathbf{U}_n - \mathbf{S}_{a,22}\,\mathbf{S}_X(p)\,)^{-1}\,\mathbf{S}_{a,21}, \tag{65}$$

where $\mathbf{S}_a$ is augmented scattering matrix belonging to $\mathbf{O}\,[N+n]$ and $\mathbf{S}_X(p)$ is any augmented load of the form:

$$\mathbf{S}_X(p) = \frac{p-1}{p+1}\begin{bmatrix} \mathbf{U}_{N_L} & 0 \\ 0 & -\mathbf{U}_{N_L} \end{bmatrix}. \tag{66}$$

The matching performance is measured as the largest reflection coefficient over the frequency band $\omega_{min} \le \omega \le \omega_{max}$:

$$|\Gamma_{max}| = \max\{\ |\Gamma_1(\mathbf{S}\,, \mathbf{S}_L\,;\, \omega_{min} \le \omega \le \omega_{max})|\ \}.$$

The reflection coefficient Γ_1, is given by:

$$\Gamma_1 = s_{11}(p) + \mathbf{S}_{12}(p)\big(\mathbf{U}_2 - \mathbf{S}_2(p)\mathbf{S}_L(p)\big)^{-1}\mathbf{S}_{21}(p). \tag{67}$$

The matching problem is to minimize this reflection coefficient over all augmented scattering matrices:

$$\min\{\ |\Gamma_{max}| : \mathbf{S}_a \in \mathbf{O}\ [\ N+n\ ]\ \}.$$

Sweeping over the orthogonal group to minimize the input reflection coefficient is equivalent to minimizing over all lumped, lossless *N*-ports of degree *n*. Reducing the matching problem to minimizing over the orthogonal group is an application of the SMD method.

The SMD method offers several *pros* and *cons* compared to other methods.

Pros:

- SMD method is computed as a function of reactive elements leading to more realizable matching bounds
- SMD method is general to encompass multiport devices such as an antenna with multiple feeds
- SMD method is applicable to custom frequency ranges including ultra-wideband and narrowband applications
- SMD method only needs the device impedance or reflection coefficient to compute the bound

Cons:

- SMD method relies on an optimizer to sweep over all orthogonal matrices which may not converge to a global solution
- SMD method solution accuracy is dependent on the sampling density of the device impedance
- SMD method includes gyrators that can lead to unattainable bounds. A gyrator-free computation is possible but the computation time increases.

APPENDIX B

B. FANO BOUND COMPARISON

To illustrate the SMD method, the matching bounds are calculated for the loads shown in Figure 82 [52]. The circuits include two first-order low-pass filters, one second-order low-pass filter, one high-pass filter, and one band-pass filter. The circuits are matched to the termination impedance. These circuits allow for the SMD method to be benchmarked against the Fano bound. The SMD method is dependent upon the degree of the matching circuit. The Fano bound has no degree, so it bounds all matching circuits of any degree. Consequently, the SMD bounds are always above the Fano bound in VSWR and converge to the Fano VSWR bound as the degree gets larger. For Figure 82(d), the bounds are calculated for several frequency ranges to show how the bound changes as a function of bandwidth.

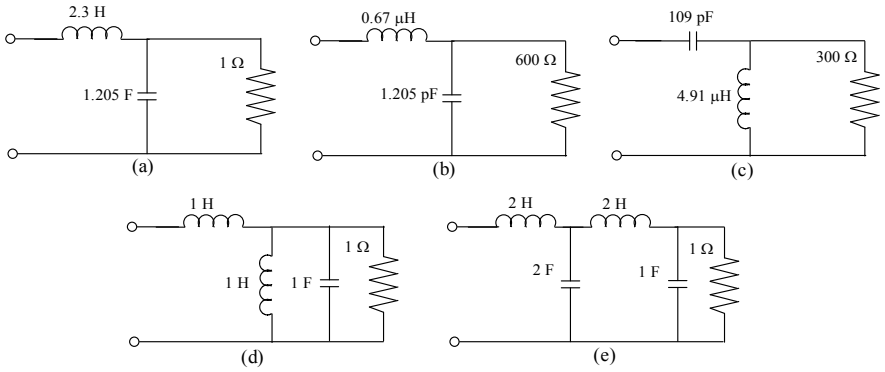

Figure 82. RLC loads.

The SMD method calculates the matching bound as a function of degree *d*. The degree *n* was swept from 0 to 15 and its results are compared to the theoretical Fano bounds given in [52]. The example number, frequency range, and results are tabulated in Table 4. The results show that as the degree increases, the SMD method converges to the Fano bound. The percentage difference between

the SMD bound at n=15 is also shown. Except for example 4(a) and 4(b), the SMD method converged to the Fano bound within 15%.

Although, a large number of reactive elements are needed to converge to the Fano bound, the SMD method shows that in most cases, only a slight improvement is gained after a few reactive elements. Figure 83 plots the VSWR calculated from the SMD bound as a function of degree. The figure shows the reduction in VSWR as the number of reactive elements is increased and how minimal improvement is gained after a few reactive elements. Example 4(a-d) shows how the reflection coefficient is minimized as the bandwidth of interest is decreased.

Table 4. SMD and Fano Matching Results.

Example No.	Fig.	Matching Frequency Band	$\lvert\Gamma_{SMD}\rvert$ (n=5)	$\lvert\Gamma_{SMD}\rvert$ (n=10)	$\lvert\Gamma_{SMD}\rvert$ (n=15)	$\lvert\Gamma_{Fano}\rvert$ [52]	%Γ
1	(a)	0–6.28 Hz	0.308	0.289	0.288	0.281	2.45
2	(b)	15–25 MHz	0.439	0.384	0.373	0.407	-8.35
3	(c)	3.4–7 MHz	0.575	0.494	0.482	0.452	6.64
4(a)	(d)	3.58–10.87 Hz	0.106	0.090	0.077	0.066	16.67
4(b)	(d)	0–2 Hz	0.282	0.194	0.178	0.155	14.84
4(c)	(d)	0.64–14.95 Hz	0.534	0.487	0.436	0.418	4.31
4(d)	(d)	2.07–18.85 Hz	0.755	0.732	0.705	0.682	3.39
5	(e)	0–6.28 Hz	0.433	0.401	0.398	0.387	2.84

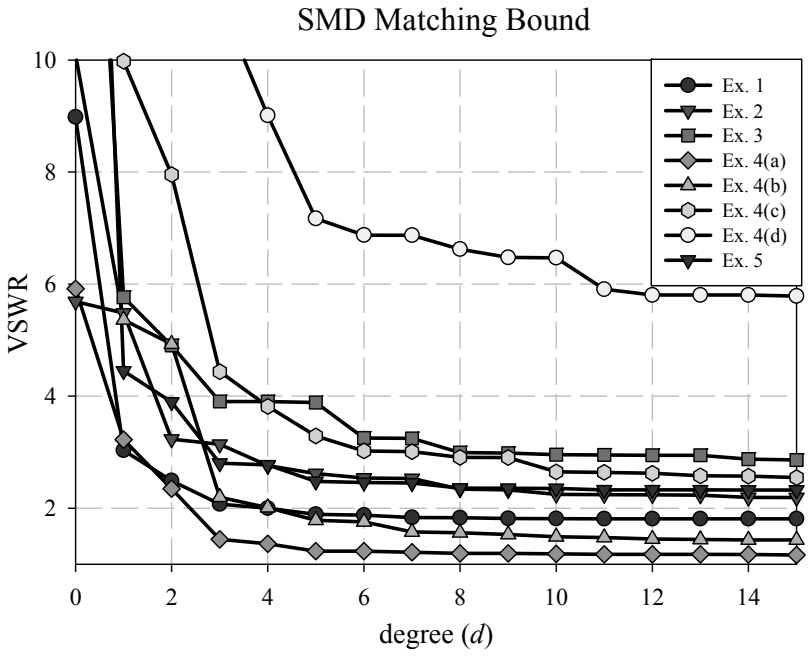

Figure 83. VSWR of the SMD method bound.